



UPPSALA
UNIVERSITET

*Digital Comprehensive Summaries of Uppsala Dissertations
from the Faculty of Science and Technology 715*

Fusion Plasma Observations at JET with the TOFOR Neutron Spectrometer

Instrumental Challenges and Physics Results

MARIA GATU JOHNSON



ACTA
UNIVERSITATIS
UPSALIENSIS
UPPSALA
2010

ISSN 1651-6214
ISBN 978-91-554-7724-0
urn:nbn:se:uu:diva-114077

Dissertation presented at Uppsala University to be publicly examined in Polhemsalen, Ångströmlaboratoriet, Uppsala, Friday, March 26, 2010 at 10:15 for the degree of Doctor of Philosophy. The examination will be conducted in English.

Abstract

Gatu Johnson, M. 2010. Fusion Plasma Observations at JET with the TOFOR Neutron Spectrometer. Instrumental Challenges and Physics Results. Acta Universitatis Upsaliensis. *Digital Comprehensive Summaries of Uppsala Dissertations from the Faculty of Science and Technology* 715. 110 pp. Uppsala. ISBN 978-91-554-7724-0.

The neutron spectrometer TOFOR was installed at JET in 2005 for high-rate observation of neutrons from reactions between two deuterium (D) ions. Neutron spectrometry as a fusion plasma diagnostic technique is invoked to obtain information about the velocity states of fusion fuel ions. Based on neutron spectrometry data, conclusions can be drawn on the efficiency of plasma heating schemes as well as optimization of fuel ion confinement. The quality of TOFOR analysis is found to depend on how well the instrument response function is known; discriminator threshold levels, detector time alignment and electronics broadening are identified as crucial issues.

About 19 percent of the neutrons observed with TOFOR have scattered off the JET vessel wall or other structures in the line-of-sight before reaching the instrument, as established through simulations and measurements. A method has been developed to take these neutrons into account in the analysis. TOFOR measurements of fast deuterium distributions are seen to agree with distributions deduced from NPA data, obtained based on an entirely different principle. This serves as validation of the modeling and analysis.

Extraordinary statistics in the TOFOR measurements from JET pulses heated with 3rd harmonic RF heating on D beams allow for study of instabilities using neutron emission spectrometry. At ITER, similar studies should be possible on a more regular basis due to higher neutron rates.

Observations of neutrons from Be+³He reactions in the TOFOR spectrum from D plasmas heated with fundamental RF tuned to minority ³He raise the question of beryllium neutrons at JET after installation of the ITER-like wall, and at ITER, with beryllium as the plasma facing component. This is especially important for the first few years of ITER operation, where the machine will not yet have been certified as a nuclear facility and should be run in zero-activation mode.

Keywords: Fusion, Plasma diagnostics, Neutron Spectrometry, TOFOR, JET, ITER, time-of-flight, plasma heating

Maria Gatu Johnson, Department of Physics and Astronomy, Applied Nuclear Physics,

© Maria Gatu Johnson 2010

ISSN 1651-6214

ISBN 978-91-554-7724-0

urn:nbn:se:uu:diva-114077 (<http://urn.kb.se/resolve?urn=urn:nbn:se:uu:diva-114077>)

To Darrin
You make life fun

List of Papers

This thesis is based on the following papers, which are referred to in the text by their Roman numerals.

I The TOFOR neutron spectrometer and its first use at JET

M. Gatu Johnson, L. Giacomelli, A. Hjalmarsson, M. Weiszflog, E. Andersson Sundén, S. Conroy, G. Ericsson, C. Hellesen, J. Källne, E. Ronchi, H. Sjöstrand, G. Gorini, M. Tardocchi, A. Murari, S. Popovichev, J. Sousa, R. C. Pereira, A. Combo, N. Cruz and JET EFDA Contributors

Reprinted with permission from M. Gatu Johnson et al., Review of Scientific Instruments, Vol. 77, Issue 10, Page 10E702, 2006. Copyright 2006, American Institute of Physics.

This paper reports on the installation of TOFOR at JET and on the first data recorded.

My contribution: Participated in the construction and installation of TOFOR, wrote the paper and presented the material at the conference.

II The 2.5-MeV neutron time-of-flight spectrometer TOFOR for experiments at JET

M. Gatu Johnson, L. Giacomelli, A. Hjalmarsson, J. Källne, M. Weiszflog, E. Andersson Sundén, S. Conroy, G. Ericsson, C. Hellesen, E. Ronchi, H. Sjöstrand, G. Gorini, M. Tardocchi, A. Combo, N. Cruz, J. Sousa, S. Popovichev and JET-EFDA contributors

Nuclear Instruments and Methods in Physics Research A **591** (2008) 417–430

A thorough description of the TOFOR setup is given, including discussions on the mechanics, electronics, control and monitoring system, response function and JET viewing geometry. The performance of the system relative to the design targets is reviewed. In addition, the instrument capabilities are highlighted

with examples of analysis of data from NB and RF heated plasmas.

My contribution: Participated in the construction and installation of TOFOR as well as in characterization of components and of the assembly as a whole, and wrote the paper.

III Modeling and TOFOR measurements of scattered neutrons at JET

M. Gatu Johnson, S. Conroy, E. Andersson Sundén, G. Ericsson, C. Hellesen, A. Murari, S. Popovichev, E. Ronchi, H. Sjöstrand, M. Weiszflog and JET-EFDA Contributors

In manuscript, to be submitted to Plasma Physics and Controlled Fusion

Neutrons that have scattered off the tokamak vessel wall or other structures in the line-of-sight before reaching TOFOR are shown in this paper to contribute about 19 percent of the neutrons observed with the instrument. The article describes how we model these neutrons using MCNPX to be able to take them into account in the analysis. Simulation and measurement results are found to agree, lending credit to the modeling.

My contribution: Responsible for the TOFOR experiments, performed the simulations and the analysis, wrote the paper.

IV Cross-validation of JET fast deuterium results from TOFOR and NPA

M. Gatu Johnson, C. Hellesen, M. Cecconello, E. Andersson Sundén, S. Conroy, G. Ericsson, G. Gorini, M. Nocente, E. Ronchi, H. Sjöstrand, M. Tardocchi, M. Weiszflog and JET-EFDA contributors

36th EPS Conference on Plasma Phys. Sofia, June 29-July 3, 2009 ECA Vol.33E, P-2.151 (2009)

Fast deuterium energy distribution results from TOFOR and the high energy Neutral Particle Analyzer installed at JET are compared in this paper and seen to qualitatively agree.

My contribution: Analyzed the TOFOR data, performed the comparison, participated in interpretation of the results, wrote the paper and presented the material at the conference. Received PPCF prize for best student poster.

V Neutron emission generated by fast deuterons accelerated with ion cyclotron heating at JET

C. Hellesen, M. Gatu Johnson, E. Anderson Sundén, S. Conroy, G. Ericsson, E. Ronchi, H. Sjöstrand, M. Weiszflog, G. Gorini, M. Tardocchi, T. Johnson, V.G. Kiptily, S. D. Pinches, S. E. Sharapov and JET-EFDA contributors

Nuclear Fusion **50** (2010) 022001 (5pp)

Recent experiments at JET involve 3rd harmonic RF heating on D beam seed. The scheme effectively accelerates deuterons to energies where the DD cross section is high. In this paper, we exploit the resulting high neutron rates for time resolved studies of the fast D distribution. TOFOR data are invoked to analyze the impact on the deuterium population of MHD effects.

My contribution: Active participation in the experiment and the data analysis, and in collaborations to interpret the results.

VI Neutron emission from beryllium reactions in JET deuterium plasmas with ³He minority

M Gatu Johnson, C Hellesen, E Andersson Sundén, M Cecconello, S Conroy, G Ericsson, G Gorini, V Kiptily, M Nocente, S Pinches, E Ronchi, S Sharapov, H Sjöstrand, M Tardocchi, M Weiszflog and JET EFDA contributors

Submitted to Nuclear Fusion, under review

In this article, a contribution to the neutron spectrum observed with TOFOR from reactions between RF heated ³He and beryllium is established. Beryllium neutrons are seen to contribute 13-57 percent of the observed neutrons in the 15 pulses studied.

My contribution: Participated in the experiment and in interpretation of the results, analyzed the data and wrote the paper.

VII Neutron emission levels during the ITER zero-activation phase

M. Gatu Johnson, C. Hellesen, E. Andersson Sundén, M. Cecconello, S. Conroy, G. Ericsson, G. Gorini, M. Nocente, E. Ronchi, M. Tardocchi, M. Weiszflog and JET EFDA contributors

Submitted to the special edition of Nuclear Fusion to be published in connection with the 11th IAEA Technical Meeting on Energetic Particles in Magnetic Confinement Systems, Kiev, Ukraine, Sept 21st-23rd 2009, under review

Reactions between fast H, ^3He or ^4He and beryllium could lead to neutron emission during the non-activated phase of ITER. In this paper, we investigate the possible magnitude of such neutron emission based on simulations of heating scenarios envisaged for this phase of ITER operations. It is concluded that higher harmonic RF heating on ^3He or ^4He could lead to substantial neutron production.

My contribution: Performed the simulations, wrote the paper and presented the material at the conference.

Reprints were made with permission from the respective publishers.

Contents

1	Introduction	13
1.1	Fusion as an energy source	13
1.2	Fusion reactions	15
1.3	Plasma heating	18
1.3.1	Neutral beam heating	19
1.3.2	Intrinsic heating	20
1.3.3	Radio frequency heating	21
1.4	MHD effects.....	24
2	Plasma diagnostics.....	26
2.1	Neutron diagnostics.....	26
2.2	Fast ion diagnostics.....	28
2.2.1	Gamma-ray diagnostics	29
2.2.2	Neutral Particle Analyzers	30
3	Neutron spectrometry	32
3.1	Background	32
3.2	Neutron spectrum simulations using ControlRoom.....	35
3.3	Scattered and direct neutrons	38
3.4	Analysis methods	40
3.4.1	Component fitting	41
3.4.2	Deuterium distribution unfolding	42
4	TOFOR	44
4.1	Line of sight	48
4.2	TOFOR response.....	50
4.2.1	Response function.....	51
4.2.2	Instrument characteristics	53
4.3	Optimization of data analysis.....	69
4.4	14 MeV TOFOR and hybrid boards.....	71
4.5	Improving campaign preparation and monitoring.....	74
5	Data analysis and results.....	75
5.1	Component analysis and scattered neutrons	76
5.2	Deuterium tails.....	79
5.3	Deuterium distribution unfolding.....	86
5.4	Beryllium neutrons.....	89

5.5	Results from 14 MeV neutron measurements	94
6	Outlook	98
6.1	Instrument improvements	98
6.2	Future experiments and data analysis	100
6.3	Outlook to ITER.....	101
7	Sammanfattning på svenska	102

Abbreviations

JET	Joint European Torus
H	Protons
D	Deuterons
T	Tritons
TBN	Triton Burn-Up
NB(I)	Neutral Beam (Injection)
RF	Radio Frequency
ICRH	Ion Cyclotron Resonance Heating
ECRH	Electron Cyclotron Resonance Heating
LHCD	Lower Hybrid Current Drive
PINI	Positive Ion Neutral Injector
FLR	Finite Larmor Radius
MHD	Magneto Hydro Dynamic
(T)AE	(Toroidal) Alfvén Eigenmode
NES	Neutron Emission Spectroscopy
HRNS	High Resolution Neutron Spectrometer
TPR	Thin-foil Proton Recoil
MPR(u)	Magnetic Proton Recoil (upgrade)
TOF(OR)	Time Of Flight (Optimized for Rate)
NPA	Neutral Particle Analyzer
CTS	Collective Thomson Scattering
PM(T)	Photo Multiplier (Tube)
CFD	Constant Fraction Discriminator
ADC	Analogue-to-Digital Converter
LED	Light Emitting Diode
DNL	Differential Non-Linearity
INL	Integral Non-Linearity
C&M	Control & Monitoring
TDC	Time-to-Digital Converter
FIFO	Fan-In-Fan-Out
FWHM	Full Width at Half Maximum
NTM	Neo-classical Tearing Mode
ILW	ITER-Like Wall

1 Introduction

The physics is simple; the application
requires sophistication.

Jeff Linsky, Magnetics course, 2008-02-13

This thesis concerns diagnostic observations of the JET fusion plasma using the time-of-flight neutron spectrometer TOFOR. My intention is that the reader, after making her way through the introductory chapters of this thesis, will understand what this means, and how our work with TOFOR fits in as one of the small pieces of the puzzle that will hopefully bring fusion to the world as an energy source within the next 50 years.

1.1 Fusion as an energy source

Simply speaking, fusion is the process in which two light nuclei fuse to release energy. The energy released is carried away in the form of kinetic energy of the product particles. This energy can be harnessed by converting it to heat which can be used to boil water in a steam cycle, similar to a conventional nuclear power plant. Fusion reactions power the sun and the stars. The idea of using them for power production also on earth is more than 50 years old. It has, however, turned out to be less than easy to create an environment where fusion processes can be sustained on a time interval compatible with commercial power generation. Currently, two main paths towards fusion on earth are being explored: inertial confinement fusion, where a small pellet of fusion fuel is heated with high-intensity lasers and made to implode, and magnetic confinement fusion. It is magnetic confinement fusion with which we are concerned here.

In order to make fusion reactions happen, the fusion fuel has to be extremely hot (~ 100 MK, see section 1.3). At these temperatures, matter is in the plasma state; atoms are split in ions and electrons, which due to their electric charge can be kept in place in a magnetic field where they move according to

$$m \frac{d\vec{v}}{dt} = Ze(\vec{E} + \vec{v} \times \vec{B}) \quad (1)$$

where m is the particle mass, v the velocity, Z the charge, E the electric and B the magnetic field [1]. The particles will gyrate along the magnetic field

lines with a characteristic radius (Larmor radius) r_L (unit m) and cyclotron frequency ω_c (unit rad/s):

$$r_L = \frac{mv_{\perp}}{ZeB} \quad (2)$$

$$\omega_c = \frac{ZeB}{m} \quad (3)$$

Fusion reactions are taking place in magnetic confinement research systems all over the world, though none with net energy production. In the EU, some 20 machines are currently being operated, e.g. Tore Supra in France and TEXTOR in Germany. The flagship device of the EU is the Joint European Torus, JET, where this work was carried out. JET is an example of a tokamak device (Figure 1).

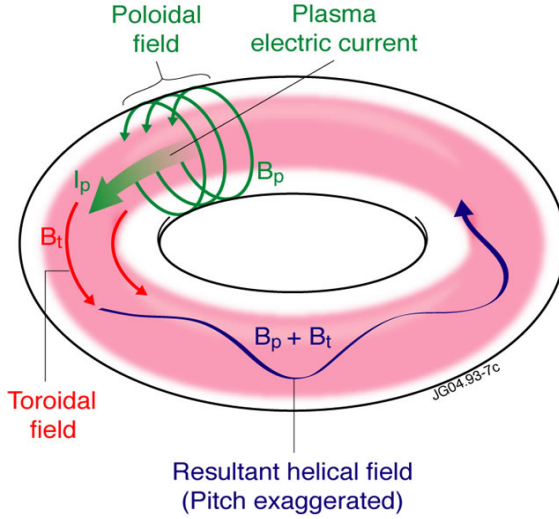


Figure 1. Schematic of a tokamak magnetic confinement fusion device, with poloidal, toroidal and resultant helical magnetic fields indicated. Figure: JET-EFDA. Courtesy of JET-EFDA. (Color online)

The tokamak is in the shape of a torus, with poloidal (from the current induced through the plasma) and toroidal (from fixed field coils) magnetic field components resulting in helical magnetic field lines around the device. The tokamak is so far the most successful magnetic confinement system, and the road map towards commercial magnetic confinement fusion includes a new tokamak device, ITER, currently under construction in southern France. ITER is a collaboration between the EU, Russia, South Korea, China, Japan,

India and the US. The plan is that with ITER, the viability of fusion as an energy source will be proven – but also ITER will not be used for energy production. This step will be taken in a later device, DEMO, where the concept of a fusion power plant will be demonstrated.

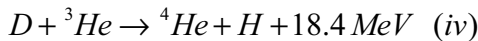
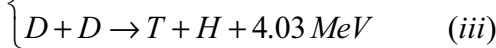
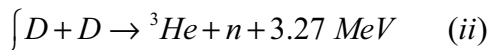
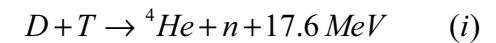
The JET tokamak has a major radius of about 3 m and a plasma volume of 90 m³. It is divided in eight equal sections, or octants, with octant numbers used to define the position of any auxiliary diagnostic or heating systems surrounding the machine. A divertor at the tokamak bottom removes heat and exhaust from the plasma in a controlled way. ITER, with a similar basic structure, will have a major radius of 6.2 m and a plasma volume of about 830 m³ [2].

As a means of measuring the progress in the fusion field, the Q value of a fusion experiment has been introduced, defined as the power released in the fusion reactions (P_{out}) divided by the power fed to the plasma through the auxiliary heating systems (P_{in}). The current world record of $Q=0.67$ was reached at JET in 1997; ITER is foreseen to reach $Q=10$.

1.2 Fusion reactions

In order for a fusion reaction to work in a power plant, a couple of conditions have to be fulfilled: The energy release must be positive (exothermic reaction) and preferably large, and the cross section for the reaction must be high for the relevant reactant energies. In the stars, it is mainly protons (H) that undergo fusion. However, the cross section for such proton reactions is too low under conditions achievable on earth. In Table 1, a number of reactions of relevance for fusion reactors are listed.

Table 1. Fusion reactions of reactor relevance.



The most promising reaction is (i), between two other isotopes of hydrogen, deuterium (D) and tritium (T). This reaction has a high energy release combined with high cross section. Another property of the D+T reactions is that both a charged particle and a neutron are produced. Power plant concepts based on the reaction exploit this property. The charged ⁴He ion is envisioned to stay confined in the reactor, transferring its kinetic energy back to the plasma thus keeping it hot, while the neutron, being neutral, will escape

the magnetic field and transfer its energy to the outside of the vessel where it can be harnessed.

The first commercial fusion power plants are foreseen to run with DT fuel. However, tritium suffers from the drawback of being radioactive and not readily available on earth; in the fusion power plants, it is planned to be bred from lithium in the reactor walls. In today's research reactors, pure deuterium fuel is more commonly used. There are two branches of the D+D reaction with approximately equal branching ratio, (ii) and (iii). Reaction (ii) is similar to the D+T reaction and D+D results can be used to infer properties of D+T fusion. Also, T is produced in (iii), which means there will always be some D+T reactions taking place even in a pure D plasma. The neutrons from such deuterium plasma D+T reactions are referred to as triton burn-up neutrons (TBN). JET operates routinely with D and is the only magnetic confinement fusion reactor in the world currently capable of running with DT fuel.

Neutrons are produced in both D+T and D+D (branch ii) fusion reactions. The flux of high energy neutrons from a fusion reactor leads to some induced radioactivity in the surrounding structures. There are scenarios where it can be beneficial to create a fusion plasma with a fuel that does not produce neutrons. ITER is planned to start operation with such so-called non-activating plasmas [2,3,4], to check the operational limits and safety systems before certification as a nuclear facility. Non-activating plasma fuel consists of protons or helium ions. After certification, ITER will move on to D fuel and finally to DT operation.

In addition to D and T, small amounts of H, ^3He or ^4He are commonly added to the JET plasma to change the scenario or plasma heating properties. JET has also been run with mainly H or ^4He fuel. Since intrinsic heating from ^4He particles from reaction (i) will eventually provide the main means of heating the plasma, the behavior of ^4He in the plasma is an important subject of study. Fusion reactions between D and ^3He create fast ^4He and H (iv), which facilitates this type of study.

The mentioned H, D, T, ^3He and ^4He can all be used as fuel ions. Also impurities will always be present in a tokamak plasma. Impurities are commonly vessel wall constituents that enter the plasma after being knocked out from the wall. The dominating plasma impurity at JET today is carbon (C), since JET is operating with a C wall and divertor. A beryllium (Be) wall and tungsten (W) divertor are under installation at JET and the plasma-facing material at ITER will be mainly Be. This means Be can be expected to take over as the main plasma impurity in the future. In paper VI, we find that on JET, Be can react with fuel ions to produce neutrons on a level observable with TOFOR. This could have implications for the non-activated phase of ITER. We explore the level at which neutrons will be created during the ITER non-activated phase in paper VII.

The rate R of fusion reactions of a certain type that takes place in a plasma is given by the product of the densities of the reactants and the reactivity of the reaction according to

$$R_{ij} = \frac{1}{1 + \delta_{i,j}} n_i n_j \langle \sigma v \rangle_{ij} \quad (4)$$

where δ_{ij} is the Kronecker delta, $i=j \rightarrow \delta_{ij}=1$, $i \neq j \rightarrow \delta_{ij}=0$. The reactivity $\langle \sigma v \rangle$ is the product of the energy dependent cross section and the relative velocity of the reactants, integrated over the reactant velocity distributions. In Figure 2, the reactivities for $D+T \rightarrow \alpha+n$, $D+D \rightarrow {}^3\text{He}+n/H+T$, $D+{}^3\text{He} \rightarrow \alpha+H$, $D+{}^9\text{Be} \rightarrow {}^{10}\text{B}^*+n$, ${}^3\text{He}+{}^9\text{Be} \rightarrow {}^{11}\text{C}^*+n$, $\alpha+{}^9\text{Be} \rightarrow {}^{12}\text{C}^*+n$ and $H+{}^9\text{Be} \rightarrow {}^9\text{B}+n$ reactions are shown, given reactants that are Maxwellian distributed with temperature $T=T_i$ (T_i is the ion temperature). As can be seen, the reactivity at lower temperatures is highest for the $D+T$ reaction at about a factor 100 above the $D+D$ reaction. At temperatures in the MeV range, also reactions between fuel ions and ${}^9\text{Be}$ need to be taken into account, as discussed in papers VI and VII.

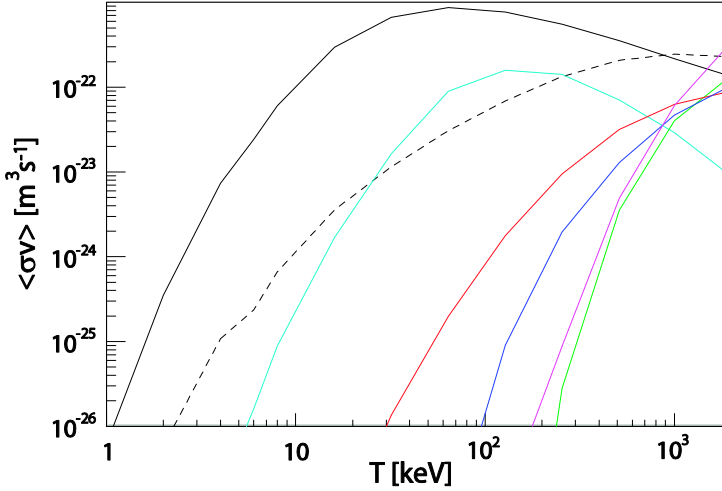


Figure 2. Maxwellian reactivities for the $d+t \rightarrow \alpha+n$ (black), $d+d \rightarrow {}^3\text{He}+n/p+t$ (dashed black), $d+{}^3\text{He} \rightarrow \alpha+p$ (cyan), $d+{}^9\text{Be} \rightarrow {}^{10}\text{B}^*+n$ (red), ${}^3\text{He}+{}^9\text{Be} \rightarrow {}^{11}\text{C}^*+n$ (blue), $\alpha+{}^9\text{Be} \rightarrow {}^{12}\text{C}^*+n$ (magenta) and $p+{}^9\text{Be} \rightarrow {}^9\text{B}+n$ (green) reactions.

1.3 Plasma heating

From Figure 2 it is obvious why the fuel needs to be hot in order for the reactions to take place; the reaction probability is simply too low to be feasible for cold reactants. 10 keV (~ 100 MK) is considered the limit where it starts to become possible to produce more energy than is needed to make the fuel ions react. The current induced through the tokamak plasma to create the poloidal component of the magnetic field also provides basic plasma heating through induction. This is commonly referred to as ohmic heating. However, the plasma resistivity decreases with increasing temperature, imposing a limit on the temperatures reachable through such heating. At JET, this limit is 2-3 keV [5].

To reach higher in temperature, auxiliary heating systems such as neutral beam injection heating (NB), ion and electron cyclotron resonance frequency heating (ICRH/ECRH) and lower hybrid cyclotron heating (LHCD) are used. At JET, NB, ICRH and LHCD systems are operated; at ITER, also ECRH will be of importance. Charged fusion products that stay confined in the magnetic field will also contribute to plasma heating as they transfer their kinetic energy through collisions with plasma electrons and ions (intrinsic heating). In a future burning plasma, this intrinsic heating will provide the bulk of the heating power needed to run the reactor.

In a plasma heated through ohmic heating only, the fuel ions are Maxwellian distributed (Figure 3).

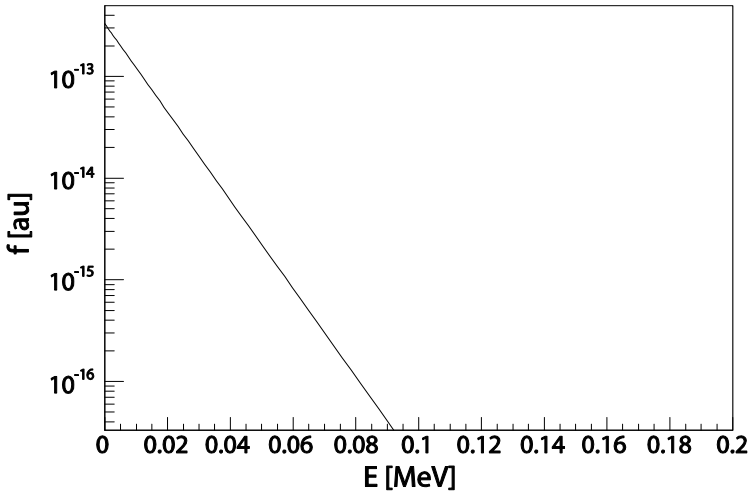


Figure 3. Maxwellian distribution as a function of particle energy for a 10 keV plasma.

The applied heating creates populations of fast ions in the plasma, changing the velocity distributions of the reactants and thus the reactivity as well as the energy carried by the reaction products.

For this thesis, we are mainly concerned with intrinsic heating and the NB and ICRH auxiliary heating systems.

1.3.1 Neutral beam heating

In neutral beam heating, ions are accelerated to high energies and subsequently neutralized in a charge-exchange target so that they can penetrate the magnetic field to enter into the plasma. In the plasma, they re-ionize and transfer their energy in a slowing down process through collisions. Electron collisions dominate above the critical energy and ion collisions below the critical energy. The distribution of neutral beam heated ions in a plasma will thus exhibit a typical shape with an edge at the injection energy and a slowing down tail towards lower energies, which can be approximately described as [6,7]

$$f(v) = \begin{cases} \frac{const}{v^3 + v_c^3} & ; v \leq v_{inj} \\ 0 & ; v > v_{inj} \end{cases} \quad (5)$$

where v_c is the critical velocity given by

$$v_c = \sqrt{2 \left(\frac{3\sqrt{\pi}}{4} \right)^{2/3} \left(\frac{m_{bulk}}{m_e} \right)^{1/3} \frac{m_B}{m_{bulk}} T_e / m_B} . \quad (6)$$

T_e is the electron temperature and m_e , m_B and m_{bulk} the masses of electrons and beam and bulk ions, respectively.

At JET, positive ions are accelerated to 80 or 130 keV before injection in the plasma; at ITER, the plan is to accelerate negative ions to 1 MeV. The JET NB system consists of two injector boxes (in octants 4 and 8) each with eight positive ion neutral injectors (PINIs). The PINIs have different alignment so that ions can be injected “normal” or “tangential” to the magnetic field and on or off axis. This characteristic of the JET NB system was seen to affect the results in paper IV.

In simulations aimed at approximating the neutron energy spectrum or expected neutron rates from NB heated pulses, we use a more complex solution to the Fokker-Planck equation than that given in equation (5) [7]. Figure 4 shows an example of such an NB distribution for 130 keV deuterium beams at JET, compared with the simplified distribution from equation (5).

The slopes of the two distributions follow each other rather closely. However, the complex solution has the additional features of a sink at low energies ($T_e=3$ keV in this example) below which the beam ions are assumed to have left the population, and a tail towards energies above the injection energy. This tail is the result of electron diffusion, i.e., the beam population is broadened in energy due to collisions with bulk electrons.

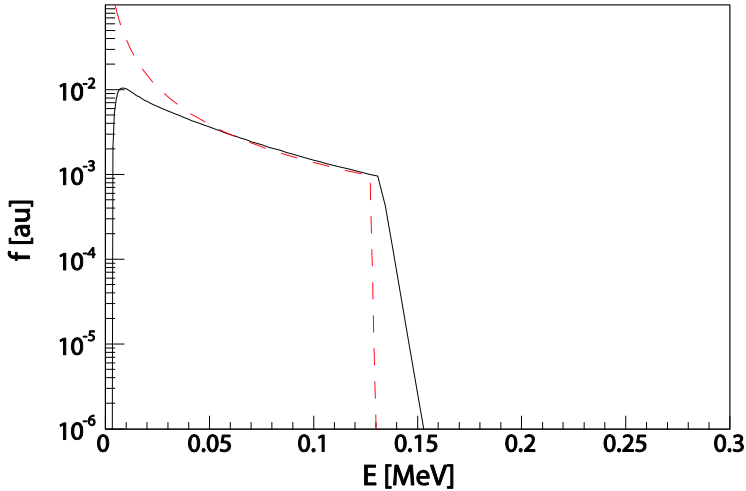


Figure 4. Analytical slowing down distribution for 130 keV deuterium ions injected into a 3 keV plasma with electron density $n_e=3.0\times 10^{19} \text{ m}^{-3}$ (solid black), and a simplified distribution calculated according to equation (5) (dashed red). (Color online)

In Figure 4, all ions are assumed to be injected with the same energy. In reality, the beam population at JET will contain a fraction of ions injected at 1/2 and 1/3 the nominal injection energy due to acceleration of gas molecules in the beam.

In fusion research, NB heated discharges are commonly modeled using the well-established TRANSP code [8].

1.3.2 Intrinsic heating

The distribution in the case of intrinsic (fusion product) heating will be similar to the neutral beam heating case, only with a different source term. The source here is the fusion reactions. Fusion products will be produced in an energy spectrum depending on the velocity state of the fuel ions. This source distribution will then follow the same slowing down process as the injected beam ions. As an example, the α source term from reactions between Maxwellian distributed D and T ions in a 10 keV plasma is shown along with the

resulting slowing down distribution in Figure 5. Another example can be found in paper VI, where α source terms and slowing down distributions from Maxwellian ^3He populations reacting with 5 keV bulk D populations according to reaction (iv) above are illustrated. Note that the different reactant distributions lead to very different source term shapes in the two cases.

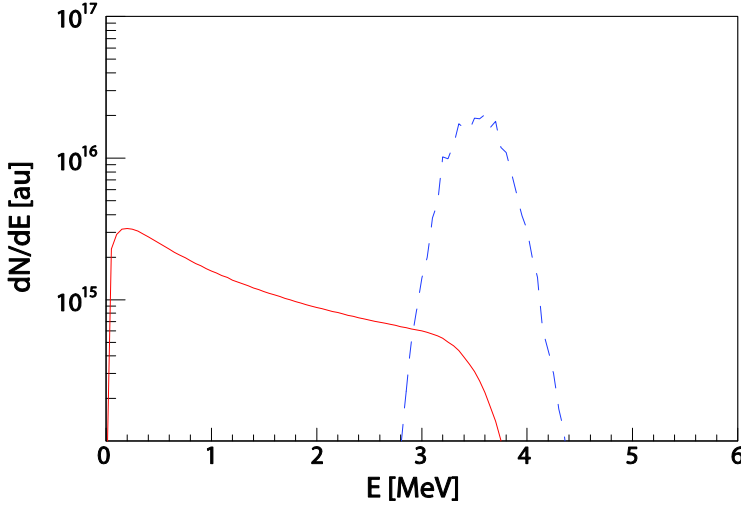


Figure 5. Alpha source term (dashed blue) and slowing down distribution (solid red) from reactions between Maxwellian distributed D and T in a 10 keV plasma with electron density $n_e = 1 \times 10^{20} \text{ m}^{-3}$. (Color online)

1.3.3 Radio frequency heating

During the work with this thesis, it has become clear that TOFOR can make important physics contributions in JET experiments heated with ICRH. Papers IV, V and VI all involve analysis of radio frequency (RF) heated JET discharges. Paper VII concerns simulations of neutron spectra from RF heated ITER discharges. RF heating is a diffusive process in which the ions are gradually accelerated to higher energies through energy transfer from wave to ion. The diffusive heating is balanced by fast ion slowing down as described above in the cases of NB and intrinsic heating; the slowing down time will characterize the formation of the high-energy tail [9].

The cyclotron frequency ω_c of the ions is proportional to their charge-to-mass ratio as described in equation (3). RF waves with frequency ω can couple to different harmonics of the ion cyclotron motion according to $\omega = n\omega_c$, where n is the harmonic number. The resonance frequencies for D and α will coincide at the same harmonic since the charge-to-mass (Z/m) ratio is the same for the two ions, while the fundamental resonance of H

coincides with the 2nd harmonic resonance of D, and fundamental ³He with 2nd harmonic T. The position of the RF resonance layer in the tokamak plasma, R_ω , will depend on the wave frequency and the magnetic field of the plasma. The magnetic field at R_ω can be approximated as $B \approx B_0 R_0 / R_\omega$, where B_0 is the field at the magnetic axis located at R_0 , giving

$$R_\omega \approx R_0 \frac{nZeB_0}{2\pi m\omega} \quad (7)$$

(for ω given in Hz).

Heating at the fundamental harmonic ($n=1$) is most efficient for a population of minority ions in the plasma [10] and is at JET frequently applied to H or to ³He added to the bulk deuterium population in small amounts (as discussed in e.g. [11], where a survey of (³He)D experiments at JET is given, or [12], discussing TOFOR measurements during (³He)D mode conversion experiments). Paper VI presents results from minority ³He experiments.

Higher ($n \neq 1$) harmonic heating couples preferentially to high energy ions [10]. For this reason, 2nd or 3rd harmonic RF heating is frequently applied to a seed population of NB injected ions (papers IV and V).

The efficiency of the wave-particle coupling depends on the plasma scenario and what species compete for the coupled power. In [13], the power partition between different species for varying ICRH wave frequencies for the ITER DT phase of operations is analyzed. It is found that the best heating efficiency would be achieved if the plasma is seeded with ³He and absorption at the fundamental ³He frequency dominates, with competing electron and 2nd harmonic T absorption.

In paper VII, Stix's steady state solution to the Fokker-Planck equation [6,7] is used to approximate the complex form of the RF heated ion velocity distributions. Figure 6 shows example distributions for fundamental (5% ³He in D plasma), 2nd and 3rd harmonic (1 MW, 93 keV ⁴He beams in ⁴He plasma) heating.

In Stix' formulation, the effect on the distribution of the finite Larmor radius (FLR) of the gyrating ions will be taken into account through the RF diffusion operator (D_{RF}). In [14], it is shown that there will be an electron density (n_e) and magnetic field (B) dependent cut-off in the distribution due to the shape of D_{RF} . This FLR effect and its dependence on n_e is reproduced in TOFOR data as shown in paper V. Not taken into account in Stix' formulation is e.g. power partition between different plasma species and mode conversion effects. Mode conversion means that the fast wave providing the resonant heating is converted to a different type of wave (see e.g. [15] and references therein). In [15], JET experiments in H plasmas show that at a minority concentration of about 2% ³He, mode conversion heating takes over from minority fundamental RF heating and no fast ³He tails are formed. This

will affect which of the distributions used to estimate the neutron rates from zero-activation ITER plasmas in paper VII are actually physically possible. Mode conversion can also have an effect in (^3He)D plasmas, as will be discussed in section 5.2.

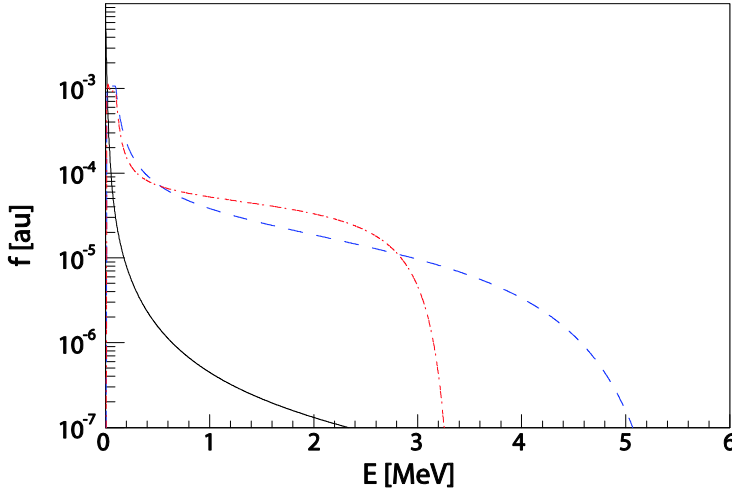


Figure 6. Stix distributions for fundamental RF heating of a 5% ^3He minority in a D plasma (solid black) and 2nd (dashed blue) and 3rd (dash-dot red) harmonic RF heating on 1 MW ^4He beams in a ^4He plasma (assuming $E_{\text{beam}}=93\text{ keV}$, $T_e=5\text{ keV}$, $n_e=5\times 10^{19}\text{ m}^{-3}$ and $B_T=2.3\text{ T}$). (Color online)

RF heated discharges are commonly modeled using tools such as PION [9] or SELFO [16].

1.3.3.1 3rd harmonic heating experiments

In paper V, TOFOR results from JET deuterium discharges heated with RF tuned to the 3rd harmonic D resonance with a D beam seed are presented. These discharges are unique. 3rd harmonic deuterium heating was previously tried at JET in the mid 90s, but then without NB seed (see e.g. ref 17). Also at Tore Supra the scheme was tried without beam seed. A scheme with D beam seed was applied at TEXTOR [18]. In Tore Supra, electron heating was seen to dominate. At JET, a population of fast ions heated through the 3rd harmonic scheme was slowly built up during the discharge. At TEXTOR, with the beam seed, the scheme was seen to dominantly and effectively heat the fast beam ions. These observations are in line with theory which predicts that the efficiency of the 3rd harmonic coupling is quadratically dependent on particle energy. The JET experiments studied in paper V were performed in the summer of 2008. By then, coupling of 3rd harmonic RF to ohmic plasmas was prohibited at JET due to the risk of competing resonances at the plasma

edge. A beam seed was used and the scheme was seen to be highly efficient in producing neutrons, giving excellent statistics in the TOFOR data. This can be understood by looking at the reactivity curves for the DD and DT reactions in Figure 2. With 3rd harmonic heating, D ions are accelerated to the MeV range, where the DD reactivity is comparable to the peak DT reactivity. In fact, the number of fusion reactions per unit auxiliary power applied is among the highest in JET's history.

3rd harmonic acceleration of ⁴He beams had been previously tried at JET [19,20]. The scheme was again applied during a low-activation campaign in the fall of 2009. A problem with this scheme is that the 3rd harmonic D and ⁴He resonances compete at the same position R_{ω} . Since JET routinely operates with D plasmas, it is hard to get a D-free ⁴He plasma. ⁴He and D absorption will compete even though no D beams are used. Some TOFOR results from these recent 3rd harmonic ⁴He experiments will be presented in section 5.4 of this thesis.

1.4 MHD effects

Magneto hydro dynamic (MHD) modes in the plasma are instabilities that result from small perturbations in the magnetic field. Sawteeth, Alfvén Eigenmodes (AE) and fishbones are examples of MHD modes that interact with fast ions in the plasma, causing redistribution or even loss of these fast ions. Interactions between fast ions and MHD modes at JET are discussed in [21]. It is important to understand how the instabilities affect plasma confinement, heating and fast ion dynamics, and to learn how to avoid instabilities. TOFOR can contribute to the studies on interaction between fast particles and MHD activity as demonstrated in paper V and section 5.3.

Sawteeth occur in the plasma when the value of the safety factor (q , number of toroidal over poloidal rotations around the torus) is less than 1 [5]. They are periodic relaxation oscillations in the center of the plasma, with each sawtooth crash changing the magnetic topology. The oscillations are visible in measured temperature and density profiles, and also in other diagnostics such as measured fast ion signals. The presence of fast ions can stabilize the sawtooth behavior increasing the period between sawtooth crashes and thus creating a so-called monster sawtooth. Monster sawteeth have been observed with TOFOR as described in paper V.

Alfvén Eigenmodes are related to Alfvén (hydromagnetic) waves in the plasma. Alfvén waves are low frequency oscillations ($\omega < \omega_c$) along the magnetic field, travelling along the magnetic field line with speed $v_A \sim B/(\mu_0 \rho)^{1/2}$ (Alfvén speed, μ_0 constant, ρ mass density) [1]. Toroidal Alfvén Eigenmodes (TAE) are shear Alfvén waves which resonantly interact with fast ions with speeds close to the Alfvén speed. Tornados are core-localized TAEs [22]. Fast ion speeds close to the Alfvén speed is a require-

ment for resonant AE interactions to take place. Since the Alfvén speed is proportional to the magnetic field B , high-field devices such as JET require high-energy ions for AEs to occur. This means at JET, ICRH ions are needed for interaction, while at smaller machines super-Alfvénic speeds can be reached with NB injected ions.

MHD modes in tokamaks are commonly diagnosed using arrays of external magnetic pick-up coils (Mirnov coils) registering fluctuations in the toroidal magnetic field [23]. From the collected data, frequency spectrograms are constructed that show oscillations of varying frequency of the magnetic field lines. Such spectrograms are compared with TOFOR data from 3rd harmonic ICRH discharges in paper V.

2 Plasma diagnostics

The first principle [of science] is that you must not fool yourself – and you are the easiest person to fool.

Richard Feynman

Diagnostics are an essential part of magnetic confinement fusion research. The purpose of diagnostic measurements is to understand, control and improve the fusion environment to make it possible to realize the goal of commercial energy production from fusion in the future. There are numerous diagnostic systems connected with each fusion research machine to determine the magnetic field and currents, the plasma shape, electron, fuel ion and impurity densities, temperatures, total impurity content, produced fusion power, plasma-wall interaction effects, modes in the plasma etc. Work is ongoing to determine what diagnostics are needed for ITER; in [24], some 45 diagnostic systems are identified as necessary for machine protection, plasma control and physics evaluation.

This thesis has been mainly concerned with neutron diagnostics. A subsection below is dedicated to discussing neutron diagnostics in some detail. Neutron spectrometry in particular has turned out to be useful as a tool for diagnosing confined fast ions. An introduction is given to the topic of fast ion diagnostics to put this work in perspective.

2.1 Neutron diagnostics

There are two main advantages to using neutrons to diagnose a fusion plasma. Firstly, they are created in the reactions between fuel ions, which means they will carry direct information about the fuel ions. Secondly, they are neutral, which means they will escape the magnetic confinement and can be used as an external probe of internal conditions. Neutron diagnostics are non-intrusive and require no direct contact with the harsh plasma environment. For this reason, they are foreseen as one of few diagnostic methods that will be relevant also for DEMO [25]. Neutrons are emitted both in D+T reactions (with nominal energy of 14 MeV) and D+D reactions (2.5 MeV).

Neutron diagnostics can be divided in three principal categories: flux monitors, emission profile monitors and neutron spectrometers (see e.g. ref 26). Flux monitors measure the neutron emission rate. Since the neutrons are

emitted in the fusion reactions, this rate will be directly related to the fusion power produced in the reactor. Monitoring of the neutron emission rate is required for regulatory purposes. Because the high-energy neutrons cause activation of the structures surrounding a tokamak, the number of neutrons produced is strictly controlled. At JET, the main neutron flux monitor diagnostic is the fission chambers (KN1, [27,28]), cross-calibrated using activation foils (KN2, [29,30]). There are also silicon diodes used for 14 MeV neutron flux measurements (KM7, [31]).

Neutron emission profile monitors (also called cameras) measure the spatially resolved neutron emission. The JET neutron profile monitor (KN3, [32]) has 10 horizontal lines of sight and 9 vertical, covering the plasma in the poloidal plane.

Neutron spectrometers aim at measuring the energy distribution of the emitted neutrons along their line-of-sight, so-called neutron emission spectrometry (NES). However, since neutrons are neutral, their energy cannot be measured directly. Techniques used are reviewed in e.g. [33,34]. Four main schemes can be identified that have been pursued to measure neutron energy spectra in fusion research: (i) neutron-induced nuclear reactions, with measurement of the energy of the charged reaction products, (ii) neutron scattering, with measurement of the energy of the charged recoil nucleus, (iii) measurement of the neutron velocity and (iv) threshold reactions (see e.g. [30]), where the neutron energy is inferred based on its ability to induce nuclear reactions with set energy thresholds.

Examples of systems operating based on scheme (i) are e.g. semiconductors and ^3He ionization chambers. In diamonds [35], the energy deposited by the reaction products from $^{12}\text{C}(n,\alpha)^9\text{Be}$ are measured. ^3He ionization chambers, measuring the energy of the $^3\text{He}(n,p)\text{T}$ products, have been extensively used (see e.g. [26, 36]), but their applicability is limited by their restricted count rate capability [33].

Various types of spectrometers make use of neutron scattering reactions according to scheme (ii). Commonly, n,p (or n,d) scattering with detection of the scattered proton (or deuteron) is used. Assuming $m_n=m_p$, the energy of a recoil proton will be related to the energy of the neutron according to

$$E_p = E_n \cos^2 \theta \quad (8)$$

where θ is the scattering angle. A conceptually simple way of implementing the n,p scattering technique is the use of a single scintillator placed in the neutron beam from the plasma, e.g., stilbene [37] or an NE213 liquid scintillator [38]. The implementation of such a system is straightforward, relatively cheap and requires little space. However, only the energy of the recoil particle is measured. Depending on the scattering angle, this energy can correspond to a number of different incident neutron energies, making the meas-

ured spectrum difficult to disentangle to be able to draw conclusions on the spectrum of incident neutron energies. More designed systems have been conceived where also the scattering angle is accounted for, e.g., thin-foil proton recoil systems. Such instruments will have a peaked response function that makes the disentangling easier. The recoil protons from scattering in the foil of a thin-foil proton recoil spectrometer of telescope type [39,40] go on to be detected in a $\Delta E/E$ detector (e.g., a silicon semiconductor) if emitted at a certain angle θ . In a magnetic type thin-foil proton recoil spectrometer such as the MPRu at JET [41], protons scattering in a narrow angular interval $\Delta\theta$ are momentum-separated in a system of bending magnets to determine their energy distribution. They can subsequently be detected using, e.g., plastic CR-39 [42], semiconductors or scintillator detectors.

TOFOR is an example of a time-of-flight system, where the neutron energy is inferred from its velocity according to scheme (iii). The neutrons are detected through n,p scattering in two detector sets placed at a set distance and angle from each other. The neutron energy can be deduced from the time-of-flight of the neutrons between the two detector sets. TOFOR is described in detail in paper II and section 4. Time-of-flight spectrometers have been used before, both at JET and JT60-U (see e.g. [26,43] and references therein).

A few parameters can be identified that determine the performance of a neutron spectrometer: efficiency, resolution, dynamic range (neutron flux range over which the instrument is able to operate without saturation), energy bite (energy range covered by the instrument), calibration stability and knowledge of the instrument response function. High efficiency is crucial since the ability to do advanced analysis is directly related to the statistics in the data. Often, a balance has to be struck between the competing requirements of efficiency, resolution and practical constraints, as discussed in the case of TOFOR in paper II. The relative merits of the systems mentioned here in terms of these parameters is discussed in e.g. [26,33].

Neutron spectrometry will be further discussed in a dedicated section below (section 3).

2.2 Fast ion diagnostics

Heating in all processes described above involves energy transfer to the bulk plasma in the slowing down of a population of fast ions, injected through neutral beam injection, fusion-born or created through coupling of radio frequency waves to the plasma. In order to achieve the goal of efficient fusion power production, it is crucial to confine these fast ions long enough for them to heat the plasma. This motivates a strong interest in fast ions and a whole field of diagnostics is dedicated to the study of confined and lost fast ions. It is important to understand the mechanisms that affect the confine-

ment of the fast ions; besides classical losses due to e.g. diffusion, finite orbit width and machine size, also interaction with MHD activity in the plasma has been seen to play a role.

Confined fast ion diagnostics in use at JET are besides NES also Neutral Particle Analyzers (NPAs) and γ measurements. These techniques can all be used to study fast ions in the MeV energy range. NES is the subject of this thesis and the NPA and γ diagnostics will also be discussed in some detail below. Collective Thomson Scattering (CTS, see e.g. [44] and references therein) and Fast Ion D(Alpha) (FIDA, [45,46]) are other examples of confined fast ion diagnostic techniques. In CTS, fast ions are diagnosed through studying their impact on the surrounding electron population. The collective motion of the electrons in the wake of a fast ion is deduced through studying the scattering of microwaves injected into the plasma using a gyrotron. CTS can also be used to study fast ions in the MeV energy range. The FIDA technique involves measurement of the Doppler-shifted wings of the light emitted in neutralization of fast ions around a neutral beam injected into the plasma. It is most useful in the tens of keV energy range due to the energy-dependence of the charge exchange cross section.

Examples of lost fast ion diagnostics are scintillator probes and Faraday cups. JET has a scintillator probe and an array of 5 Faraday cups installed to study fast ion losses [47].

2.2.1 Gamma-ray diagnostics

Gamma-ray diagnostic measurements involve the detection of γ released in reactions between fuel ions and plasma impurities such as ^{12}C or ^9Be [48]. The technique is well suited for measurements of fast ions in the MeV energy range because the cross-sections for the γ releasing reactions involved are high in this energy region. For diagnosis of fast D at JET, the reaction $^{12}\text{C}(\text{d,p})^{13}\text{C}^*$ is useful. ^{12}C is the most common impurity at JET because carbon is the material used in the plasma-facing components. ^3He and ^4He are more easily diagnosed through their interactions with ^9Be . This impurity is not abundant at JET and Be seeding is often undertaken before fast ion experiments to improve the experimental conditions for the γ diagnostics. The experiment studied in paper VI involved Be seeding, and results from measurements of γ from $^9\text{Be}(^3\text{He,n})^{11}\text{C}^*$ are also used in this paper to verify the presence of fast ^3He ions in the plasma. In paper VI, we conclude that also the neutrons from the $^9\text{Be}(^3\text{He,n})^{11}\text{C}^*$ reaction can be observed. This opens up for the possibility of comparing TOFOR and γ results from future experiments with better statistics involving this reaction or $^9\text{Be}(^4\text{He,n})^{12}\text{C}^*$.

The gamma-ray diagnostics can be divided in two categories: tomographic measurements [20] and spectroscopy [48]. At JET, the neutron camera system can also be used as a γ camera for tomographic measurements of the γ emission. So far, this has been most successfully done if special CsI crys-

tals with higher γ detection efficiency are placed in front of the normal neutron detectors in each channel, but the neutron detectors themselves (NE213) are set up to be usable also for γ detection.

JET has two sight lines for γ emission spectroscopy: one tangential, with a BGO spectrometer, placed in the torus hall, and one vertical. The vertical γ spectrometer is placed in the roof laboratory at JET, in the TOFOR line of sight, about 3 m further away from the torus. Currently there are three different systems for use in this line of sight, placed on an automated slider for easy switching between the systems. These are an old NaI(Tl) system with good efficiency but relatively poor energy resolution, a new LaBr system with intermediate energy resolution and efficiency and a high-purity Ge detector (HPGe) with excellent energy resolution but relatively poor efficiency.

2.2.2 Neutral Particle Analyzers

Neutral Particle Analyzers (NPA) work on the principle of detecting neutralized plasma ions that escape the magnetic confinement [23]. From the energy distribution of the detected escaping atoms, the energy distribution of the fuel ions in the plasma can be derived. The interpretation of the measured distribution of the neutral atoms requires different atomic processes to be taken into account, such as electron and ion impact ionization (loss term), electron radiative recombination (source term), and charge exchange with both main fuel ions and impurities (both a loss and a source term of neutrals) [23]. To correctly model these processes a good knowledge of the temperature and density profiles of all the species involved is necessary. The density profiles of the neutral particles are particularly difficult to measure and instead estimates based on Monte Carlo transport simulations or fluid models are used. Additional complications arise in the presence of NBI heating as it provides an additional source of "warm" neutrals along the beam path and an increased presence of impurities in the plasma with which the neutrals can interact.

JET has two NPAs, a low energy NPA (KR2 [49]) with a radial view of the plasma, and a high energy NPA (KF1 [50]) with a vertical view of the plasma at $R = 3.14$ m, both in octant 4 with a view of the beams injected through the octant 4 beam box. Each system can be set to detect H, D or ^3He neutrals. Paper IV presents a cross-validation study of deuterium distributions derived from TOFOR and KF1 data at JET. The two instruments are based on different physical principles and modeling has been derived independently in the two cases. The model used for KF1 at JET is described in [51]. In paper IV, we confirm a qualitative agreement between the results. The paper was written as the result of a pre-study for a dedicated experiment proposed, planned and accepted to be run at JET to further cross-validate the measurements from the two instruments. Unfortunately, the experiment had to be cancelled at the last minute due to problems with the liquefier used to

produce liquid ^4He for regeneration of the cryopumps, and could not be rescheduled before the current (2009-2010) shutdown.

3 Neutron spectrometry

*Life will become harder for theorists because
the diagnostics are getting better.*

Philip Lauber, theoretical summary, IAEA
TM on Energetic Particles, Sept 2009

As described above, neutron spectrometers aim at deducing the energy spectrum of neutrons emitted from the plasma. Since the neutrons are born in reactions between fuel ions, the velocity states of the fuel ions will affect their kinetic energy. Hence, the neutron energy distribution contains information about reactant distributions and fuel ion velocity distributions can be obtained from neutron spectral data. In this chapter, the physics of how ion distributions manifest themselves in the neutron spectra is reviewed. Practical examples of how model neutron spectra are derived using the Monte Carlo code Control-Room are presented, and the impact on the measurements of scattered neutrons is discussed. Finally, methods used to deduce the neutron energy spectra and fuel ion distributions from the measured data are described. In the first section, a brief sketch of the development of neutron spectrometry is given; it is in no way to be viewed as the complete history of this diagnostic field.

3.1 Background

Neutron spectrometry was first proposed as a tool for diagnosing ion velocity distributions in fusion plasmas by Lehner and Pohl in 1967 [52]. In their paper, Lehner and Pohl examine the non-relativistic kinematics of how neutron energies relate to ion energies and derive the neutron spectrum for some example distributions. They find e.g. that the width of the (Gaussian) peak in the neutron spectrum, ΔE_n , from reactions between Maxwellian distributed ions is related to the Maxwellian temperature according to

$$\Delta E_n \approx 82.5 \sqrt{kT} \quad (9)$$

for DD reactions (ΔE_n ¹ and kT in keV), and also that the peak will be displaced towards higher energies as the plasma temperature increases. Lehner and Pohl conclude that it would be useful to use neutron spectrometry to derive information on the fuel ions, and that this is also already being tried.

¹ ΔE_n is the full width at half maximum (FWHM) of the peak

Lehner and Pohl's derivation is updated and revised by Brysk [53] in 1975. Brysk concludes that the peak broadening due to temperature should be resolvable in the neutron spectrometers available at the time but that the peak displacement will be more difficult to detect. The measurements could, he claims, be used to determine the plasma temperature if the plasmas are roughly Maxwellian, or to "identify non-thermal conditions" if they are not.

Measurements of the spectrum of neutrons from DD reactions at the Alcator C tokamak in the early 1980s are reported in [36]. The authors are able to show that the neutron spectrum from high- T_i discharges is different from that from low- T_i discharges. They use the Cash method [54]² to fit a Gaussian to their measured neutron peaks. Reference is made to 1977 measurements at the Princeton Large Torus where the signal spectrum was obscured by background neutrons. The authors show an improvement in the results compared to these old measurements due to the higher plasma density at Alcator C. Still, also in the newer measurements, 169 low- T_i and 38 high- T_i pulses have to be summed to perform the analysis. Here, one of the main limitations of neutron spectrometry becomes apparent; the results can never be better than the neutron rates available because this puts a definite limit on the statistics achievable in the measurement.

JET started operation in 1983. Around this time, also other larger machines were appearing at which significantly higher rates of neutrons were produced. Higher precision neutron spectrometry measurements now started to be possible. In a paper on neutron spectrometry results from JET from 1993 [55], the focus has shifted from determining the average temperature of 169 pulses to describing the spectrum from one pulse (measured by a time-of-flight spectrometer) in terms of thermonuclear, beam-thermal and beam-beam contributions. It was also around that time (1992) that the idea of a time-of-flight spectrometer optimized for high count rate, that was to mature into the TOFOR project, was first presented [56].

In a review paper from 1994 by Jarvis [26], neutron spectrometry developments up to this time are summarized. Jarvis gives an overview of techniques tried and shows some examples of recent results from JET. He makes a couple of important points: (i) The energy resolution of the spectrometer should be "rather less" than the thermal broadening of the spectral peak for plasmas from a few keV and upwards. This does not mean that thermal broadening below the resolution of the instrument cannot be measured; however, higher counting statistics and good knowledge of the spectrometer resolution will be required. The TOFOR resolution is discussed in paper II. (ii) The temperature measured with a neutron spectrometer will depend on the instrument line of sight and cannot be simply assumed to be representative of central plasma temperatures though the correction factor might be small. Line-of-sight effects on temperature measurements in thermonuclear

² This method is used also in TOFOR analysis as will be further described below.

plasmas are discussed in detail in [57]. (iii) Measurements of 2.5-MeV neutrons from DD reactions are complicated due to the interference in the spectrum of energetic neutrons from ICRF heated fast ions and plasma impurities. In our work with TOFOR, we have seen that this can be viewed not as a problem but as an advantage, since this means neutron spectrometry can be used to answer questions also about these fast ions and impurities, as exemplified in paper VI.

The MPR spectrometer, installed at JET in 1996, demonstrated the usefulness of neutron spectrometry to study DT plasmas during the 1997 JET DT campaign. With the MPR, contributions to the spectrum from NB or ICRF heated ions reacting with the bulk population (see e.g. refs 58 and 59) as well as synergy effect from the two systems [60] could be isolated. A contribution to the spectrum from reactions involving a population heated through ^4He knock-on could also be established [61].

Neutron emission spectrometry has now turned into a high-precision measurement technique. In a paper by Luigi Ballabio [62], earlier analytical neutron spectrum results are compared with relativistic analytical and Monte Carlo calculations. The conclusion is that the relativistic approach is needed to reproduce the measured thermal peaks from especially DT reactions in warm plasmas to the required accuracy (example: relativistic DT $E_n=14.021$, non-relativistic $E_n=14.041$ MeV). Ballabio also gives interpolation formulas for the mean energy and width of the thermal neutron peaks in the range $0 < T_i < 100$ keV (previous interpolations were only available up to 20 keV).

In Ballabio's non-relativistic formulation [62], the energy of a neutron (or other particle) emitted in a two-body fusion reaction can be written

$$E_3 = \frac{1}{2} m_3 v_{CM}^2 + \frac{m_4}{m_3 + m_4} (Q + K) + v_{CM} \cos \theta \left[\frac{2m_3 m_4}{m_3 + m_4} (Q + K) \right]^{\frac{1}{2}}$$

$$K = \frac{1}{2} \mu v_{rel}^2$$
(10)

where subscripts 3 and 4 identify the two reaction products, m the masses, Q the nominal energy release in the reaction (not to be confused with $Q=P_{out}/P_{in}$ as introduced in section 1.1), μ the reduced mass, v_{CM} and v_{rel} center-of-mass and relative velocities, respectively, and θ the angle between v_{CM} and the emission direction. The distributions of the reacting ions affect the probability to find reactants in different velocity states, which will affect the values of v_{CM} , v_{rel} and θ . This means that the neutron energy spectrum in the solid angle Ω is obtained from integrating over the reactant velocity distributions according to

$$\frac{dN}{dE} = \frac{1}{4\pi} \iint_{\vec{v}_1 \vec{v}_2} f_1(\vec{v}_1) f_2(\vec{v}_2) \delta(E - E_n) v_{rel} \sigma(v_{rel}, \theta) d\vec{v}_1 d\vec{v}_2 d\Omega \quad (11)$$

where f_1 and f_2 are the reactant distributions, δ the Dirac delta function and σ the cross-section, dependent on energy and angle.

3.2 Neutron spectrum simulations using ControlRoom

The theoretical neutron spectrum at a set viewing angle from reactions between ions from two arbitrary velocity distributions f_1 and f_2 can be obtained by solving equation (11). The solution requires knowledge of the energy-dependent cross-section of the reaction and the equation is, depending on the complexity of the distributions involved, most conveniently solved using Monte Carlo methods. In this thesis, the Monte Carlo code ControlRoom has been used.

ControlRoom was developed by Luigi Ballabio based on the theory as outlined in [62], and first used (in an early form) to predict the ^4He knock-on contribution [63] which was later observed with the MPR [61]. This experimental observation of a predicted subtle effect serves as a solid benchmark of the code. ControlRoom samples given velocity distributions, energy and pitch angle ranges for the reacting ions and calculates the neutron spectrum at a viewing angle selected by the user based on equations (10) and (11). The pitch angle θ is the angle of the particle velocity relative to the magnetic field, i.e.,

$$\cos \theta = \frac{v_{\parallel}}{|\vec{v}|}. \quad (12)$$

The absolute emission rate as a function of energy is determined as in equation (4), combining the spectral information from equation (11) with given population densities. ControlRoom does not take density and temperature *profiles* into account and makes no line-of-sight integration.

Figure 7 shows example neutron spectra (normalized to their peak values) from ControlRoom at 90° viewing angle to the magnetic axis for JET heating conditions. In the simulations, it is assumed that $T_{\text{bulk}}=3$ keV, $n_e=3 \times 10^{19} \text{ m}^{-3}$ and $E_{\text{beam}}=110$ keV. Reactions between ions from the isotropic bulk population in thermal equilibrium lead to Gaussian neutron spectra centered at 2.5 MeV; here, this is exemplified with the narrow Gaussian from a 3-keV plasma.

Broader neutron spectra are obtained if auxiliary heating is applied. Reactions between bulk ions and ions from the slowing down of the 110-keV

beam used in this simulation give the double-humped (short-dash red) neutron spectrum in the figure that extends between 2 and 3 MeV. Beam-beam reactions give the dash-dot green spectrum, broadened in the region 2-3 MeV and with a peak shift towards higher energies. Beams at JET are injected at an angle around 60° to the magnetic field; this is taken into account in the simulations by sampling the pitch angle range $50\text{-}70^\circ$.

RF heated ion populations typically cover wider energy ranges and lead to broader neutron spectra. Here, this is exemplified with a spectrum from reactions between a 300-keV Maxwellian and bulk ions (dotted magenta) and reactions between bulk ions and ions from a theoretical distribution describing the application of $P_{\text{RF}}=0.5 \text{ MW/m}^3$ to a 110 keV beam seed (long-dashed blue). Since RF heating only affects the perpendicular velocity of the ions, RF distributions are characteristically anisotropic with pitch angles close to 90° . In these RF simulations, a pitch angle interval $80\text{-}100^\circ$ is sampled.

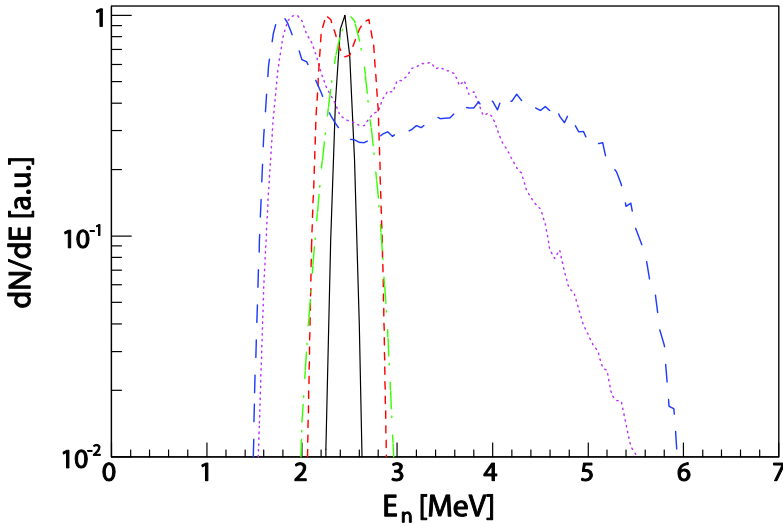


Figure 7. DD neutron spectra obtained with *ControlRoom* for thermonuclear reactions (solid black), beam-thermal reactions (short-dashed red), beam-beam reactions (dash-dot green), a 300-keV Maxwellian population reacting with the thermal bulk population (dotted magenta) and a theoretical distribution from 3rd harmonic RF on D beam seed reacting with the thermal bulk (long-dashed blue). Note that the distributions have been normalized to their peak values. (Color online)

In the analysis of TOFOR data, we have also found it useful to study the imprint of reactions between mono-energetic deuterons and bulk deuterons in the neutron spectrum (see e.g. papers IV and V). We call the theoretical neutron spectra resulting from such reactions δ spectra. Examples of δ spectra are given in Figure 8.

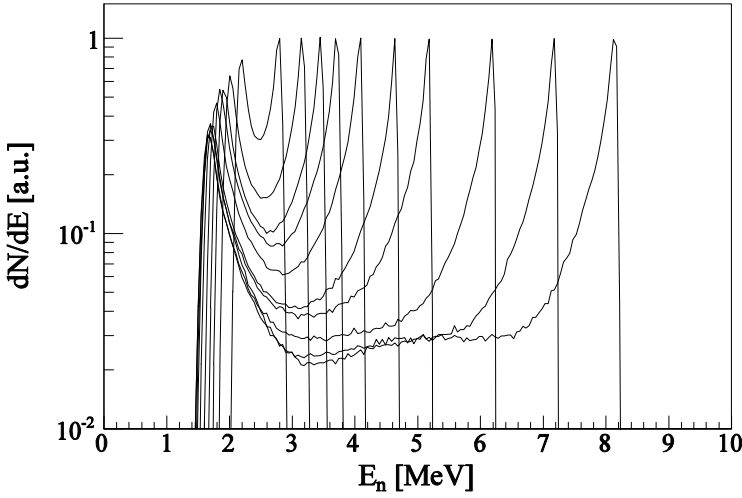


Figure 8. Neutron spectra from mono-energetic deuterons of 0.1, 0.3, 0.5, 0.7, 1.0, 1.5, 2.0, 3.0, 4.0 and 5.0 MeV energy reacting with deuterons from a 3-keV bulk population, in order of spectral broadening. Note that the distributions have been normalized to their peak values.

TOFOR views the plasma radially, with a viewing angle perpendicular to the magnetic field. For anisotropic ion distributions, such as those described by RF populations or by the slowing down population from beams, the viewing angle will affect the shape of the recorded neutron spectrum. In Figure 9, neutron spectra from beam-thermal reactions and from a 300-keV anisotropic Maxwellian reacting with the thermal population are shown both at 90° (solid lines) and 45° (dashed lines) viewing angles. As can be seen, the observable spectra at 90° viewing angle are significantly broader than those at 45°. This of course means that the line-of-sight of the observing instrument has to be taken into account in the analysis.

We use model neutron spectra such as the ones illustrated here to understand, analyze and interpret measured TOFOR data. The spectra obtained from ControlRoom are on a neutron energy scale. As described above, neutron spectrometers do not directly measure neutron energy. To convert the model spectra to a form understandable in terms of the measured parameters (time-of-flight in the case of TOFOR) knowledge of the instrument response function that relates the measured quantity to incident neutron energy is needed. The TOFOR response function will be discussed in section 4.2.1 and the models used to compare theoretical neutron spectra with measured data in section 3.4 below.

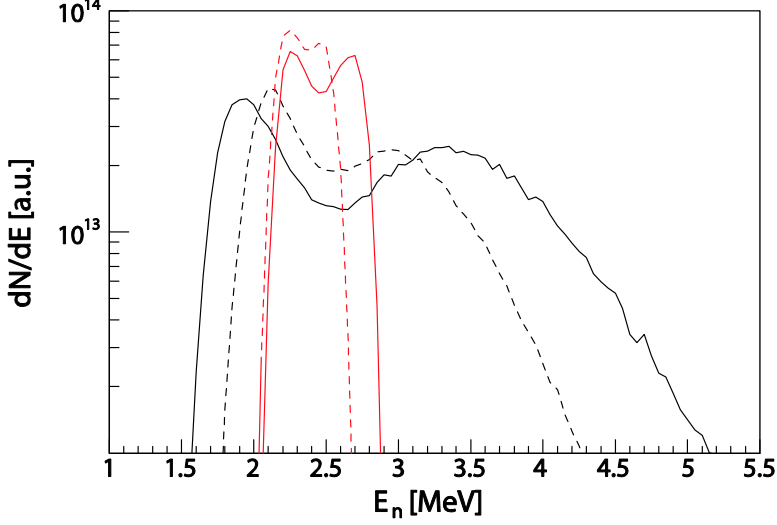


Figure 9. DD neutron spectra from beam-thermal reactions (red, narrow) and from reactions between a 300-keV Maxwellian population and the thermal bulk population (black, broad) at 90° viewing angle (solid lines) and 45° viewing angle (dashed lines). (Color online)

3.3 Scattered and direct neutrons

An important complication in neutron emission spectrometry is that not only neutrons emitted directly from the plasma in the direction of the detecting instrument will be recorded, but also neutrons that have scattered off the tokamak vessel wall into the line of sight. The scattered neutrons will be energy degraded compared to the direct ones; in the scattering process, the neutron will lose an energy

$$E_R = \frac{4A}{(1+A)^2} (\cos^2 \theta) E_n \quad (13)$$

to the recoil nucleus [64]. Here, A is the mass of the target nucleus divided by the neutron mass and θ the scattering angle. For a neutron spectrometer with a fixed line of sight, mainly neutrons scattered at around 180° angles (i.e., off the far wall) will be observed. For $\theta=180^\circ$, the scattered neutron energy is

$$E_n^{scatt} = E_n \left(1 - \frac{4A}{(1+A)^2} \right). \quad (14)$$

The scattered neutron spectrum will interfere with the measured direct neutron spectrum and complicate the analysis. As demonstrated in paper III, the scattered spectrum needs to be known for accurate interpretation of the measured data. In our work with TOFOR, the neutron transport calculation tool MCNPX [65] has been used to simulate the scattered component. The MCNPX simulations and results are discussed in detail in paper III. In Figure 10, the result from an MCNPX simulation for the TOFOR line-of-sight at JET using a quasi-monoenergetic (± 25 keV) 2.5-MeV neutron source is illustrated. The source is placed in the JET torus and the spectrum determined at a location corresponding to the position of the primary TOFOR detector. In the simulation for Figure 10, the neutron emission source profile from JET pulse 73311 is used (see paper III for details).

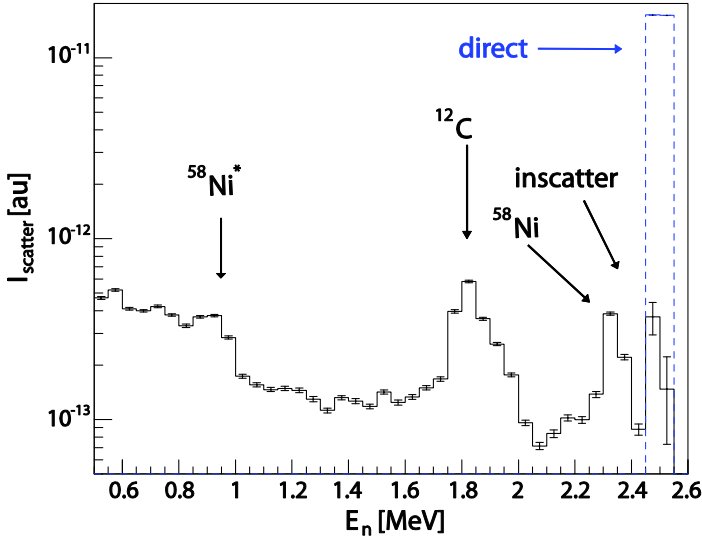


Figure 10. Scattered (solid black) and direct (dashed blue) neutrons incident on the primary TOFOR detector from a quasi-monoenergetic (2500 ± 25 keV) neutron source placed in the JET torus as determined using the MCNPX code. (Color on-line)

In the figure, the direct flux is represented by the dashed blue peak at 2.5 MeV and the scatter by the black curve. The error bars represent the statistical errors in each bin of the MCNPX simulation and are dependent on the number of particles simulated (in this case 50×10^6). Some features can be identified in the scattered flux curve. Underneath the direct peak, a small slightly down-shifted peak can be discerned – this can be interpreted as due

to small-angle inscatter in the line-of-sight. At about 1.8 and 2.3 MeV, two further peaks can be seen that represent scattering at around 180° (backscatter) at the bottom of the JET vessel against carbon and nickel, respectively. The small peak in the scatter component below 1 MeV represents scattering involving the first excited state of Ni. The shape of the scatter component has been found to be sensitive to the material composition used in the MCNPX model (paper III) – this means that accurate analysis of the neutron spectral data can only be performed if the viewing geometry and the involved materials are sufficiently well known. The MCNPX model of JET used incorporates information on the material composition of the vessel walls obtained from the JET drawing office for maximum accuracy.

3.4 Analysis methods

As has been mentioned, neutron spectrometers do not measure the neutron energy E but a secondary quantity M related to the neutron energy spectrum E through the instrument response function R according to $RE=M$. Retrieval of E from M , assuming R is known, is not a straight-forward problem.

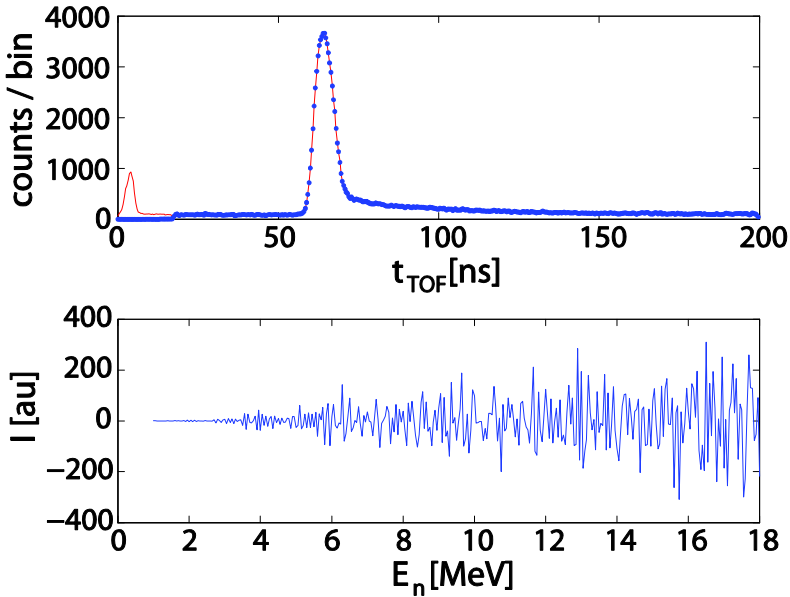


Figure 11. Example of TOFOR analysis through response function inversion. Upper panel: Original t_{TOF} spectrum for JET pulse 73311 (red curve), and t_{TOF} spectrum folded with R^{-1} , then back again with R (blue dots). Lower panel: E_n spectrum from folding the original t_{TOF} with R^{-1} . (Color online)

Inversion of R to get $E=R^{-1}M$ does not work, as exemplified in Figure 11. The expected neutron spectrum from the example TOFOR spectrum M_{ex} in the upper panel in Figure 11 (red curve, JET pulse 73311) is a superposition of the dash-dot, short-dash and solid curves from Figure 7. Folding M_{ex} with R^{-1} yields the nonsense neutron energy spectrum E_{ex} in the lower panel. However, folding E_{ex} with R nicely reproduces the original data (blue dots in the upper panel) except in the region of low t_{TOF} , representing neutron energies not covered by the current R of TOFOR.

One approach to the problem is to retrieve E from M using a so-called free unfolding method. Some established methods and the difficulties involved in this approach are discussed in [66]. Reasonable representations of the neutron spectrum can be obtained through free unfolding. However, in fusion, it is generally not the neutron spectrum itself that is the parameter of interest, but the underlying properties of the fuel ion distributions. If the neutron spectrum is obtained through unfolding, interpretation of the result in terms of fuel ion properties still remains.

In this thesis, the expected manifestation of the fuel ion distribution in the neutron spectrum is taken as the starting point in the analysis. Two main methods based on the same principle are used; component fitting and direct deuterium distribution unfolding.

3.4.1 Component fitting

The neutron emission from the JET plasma can be viewed as a superposition of components, each representing reactions between subpopulations of fuel ions. Examples of such components are the neutron spectra in Figure 7. TOFOR spectra are commonly analyzed through parameterizing this type of theoretical neutron spectra, folding them with the response function to get them on the scale of the measured data and fitting the parameters. This analysis approach was e.g. used for the analysis in papers II, III and VI.

The fit is performed using the method suggested by Cash [54], i.e., minimization of the metric

$$C = 2 \sum_{i=1}^N (x_i - n_i \ln x_i). \quad (15)$$

This method is in principle equivalent to the χ^2 minimization procedure used for Gaussian distributed experimental data, but it is derived for data following the Poisson distribution. Equivalent to reduced χ^2 , also a reduced Cash statistics metric can be constructed:

$$C_{red} = \frac{C}{\nu - p} \quad (16)$$

where $\nu - p$ is the number of degrees of freedom (i.e., in practice, ν the number of bins in the fitted interval and p the number of free parameters used in the fit). A value of $C_{red} \sim 1$ indicates a good fit.

A dedicated analysis tool, NES, is used for component analysis of TOFOR data. NES includes pre-parameterized components representing the neutron emission from thermonuclear reactions, beam-thermal reactions, and reactions between thermal and simplified iso- or anisotropic RF populations. The thermonuclear neutron spectrum is represented with a Gaussian defined by intensity and width $\sigma = 35.0 T_d^{1/2}$ (cf eq. (9): $\Delta E_n = 2(2 \ln 2)^{1/2} \sigma$), the beam-thermal neutron spectrum with a “box” in ion energy space defined by intensity and maximum and minimum beam distribution ion energies, and the simplified thermal-RF neutron spectra with Maxwellians defined by temperature and intensity. It is also easy for the user to add fixed shape components with the intensity as a free parameter, based on theoretical estimates of neutron spectra from specific plasma scenarios.

3.4.2 Deuterium distribution unfolding

The Maxwellian components used to represent reactions between bulk and RF heated ions as described above are often not a satisfactory representation of the RF ion population. They give an idea of what fraction of the neutrons originates from this population, but are in general too simplified to give a fair representation of the RF heated deuterium distribution. In papers IV and V, a method is used where the deuterium distribution from RF heating is obtained directly from the high-energy tail in the TOFOR spectra through fitting neutron spectra from mono-energetic deuterons reacting with the bulk population (δ spectra, as in Figure 8) to the data. We call this “deuterium distribution unfolding”.

The δ spectra are generated assuming $90^\circ \pm 10^\circ$ pitch angle (see section 3.2) for the ions; this limits the application of the method in its current form to RF populations, for which this assumption is valid. Also this method utilizes Cash statistics. The number and deuterium energies of the δ spectra used are selected to match the resolution of the data. A δ spectrum representing a single deuterium energy E_d extends from low to high neutron energies as seen in Figure 8. For this reason, each iteration of the fit starts with varying the intensity of the highest energy δ spectrum. The intensity in this point is then fixed, and the intensity of the next δ spectrum varied etc. A smoothing prior is enforced to avoid reproducing statistical fluctuations. The errors in each point are deduced by varying the intensity in that point until C from equation (15) increases by 1, while allowing the intensity values of the

four surrounding points to vary and keeping the intensities of all other points fixed.

The experimental deuterium distributions deduced in this way can be compared with simplified theoretical distributions derived using Stix's solution to the Fokker Planck equation as in section 1.3.3 above. Good agreement has been obtained, as illustrated e.g. in paper V.

4 TOFOR

Ja vad säger man – världsklass!

Anders Hjalmarsson

TOFOR (JET name KM11) is a time-of-flight (TOF) spectrometer optimized (O) for high-rate (R) detection of 2.5 MeV neutrons from DD reactions. It was constructed based on neutron transport simulations using the GEANT4 tool as discussed in [67]. The instrument setup is described in detail in papers I and II. Here, a short introduction will be given to give the reader the basic information needed to follow a discussion on work done to improve the understanding of the instrument and the accuracy in the analysis.

Neutrons enter TOFOR from below (Figure 12a). The flight time is measured between an in-beam scattering detector S1 and a secondary removed detector S2, placed on the constant time-of-flight (TOF) sphere (Figure 12b) from S1 with center-to-center flight times related to the incident neutron energy as $E_n = 2mr^2/t_{\text{TOF}}^2$ (derived in paper II).

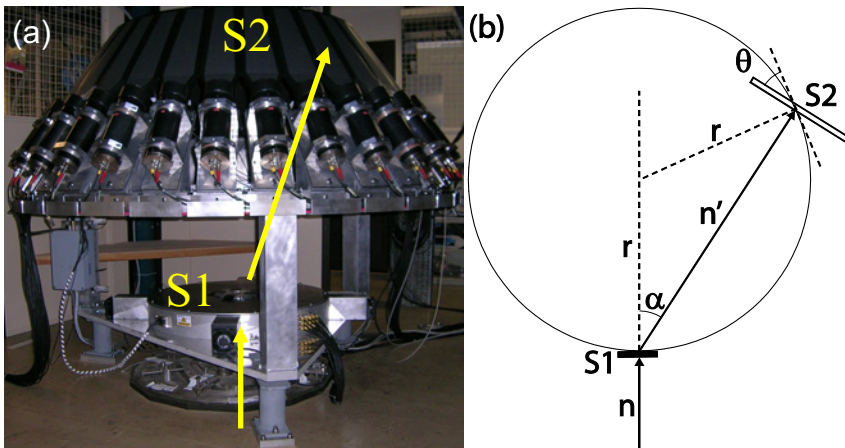


Figure 12. (a) Picture of the TOFOR instrument in place in the JET roof laboratory, with in-beam (S1) and secondary (S2) detectors indicated and (b) schematic of the setup, showing the S1 and S2 detectors located on the constant time-of-flight sphere ($r=705$ mm, $\alpha=30^\circ$, $\theta=5^\circ$). (Color online)

The S1 and S2 detectors consist of 5 and 32 plastic scintillators, respectively, and the neutrons are detected through their interaction with protons in elastic n,p scattering as discussed above (section 2.1). The energy deposited by the proton (recoil energy) is converted to a light pulse in the scintillator, which

is in turn converted to an electric pulse in a photomultiplier (PM) tube and fed to the electronics. Events with pulse height below a discrimination level set using constant-fraction discriminators (CFD) are rejected. For all events of sufficient pulse height, a time stamp is recorded using digital data acquisition boards with 0.4 ns bins. One board channel is dedicated to each detector, and an additional two channels record clock pulses from JET for calibration purposes as described in detail in paper II.

The integrated charge of the pulse is recorded in the form of an increment in the corresponding bin of a histogram of analogue-to-digital converter (ADC) data. Currently, only two ADC spectra per detector are recorded in connection with each JET pulse: A calibration spectrum with two seconds of light-emitting diode (LED) data collected during the initialization phase, and a data spectrum with the neutron signal data integrated over the full length of the JET plasma discharge. This means that it is currently not possible to correlate individual time stamps to the proton energy of the event that generated them. An upgrade of TOFOR is being considered where the time boards might be replaced with so-called hybrid boards, collecting pulse shapes with the required sub-nanosecond time resolution.

Rate optimization of TOFOR is achieved mainly with the use of the time boards, which have the ability to record events without dead-time, and the segmentation of the in-beam detector in 5 layers, spreading the count rate over a larger number of photomultiplier tubes. Without the segmentation, the count rate capability of the PM tubes would be a limiting factor. So far, the projected count rate limit of TOFOR of the order of 0.5 MHz (paper II) has not been possible to test; the record rate recorded is a true neutron event rate of 44 kHz during 1.5 s of JET pulse 79691 (with total neutron rate $R_n \sim 1.7 \times 10^{16}$ n/s as measured by the JET fission chambers).

The optimization for detection of 2.5 MeV neutrons is achieved through geometrical considerations. Also, the n,p scattering cross section decreases with energy, making detection of higher energy neutrons less efficient. The *efficiency* of TOFOR is optimized for 2.5 MeV neutrons through careful selection of the S2 angular coverage (Figure 12b). The interval covered is selected to include as large a fraction of detectable scattered 2.5 MeV neutrons as possible, without being so large as to introduce unnecessary timing uncertainties or become impractical and expensive to construct. Examples of proton recoil energies deposited in S1 for incident neutrons of varying energy for the maximum and minimum scattering angles covered by S2 are given in Table 2. As can be seen, 2.45 MeV neutrons that scatter from S1 to the tip of S2 (23.02°) will deposit $E_p = 375$ keV in S1. We have aimed at setting the discrimination threshold to 380 keV to achieve full efficiency for 2.45 MeV neutrons while excluding noise. The choice of thresholds affects the neutron energy-dependent detection efficiency of TOFOR as described below in section 4.2.2.1; the discriminator levels can be tuned to match the plasma scenario studied as discussed in section 4.4.

Table 2. Deposited proton recoil energy in S1, E_p^{S1} , and remaining scattered neutron energy, E_n , for neutrons of incident energy E_{in} that scatter in S1 through the maximum and minimum angles covered by S2.

E_{in} [MeV]	37.87° scatter (S2 base)		23.02° scatter (S2 tip)	
	E_p^{S1} [MeV]	E_n [MeV]	E_p^{S1} [MeV]	E_n [MeV]
1	0.377	0.623	0.153	0.847
2	0.754	1.246	0.306	1.694
2.45	0.923	1.527	0.375	2.075
3	1.131	1.869	0.459	2.541
4	1.507	2.493	0.612	3.388
5	1.884	3.116	0.764	4.236
6	2.261	3.739	0.917	5.083
7	2.638	4.362	1.070	5.930
14	5.276	8.724	2.141	11.859

The *resolution* of TOFOR is optimized for 2.5 MeV neutrons through selection of a tilting angle for S2 (θ in Figure 12b). The finite size of S2 (35 cm length) means that the recorded S2 time will include both the neutron flight time as well as the light transport time through the scintillator to the PM tube.

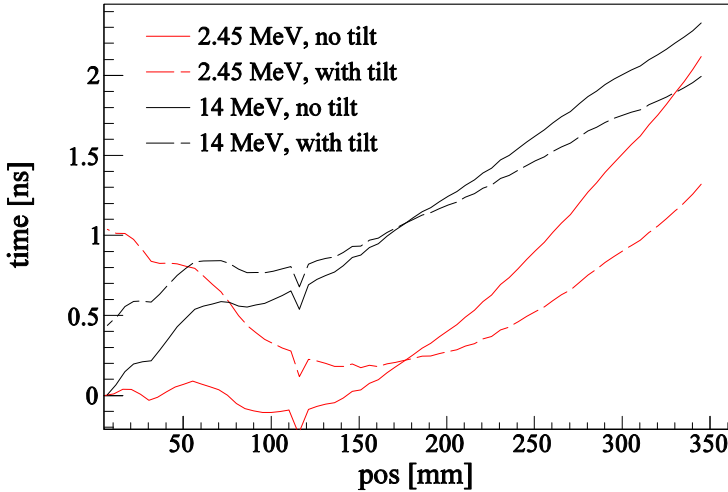


Figure 13. Spread in detection time as a function of interaction position in S2, for 2.45 MeV (red) and 14 MeV (black) neutrons, without tilt (solid lines) and with a 5° S2 tilt (dashed lines). The spread is determined as the sum of the interaction point dependent flight time plus S2 light transport time, minus the total time to the base of S2 in the untilted case. (Color online)

To compensate for this, the detectors are tilted relative to their reference location on the constant TOF sphere to reduce the flight time to the tip of the detector and increase the flight time to the base of the detector. This tilt will improve the timing resolution for incident neutrons of all energies but is optimized for neutrons of 2.5 MeV as illustrated in Figure 13. In the 2.45 MeV case, the spread is reduced from more than 2 ns before introduction of the tilt to about 1 ns with tilt, while in the 14 MeV case, the tilt reduces the more than 2 ns spread to about 1.5 ns.

The time-of-flight (t_{TOF}) spectrum measured by TOFOR is constructed post-pulse from the individual time traces of events recorded on the digital time boards for each S1 or S2 scintillator as illustrated in Figure 14.

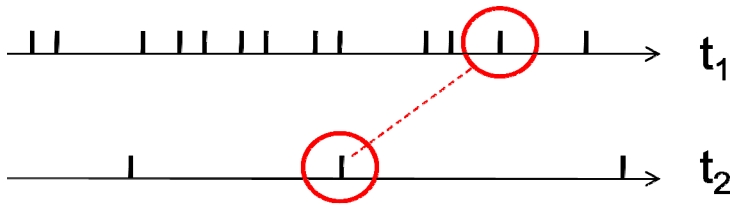


Figure 14. Principle of t_{TOF} spectrum construction: An event is selected in the time trace t_2 of the S2 detector, and paired up with matching events in the S1 time trace t_1 that fall within a selected time window. (Color online)

Fewer events are recorded in the removed detector S2, since S1 is placed in-beam. Only a fraction of the neutrons that scatter in S1 go in the direction of S2, and even fewer undergo scatter in S2. The S2 time trace is taken as the starting point for which matching events in S1 are sought within a set time window (currently ± 400 ns). Both true and random coincidences will be constructed in this way. 160 individual S1-S2 t_{TOF} spectra are constructed; these are summed to make up the total spectrum. It is of course important that the detectors are time aligned relative to each other to avoid introducing further broadening at this stage; this issue will be discussed in detail below.

Examples of t_{TOF} spectra recorded with TOFOR are given in Figure 15. Since random events are uncorrelated in time, they will show up as a flat level across the t_{TOF} spectrum with intensity proportional to the count rate in the S1 and S2 detectors, i.e., the random level is proportional to the square of the incident neutron flux F_n . The true coincidence count rate will be linearly dependent on F_n , meaning that the true/random ratio will be worse for pulses with high neutron rates, with the result that low-intensity features of the spectrum will be harder to resolve in this case. In Figure 15, two examples are given: a t_{TOF} spectrum from the RF-only heated period of JET pulse 73205 with low count rate (red), and from NB heated pulse 73311 with high count rate (black). For both examples, the true 2.5 MeV neutron peak shows up around $t_{\text{TOF}}=65$ ns. The peak at 4 ns corresponds to true γ events. The

random level has not been subtracted in either case and can be seen to be two orders of magnitude higher in the high-intensity case. Since the random level is flat, it is straightforward to determine it through fitting in a region with no physical events; we have selected the region -40 to -80 ns to routinely perform this fit. The random level is commonly subtracted when data are visualized. Note, however, that the randoms are not subtracted but treated as a fixed component in the data analysis.

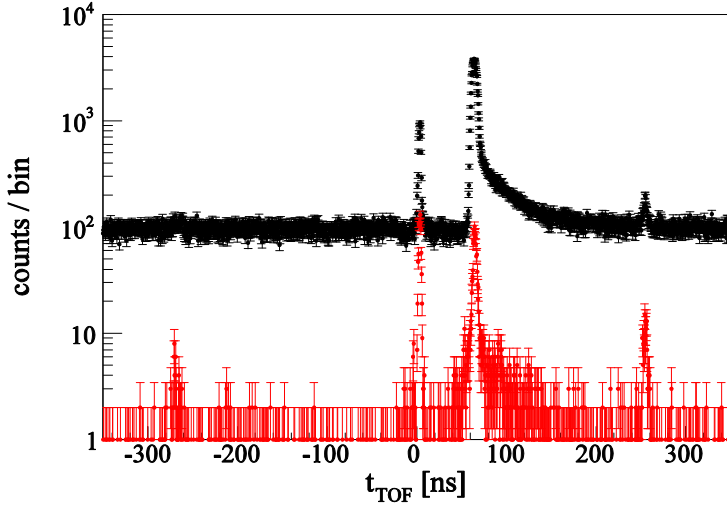


Figure 15. Non-background subtracted data from 73311 (top, black) and 73205 (47-50.5 s) (bottom, red). (Color online)

The small peaks at about 270 and -270 ns in Figure 15 have been found to be due to reflections of large pulses in the signal cables and do not interfere with the interesting part of the spectrum. It could be noted that also background events, due to e.g. ambient γ radiation and observed in S2 on a level of about 100 Hz due to their large volume, will contribute to the random level in the recorded t_{TOF} spectrum.

4.1 Line of sight

TOFOR is located in the roof laboratory at JET and views the central part of the plasma with a perpendicular (vertical) line-of-sight (Figure 16). The field of view is restricted by a 2 m collimator through the roof lab floor, the pre-collimator structure and the upper vertical diagnostic port. The coordinate systems for the JET roof laboratory and torus hall are not matched up and no exact line-of-sight information can be obtained from the JET drawing office;

currently our best estimate is an umbral foot print (viewed from the center of S1) at the torus midplane from major radius $R=2.74$ to 3.02 m, centered at $R=2.88$ m. The corresponding numbers at the divertor level are 2.69 , 3.00 and 2.85 m, respectively.

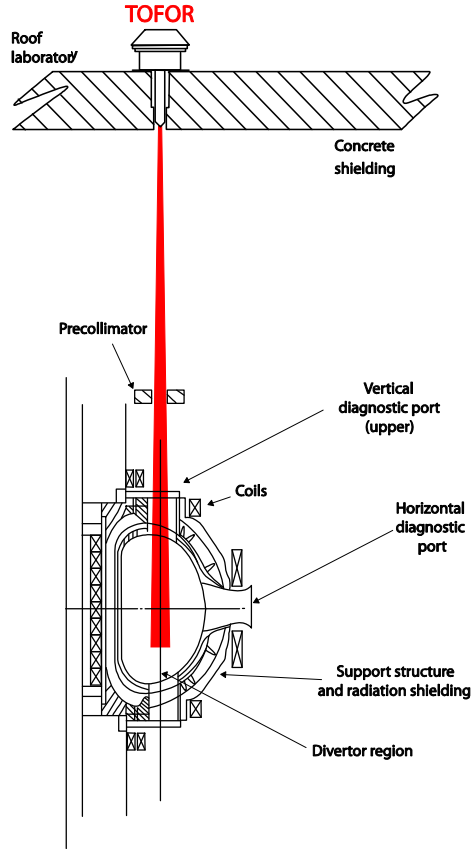


Figure 16. Poloidal cross section of JET in octant 8 with the TOFOR line-of-sight from its location in the roof laboratory indicated. (Color online)

The line-of-sight information is crucial in the determination of the expected scattered neutron flux in the TOFOR line-of-sight. A detailed description of how the line-of-sight estimate was deduced can be found in paper III, where measurements using super-heated fluid detectors [68] are also invoked to confirm the estimate.

The precollimator consists of four concrete jaws, two movable in the radial direction and two in the toroidal direction. The purpose of the system is to allow for restriction of the line-of-sight if the neutron flux from the plasma is too high for the detecting instrument. A crucial point in the TOFOR line-of-sight estimate is the result from the installation survey that a precollimator

outer radial jaw set to 54.5 mm blocks half the line-of-sight (see paper III). This survey result was confirmed in a set of measurements where the precollimator outer jaw was gradually moved from fully open (143.3 mm) to fully closed (0 mm) as visualized in Figure 17. Here, KM11 represents true neutron counts in the t_{TOF} spectrum from TOFOR, and KN1 the total neutron yield as measured by the JET fission chambers. The linear fit to the data gives a value for KM11/KN1 at 54.5 mm of 0.48 ± 0.002 times that at fully open.

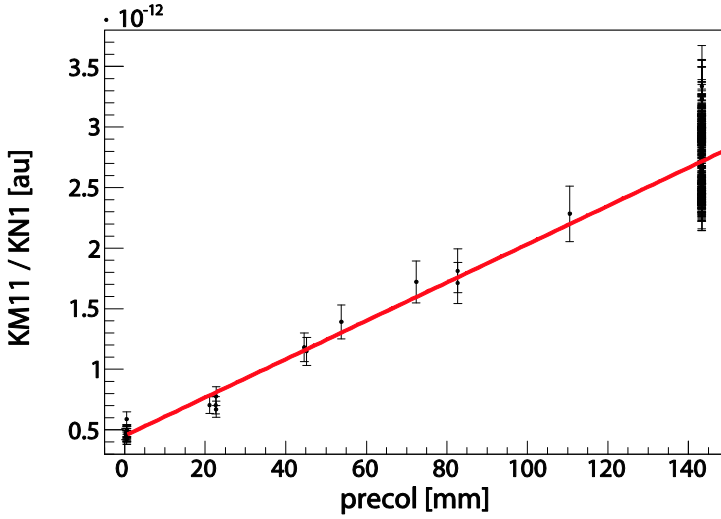


Figure 17. TOFOR counts (KM11) divided by fission chamber neutrons (KN1) for a number of JET pulses shown as functions of setting of the precollimator outer jaw. Also shown is a linear fit to the data points. The outer jaw is fully open when set to 143.3 mm. (Color online)

4.2 TOFOR response

As mentioned, S1-S2 center-to-center flight times in TOFOR are related to the incident neutron energy as $E_n = 2mr^2/t_{\text{TOF}}^2$ (constant TOF sphere equation). However, the measured flight time will deviate from this ideal value due to the finite size and flat geometry of the detectors, and due to the possibility of neutrons scattering multiple times on their way from detection in S1 to S2. These effects are of crucial importance for accurate analysis of the recorded data and a full response function of TOFOR has been simulated to take them into account (see section 4.2.1 below). This simulated response function will describe the geometrical response, R_n , of TOFOR due to the setup of the detectors and the surrounding structures. However, the measured representation of the spectrum of incident neutron energies will also be af-

affected by other factors which in paper II were classified as pulse response, R_p . This pulse response is affected by the finite resolution by which the event times can be measured in the electronics as well as other peculiarities of the instrument, and the contributing factors will be discussed in some detail in section 4.2.2 below.

In summary, the total response of TOFOR will, in addition to the geometrical response, be affected by:

- The thresholds set in the electronics to select which pulses to record.
- The time alignment of the individual scintillator channels.
- An additional broadening due to imperfections in the data acquisition electronics.

4.2.1 Response function

The geometrical response of TOFOR was simulated using GEANT4 as described in [67], to create what we call the TOFOR response function. The time-of-flight response of TOFOR to quasi-monoenergetic (± 25 keV) neutrons in 50 keV intervals was simulated, originally in the range from 1-5 MeV. For this thesis, the simulations were extended to cover the range of incident neutron energies from 1-18 MeV; this was found necessary as the analysis tools improved and as new plasma scenarios emerged where higher energy neutrons could be studied, e.g. the ${}^9\text{Be}({}^3\text{He}, n){}^{11}\text{C}$ neutrons discussed in paper VI.

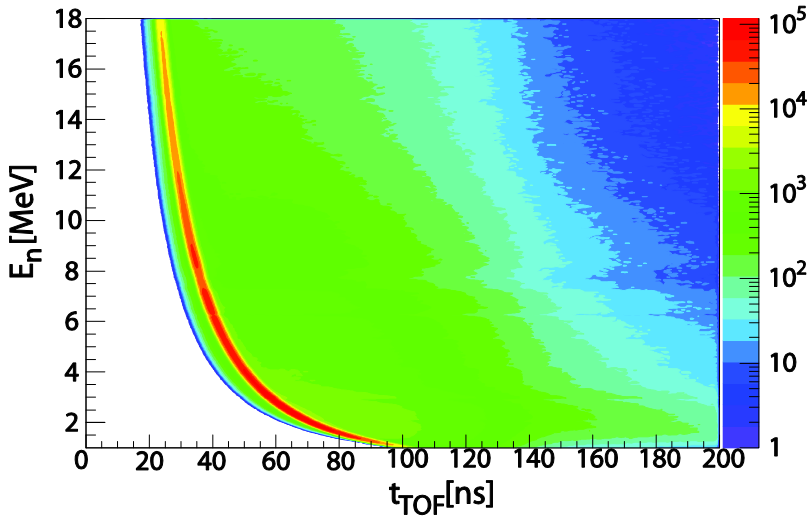


Figure 18. TOFOR response function, showing the simulated time-of-flight spectrum for incident neutron energies in the range 1-18 MeV.

The response function, made up of a t_{TOF} spectrum for each simulated incident neutron energy, is illustrated in Figure 18. The red crescent represents the most likely flight times for each neutron energy, corresponding to the equation of constant TOF.

From the response function, the expected efficiency as a function of neutron energy can be determined by summing all events in the t_{TOF} spectrum in each E_n bin (Figure 19). 10^8 incident neutrons were simulated for each energy; in Figure 19, the intensities from Figure 18 have been normalized using this number. As can be seen, the efficiency peaks at 0.01 coincidences per incident neutron for 2.5 MeV neutrons, and decreases by almost a factor of 10 for 14 MeV neutrons. The plastic scintillators contain C and H and n,p scattering competes with n,C scattering. The structures seen in the response function correspond to resonances in the n,C scattering cross section that increase the n,C scattering probability at the expense of n,p scattering for those energies.

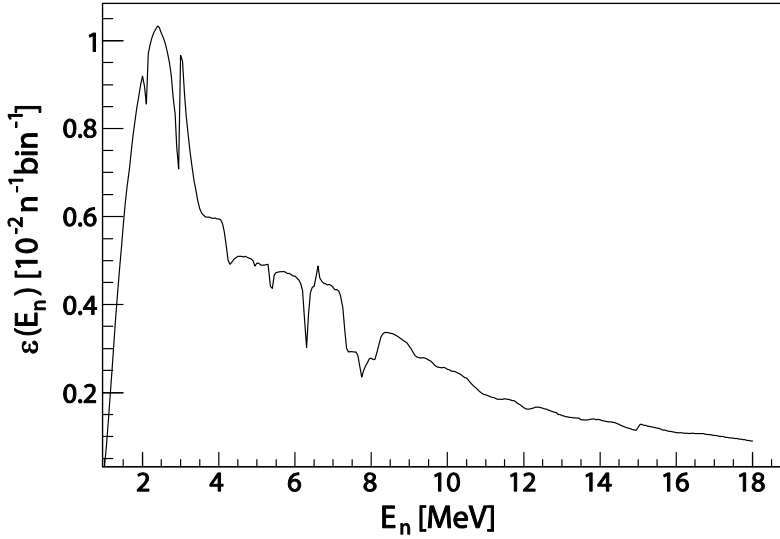


Figure 19. Efficiency of TOFOR for detection of neutrons of different incident energies, as determined from summing the events in the simulated t_{TOF} spectra in Figure 18.

In the simulations, the proton energy E_p and the event time t for all interactions are recorded. In order to match the response function to the measured data, the same discrimination thresholds used in the measurement need to be applied also to the simulated response function, in units of proton energy.

4.2.2 Instrument characteristics

The total response of TOFOR is determined by the response function, describing the geometrical response as discussed above, with input on (i) discriminator thresholds in units of proton energy, (ii) the time alignment of the detectors and (iii) an additional broadening due to finite resolution in the electronics. In this section, we will discuss each of these topics.

4.2.2.1 Thresholds

The thresholds are set in the CFDs of the TOFOR data acquisition electronics in the form of a pulse height level on a mV scale. The response function, as mentioned, requires input thresholds on an E_p scale. The mV thresholds are converted to energy levels using the analogue ADC branch of the TOFOR electronics. ADC data are collected with a ^{22}Na source placed on top of the S1 detector. The decay of ^{22}Na leads to emission of a 0.546 MeV β^+ and a 1.275 MeV γ . With the positron annihilating to two 511 keV γ -rays, the decay will give rise to two Compton edge signatures in the ADC spectra. Consequently, there will be three points of known energy in the spectrum: the pedestal at $E_c=0$ keVee and the two Compton edges at 1062 keVee and 341 keVee, respectively. This means the energy scale (channel to “keVee”, electron equivalent energy from the Compton scattered electron recoil) of the ADC spectrum can be determined, assuming a strictly linear correlation between light yield and energy. The threshold level in channel number can then be read out from the spectrum and converted to keVee.

One complication of this scheme is that the ADCs suffer from differential non-linearity (DNL) which has to be corrected for. The DNL for each individual detector ADC channel has been determined using a triangular wave generator of sufficient amplitude to scan the range of possible pulse heights, gating the ADC with uncorrelated pulses from a pulse generator. Examples of such DNL spectra, for detector S1-2, are shown in the top panel of Figure 20. The three curves represent measurements from 2006, 2007 and 2009, respectively. The amplitude depends on collection time and is not relevant. To compare the spectra from the different measurement times, the integral non-linearity (INL) in the three cases has been constructed and normalized to its maximum (middle panel). By dividing the normalized INL from the different measurements, the DNL drift can be determined for each channel (bottom panel). As can be seen, a 5% difference is observed for low channel numbers both if the 2006/2007 (magenta) and the 2007/2009 (black) measurements are compared. The conclusion is that there are drifts in the DNL and regular measurements are needed to keep the DNL corrections up-to-date.

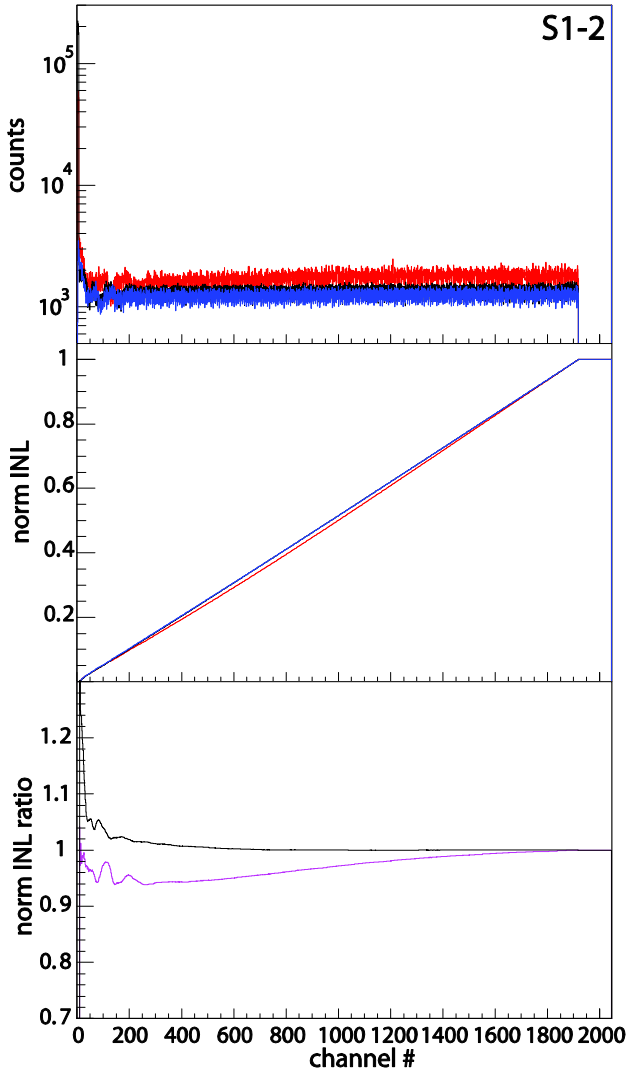


Figure 20. Non-linearity of the ADC channel used for S1-2 data. The top panel shows the DNL spectra collected with a triangular pulse generator in November 2006 (red), October 2007 (blue) and June 2009 (black). The central panel shows the normalized INL from the same measurements. The bottom panel shows the 2006 INL divided by the 2007 INL (magenta) and the 2007 divided by the 2009 (black).

Another complication in the determination of the thresholds using ^{22}Na is that the spectra need to be corrected for background. In Figure 21, raw ^{22}Na (blue) and background (red) spectra collected with S2-5 over 48 hours each are shown. The black curve shows the resulting background subtracted linearized ADC spectrum used for threshold determination.

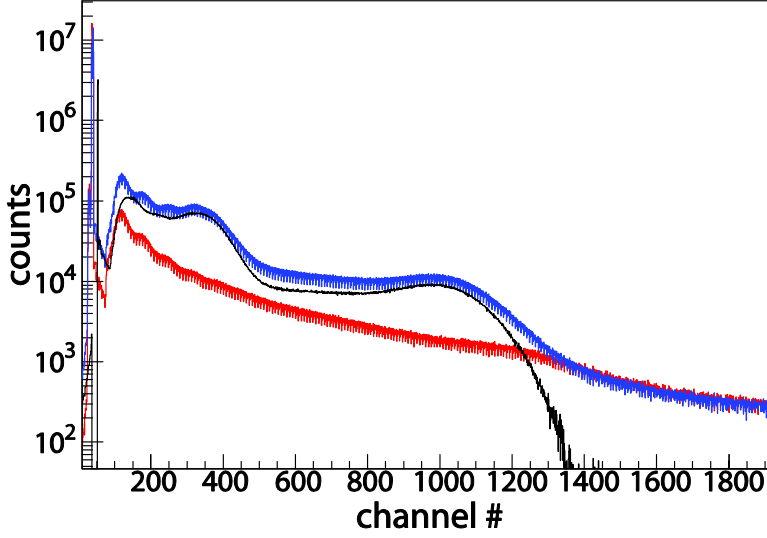


Figure 21. ^{22}Na (blue) and background (red) spectra measured for 48 hours with S2-5. Also shown is the resulting linearized and background subtracted ^{22}Na spectrum (black).

Currently, the pedestal is determined through fitting a Gaussian, while the Compton edges are determined by inspection, assuming that the actual Compton edge corresponds to the half-height. However, it has been shown that for different scintillator materials, the half height does not necessarily represent the true value of the Compton edge [69,70,71,72]. In theory, it should be possible to achieve a more systematic ADC spectrum energy calibration through fitting to the ^{22}Na data. This has been tried, taking into account the positions and intensities of the Compton edges, the pulse height resolution of the detector and the attenuation of the light due to the detector geometry. The fit function consists of a basic linear energy scale function on the form $y=mx+c$, with intensities of Compton edges 1 and 2 and the pileup from simultaneous interaction of both gamma energies emitted in a ^{22}Na decay, folded with the pulse height resolution on the form [69]

$$\frac{\Delta L}{L} = \left(\alpha^2 + \frac{\beta^2}{L} + \frac{\gamma^2}{L^2} \right)^{\frac{1}{2}}. \quad (17)$$

An example of a fit to S1-4 ^{22}Na data using this method is shown in Figure 22.

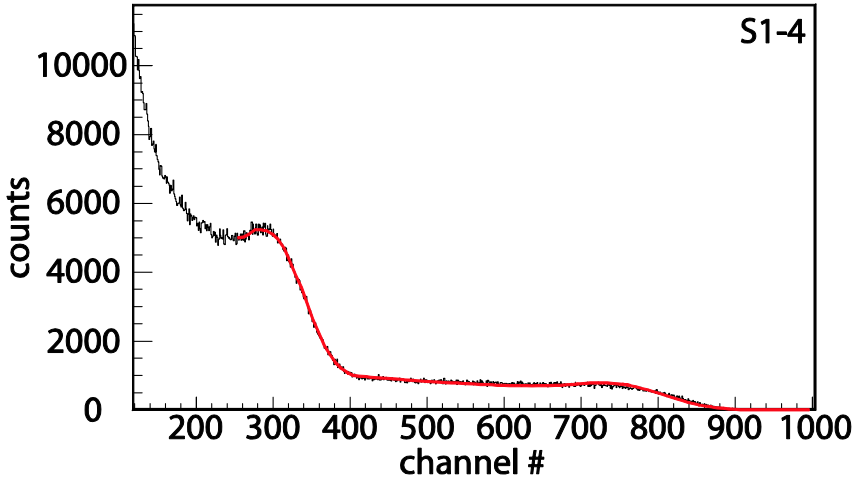


Figure 22. Fit to linearized background subtracted ^{22}Na data for S1-4.

Examples of comparisons between fits and inspection are given in Table 3. As can be seen, the results from fits to and inspection of S1 spectra closely match each other, with the edge position from the fit falling between the peak and half-height of the first Compton edge (C1) from inspection, close to the half-height. However, in the S2 case, the fitted C1 edge falls above the half-height (further to the right in the spectrum). This is not expected from the references and is not understood at this point.

Table 3. Results from comparison between Compton edge position results for the first Compton edge (C1) (at 341 keVee) from inspection and fit to ^{22}Na data. For the five S1 detectors listed, the fitted Compton edge position approximately coincides with the half-height. For the three S2 detectors, the Compton edge position resulting from the fit lies above the half height.

Detector	C1 peak (inspection)	Half-height (inspection)	C1 pos (fit)	Fit pos above peak	Fit pos below half-height
	[ch]	[ch]	[ch]	[%]	[%]
S1-1	239	292	286	19.7%	2.0%
S1-2	165	201	196	18.6%	2.7%
S1-3	225	271.5	266	18.4%	1.9%
S1-4	281	344	338	20.2%	1.8%
S1-5	245	297.3	291	18.9%	2.0%
S2-2	321	407	439	36.7%	-7.8%
S2-3	311	385	419	34.6%	-8.7%
S2-4	346	427	465	34.4%	-8.9%

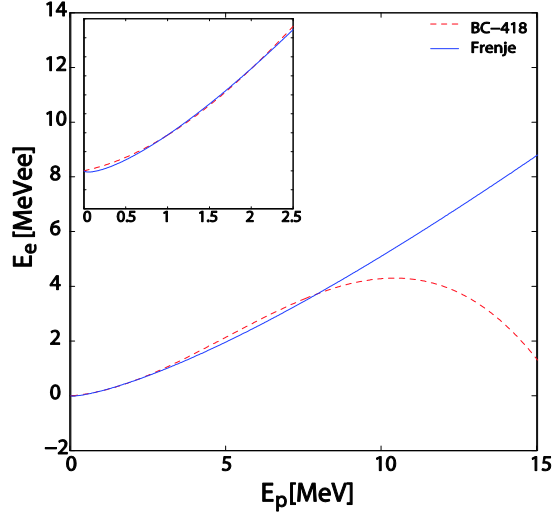


Figure 23. Comparison of E_e - E_p conversion formulas from ref. [73] (BC-418, dashed red) and [74] (Frenje, solid blue). (Color online)

The ^{22}Na method yields the threshold in units of keVee. The response function, as has been mentioned, needs threshold input in units of E_p . To achieve the needed conversion, the relation [73]

$$E_e = 0.093159 \cdot E_p + 0.101399 \cdot E_p^2 - 0.006787 \cdot E_p^3 \quad (18)$$

has been used. In Figure 23, this formula is compared with one used by Frenje in ref [74]. As can be seen, the two curves follow each other closely in the low energy interval ($E_p < 3$ MeV) that we are interested in here. However, the conversion adds to the uncertainty of the threshold determination.

The goal is to set the discriminator threshold to the same keVee level for all detectors; this makes the response function generation easier. The recent target threshold has been $E_p = 380$ keV, corresponding to $E_e = 50$ keVee. It is estimated that the uncertainty in the threshold determination is ± 10 keVee. In Figure 24, the TOFOR efficiency as a function of incident neutron energy is shown, varying the thresholds for both S1 and S2 ± 10 keVee, i.e. from $E_p = 320$ keV to $E_p = 440$ keV, in steps of 20 keV. As can be seen, the difference between the efficiency in the two extreme cases of $E_p^{S1} = E_p^{S2} = 320$ keV and $E_p^{S1} = E_p^{S2} = 440$ keV is almost $\pm 20\%$ for 2.5 MeV neutrons.

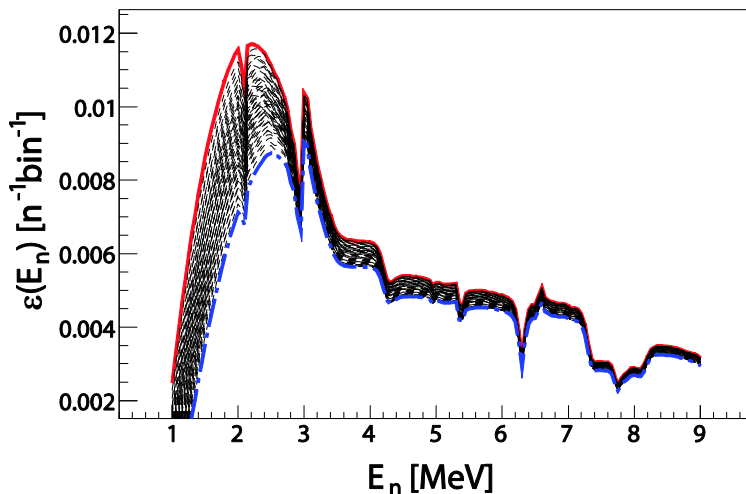


Figure 24. Efficiency as determined from integrating the t_{TOF} spectra in the response function, varying the threshold settings in steps of 20 keV from $E_p=320$ keV in both S1 and S2 (solid red curve) to $E_p=440$ keV in both S1 and S2 (broken blue curve). (Color online)

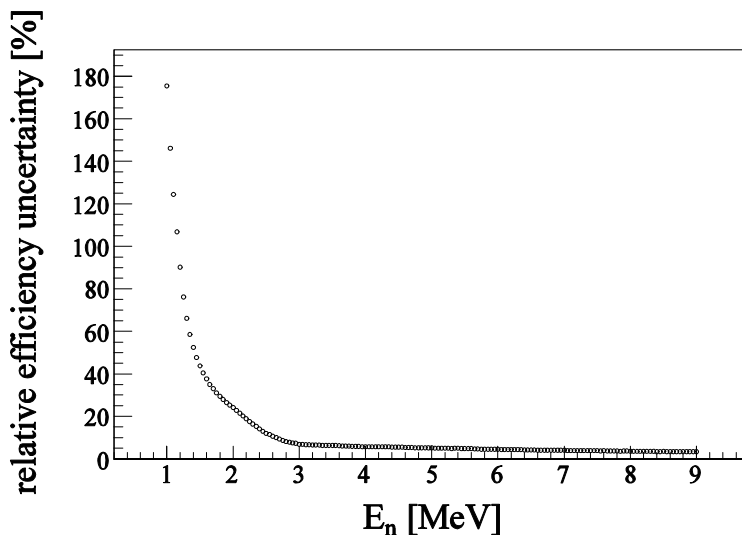


Figure 25. Relative uncertainty in the TOFOR efficiency as a function of incident neutron energy, determined as the percentage deviation from the average of one of the extreme points in Figure 24.

In Figure 25, the relative efficiency uncertainty, determined as the percentage deviation from the average of one of the extreme points, is shown as a function of energy. As can be seen, the uncertainty is highest for low ener-

gies; this is of course to be expected since the threshold cut affects the lowest energies the most. The natural consequence is that the thresholds also affect the shape of the response function, which will have an impact on the achievable accuracy in the data analysis performed using the response function. This is exemplified in Figure 26.

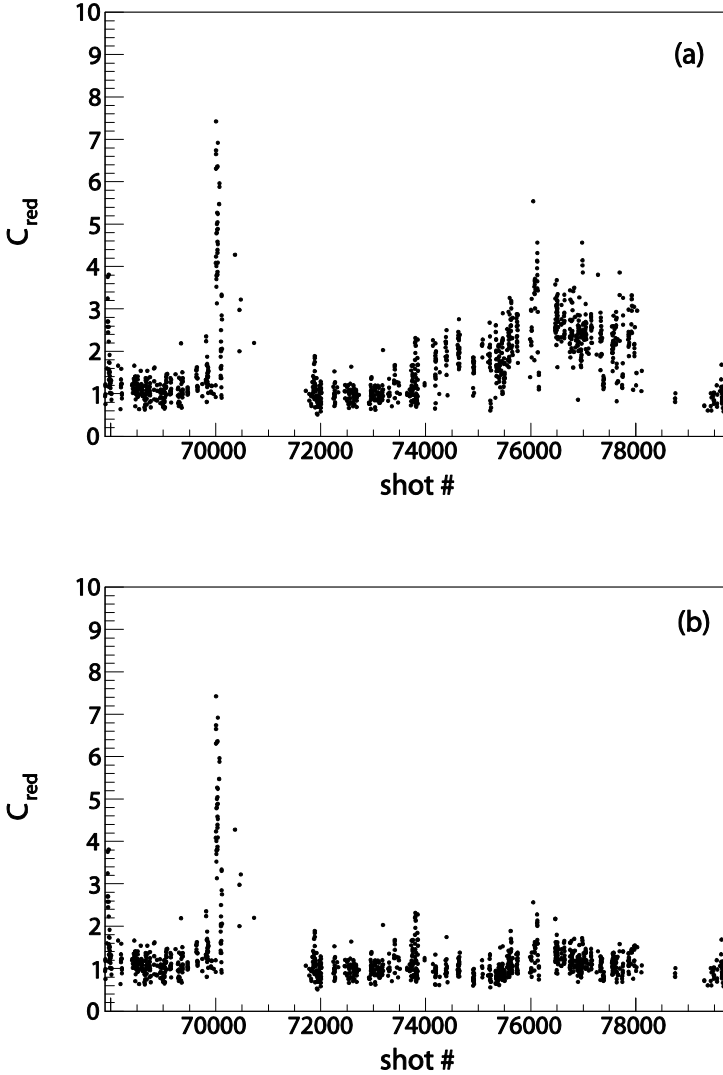


Figure 26. (a) C_{red} from fits to TOFOR data from JET pulses with $P_{NB} > 10$ MW and no applied RF heating. (b) Same as in (a), but with a different response function used in the pulse interval 74000-78200 as described in the text.

The figure shows the Cash statistics goodness of fit parameter C_{red} from fits to data from JET pulses with $P_{\text{NB}} > 10$ MW and no RF heating applied. The data set was selected based on the criteria of small variations in the neutron emission conditions, to facilitate routine fitting with similar parameters, and good statistics in the TOFOR data. The data in the two panels can be divided in four intervals: (i) 68000-71000, (ii) 71000-74000, (iii) 74000-78200 and (iv) 78200-79000. The intervals correspond to time periods with different threshold settings and, hence, different response functions. In time period (i), a response function with lower and upper thresholds for S1 and S2 of 320, 2300, 540 and 2580 keV is used. Time period (ii) uses lower thresholds of 380 keV for all detectors. In time period (iv), a different low threshold is used for each of the 5 S1 detectors, while the S2 low thresholds are set to 380 keV.

At around shot 74000 in panel (a) of Figure 26, the C_{red} values can be seen to start deteriorating. This is believed to be due to drifts in the effective E_p thresholds. Time periods (ii) and (iii) belong to the same set of JET campaigns. The thresholds were calibrated before the start of these campaigns. In Figure 26a, the deduced response function is applied in the analysis throughout periods (ii) and (iii). After the end of these JET campaigns (~ 78200) a new ^{22}Na measurement was done to determine the new threshold settings. Unfortunately, the measurement was done after TOFOR had been switched off for some two months, meaning it is not clear how well the new thresholds actually match the campaign settings. However, when the new response function is applied from 74000-78200, a dramatic improvement in C_{red} is seen (Figure 26b). Consequently, this response function is used when data from time period (iii) are analyzed.

As mentioned, also upper thresholds were used in the TOFOR setup in period (i), i.e., during the first campaigns after installation of the instrument at JET. By only accepting pulse heights within a window with lower and upper bounds, the randoms level for 2.5 MeV neutron measurements could be suppressed. TOFOR was in this way further optimized for 2.5 MeV neutron measurements. However, the upper thresholds led to reduced efficiency for detection of higher energy neutrons. Before the new campaigns, (ii), we realized that an important contribution of TOFOR to the JET physics program was in the region of high neutron energies, and it was decided to scrap the high thresholds.

An investigation of the randoms suppression achieved with the upper thresholds was also done. Discriminating against 2.5 MeV neutrons that deposit 2.3 MeV proton recoil energy in S1 (as was attempted during the first campaigns) is equivalent to discriminating against neutrons that scatter through an angle larger than 73.6° . The probability for neutrons to scatter with an angle larger than 73.6° compared to the total scattering probability was used as a measure of how effective the high thresholds were in discriminating against random background. Using differential cross sections from

[75], it was found that the upper thresholds suppressed less than 1/10 of the 2.5 MeV randoms.

From the comparison between Figure 26a and b, it is clear that the effective thresholds have drifted during periods (ii) and (iii). The mV levels set in the CFDs did not change during this time. It is determined that the reason for the effective threshold drift is a drift (drop) in PM tube gain. In Figure 27, the TOFOR coincidence counts are shown divided by the neutron yield as measured by the fission chambers for pulses with $P_{NB} > 10$ MW and no RF heating. As can be seen, the TOFOR efficiency decreased during the campaign from 71000 to 78200. An attempt was made to compensate for this efficiency drop by increasing the high voltage applied to the S1 PM tubes before the start of the next campaign (>78200). This can be seen to have the desired effect (Figure 27).

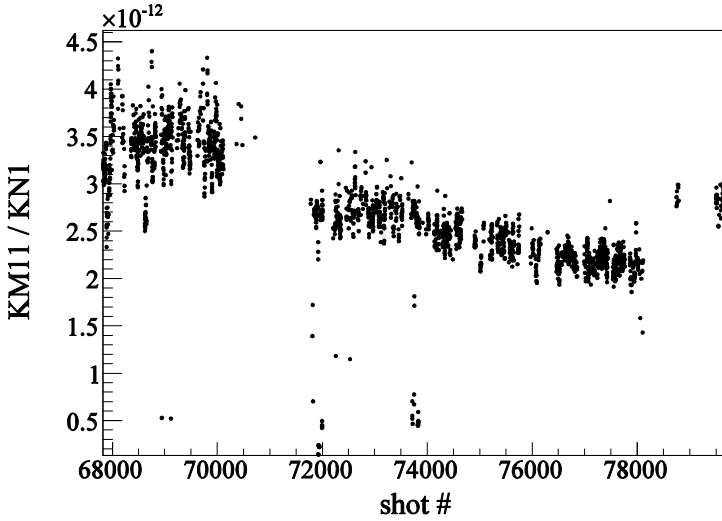


Figure 27. TOFOR (KM11) coincidences divided by total neutron yield as measured by the fission chambers (KNI) as a function of shot number.

The efficiency drop seen in Figure 27 can also be understood by comparing S1 ADC data from similar JET pulses from the high-efficiency period (68000-71000) and the beginning and end of the 71000-78200 campaigns. Such a comparison (for S1-2) can be seen in Figure 28. It is obvious that the amplification in the PM tube has decreased during this time period.

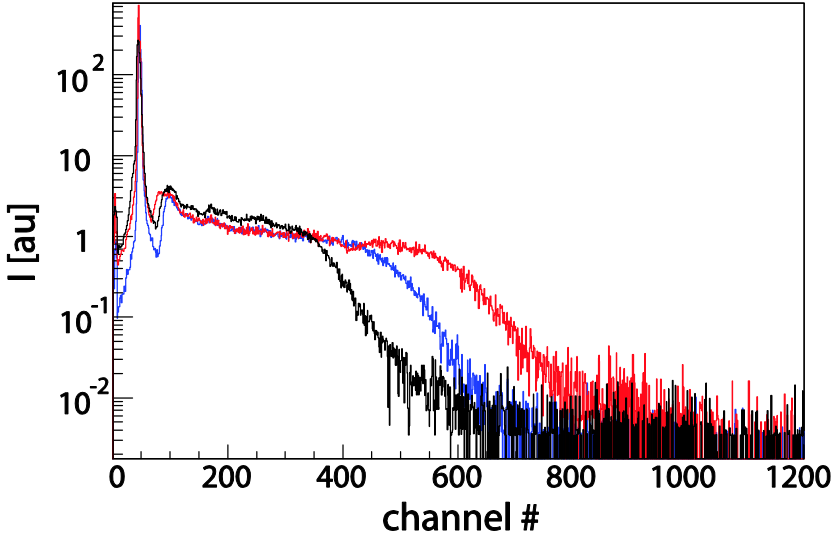


Figure 28. Comparison of ADC spectra for S1-1 collected for pulses 68448 (red), 72618 (blue) and 77943 (black). The spectra are all from NBI heated shots with more than 10 MW of heating power. They have been normalized to their average value in bins 200-400.

A function to monitor the PM tubes for gain drifts is included in the TOFOR Control & Monitoring (C&M) system. As described in detail in paper II, each TOFOR detector is equipped with a light fiber so that the individual detectors can be fed light pulses from a common LED source, distributed in parallel to all detectors. In addition, a reference detector outside of the TOFOR setup is equipped with both such a light fiber and a ^{241}Am source, used as an absolute standard.

The PM tubes are monitored for gain through analysis of the LED peak from the calibration spectra collected in connection with each JET pulse. The reference detector is used to establish if any LED intensity drift has occurred, so that the PM tube gain drift can be isolated. An example of a ^{241}Am spectrum with an asymmetric Gaussian fit is shown in Figure 29. Also the pedestal is fitted and its position taken as the origin of the amplitude scale. Figure 30 shows an LED spectrum (from S1-2) with Gaussian fits to both the pedestal (which is subtracted) and the LED peak.

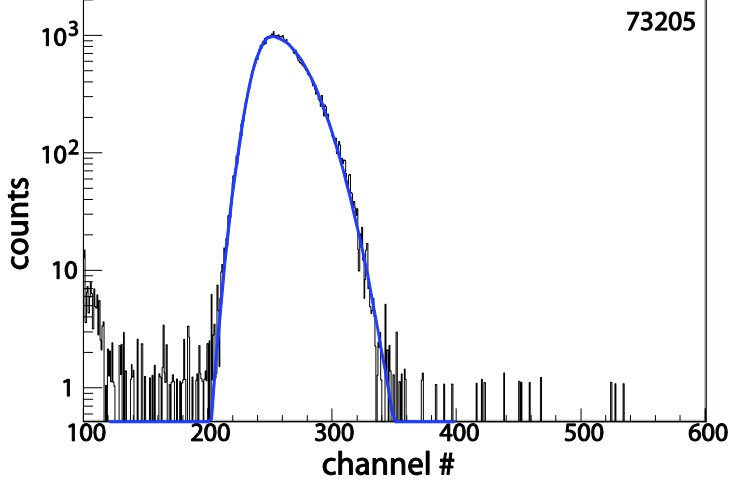


Figure 29. ²⁴¹Am reference ADC spectrum collected during JET pulse 73205, with an asymmetric Gaussian fit to the data. (Color online)

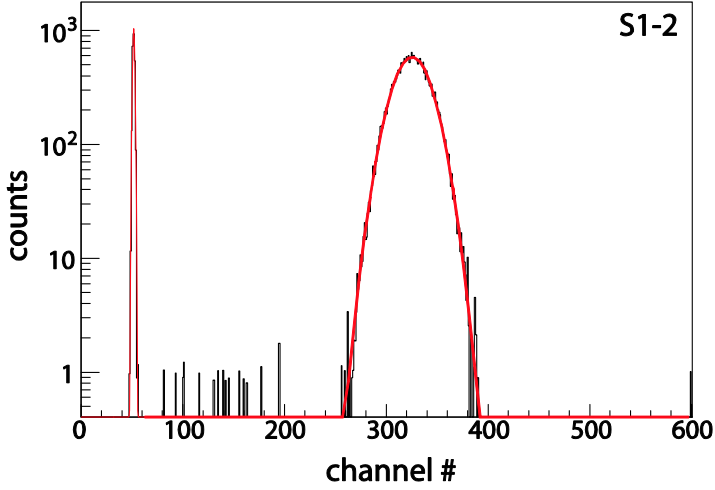


Figure 30. LED calibration ADC spectrum for S1-2, with Gaussian fits to pedestal and LED peak indicated. (Color online)

The correction process is outlined in ref [76]. The final result will be an ADC spectrum peak position, corrected for the pedestal position, for each detector and discharge (D_{corr}^S) corrected for the LED drift according to

$$D_{corr}^S = D^S \frac{A_{LED}^R}{A_{LED}^S} \frac{A_{Am}^S}{A_{Am}^R} \quad (19)$$

where the superscript S represents the discharge selected for study and R the reference discharge. D^S is the measured LED peak position minus pedestal for the detector studied. A is the peak position minus pedestal in the absolute reference detector for the ^{241}Am and LED peaks, respectively.

An example of a PM tube gain drift plot, for S1-1, is shown in Figure 31. The reference pulse is 73650 (one of the first pulses after automatic collection of calibration spectra was introduced), and the results are also normalized to D_{corr}^S for this discharge.

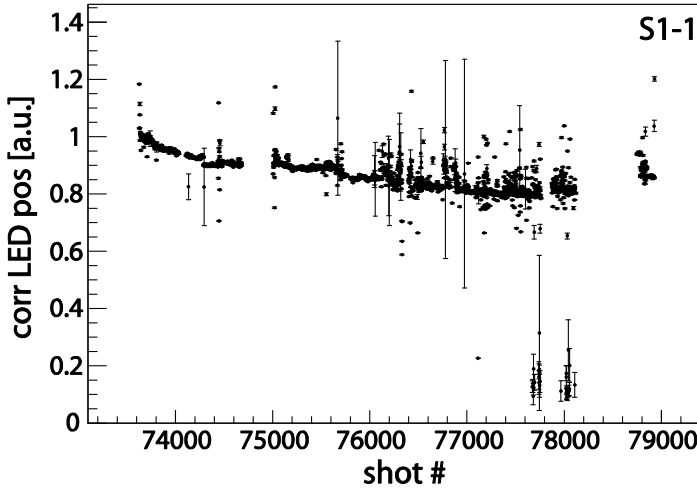


Figure 31. Example of a PM tube gain drift plot for detector S1-1, where the corrected LED peak position is determined as described in the text and normalized to the value for pulse 73650.

The error bars represent the total error with contributions from all components, where the individual peak and pedestal position errors are the errors in the mean value of the fits to the peaks:

$$\begin{aligned} \epsilon_{D^S,corr} = & \left(\left(\frac{A_{LED}^R A_{Am}^S}{A_{LED}^S A_{Am}^R} \right)^2 \epsilon_{D^S}^2 + \left(\frac{D^S A_{Am}^S}{A_{LED}^S A_{Am}^R} \right)^2 \epsilon_{A_{LED}^R}^2 + \left(\frac{D^S A_{LED}^R}{A_{LED}^S A_{Am}^R} \right)^2 \epsilon_{A_{Am}^S}^2 + \right. \\ & \left. + \left(\frac{D^S A_{LED}^R A_{Am}^S}{(A_{LED}^S)^2 A_{Am}^R} \right)^2 \epsilon_{A_{LED}^S}^2 + \left(\frac{D^S A_{LED}^R A_{Am}^S}{A_{LED}^S (A_{Am}^R)^2} \right)^2 \epsilon_{A_{Am}^R}^2 \right)^{\frac{1}{2}} \end{aligned} \quad (20)$$

4.2.2.2 Time alignment

Before initial operation of TOFOR in 2005-2006, the individual scintillators were time aligned relative to each other using LED pulses, an analogue time-to-digital (TDC) module with 50 ps resolution to measure the alignment and short LEMO cables to adjust it. It was believed that an alignment for all detectors within 0.1 ns was achieved. The intensity of the LED was varied during the measurements so that the peak would fall at about the same ADC channel for all detectors.

In January 2007, an attempt was made to redo the physical time alignment before the start of the new campaigns (JET # >71000). However, we found:

- That the time alignment had changed dramatically from the previous alignment.
- That measurements with the time boards used in the actual data acquisition chain changed the results as measured with the 50 ps TDC.
- That the time alignment between the different detectors was different depending on if it was determined with LED pulses or cosmic muons (correcting for the finite travel time between the different S1 layers in the latter case).

The time boards were seen to affect the time alignment at least partly due to different lengths of their connection cables. It was determined that if a hardware time alignment was to be done, it had to be done using the boards.

The observations indicate that the detector time alignment is pulse height dependent. In the new measurements using the 50 ps TDC, the LED intensity was not varied to match the pulse height between the detectors. This means the effective pulse heights changed between the old and new measurements. The cosmic muon pulses were also of different pulse height (and shape) than the old and new LED pulses.

Measurements done recording pulses with an oscilloscope indicate that the CFD modules introduce a pulse-height dependent time walk in the measurements. Signal pulses, output from a linear fan-in-fan-out (FIFO) module, and CFD pulses were recorded in the measurements. The timing of the

hardware CFD, as determined from the oscilloscope waveforms, was compared with applying a software CFD algorithm to the FIFO signal pulses (Figure 32). Note that the measurements provide no absolute measurement of the time walk; this would require a fixed reference time, such as a synch signal. With the current technique, it is unclear if the software or hardware CFD timing is a better estimate of the “true” pulse time. What is clear from Figure 32, however, is (i) that the time resolution is worse for low pulse heights, likely due to photon statistics and (ii) that there seems to be a time walk trend from low to high pulse heights. Assuming this time walk is different for different detectors, this peculiarity of the TOFOR CFDs could explain why the time alignment would be pulse height dependent.

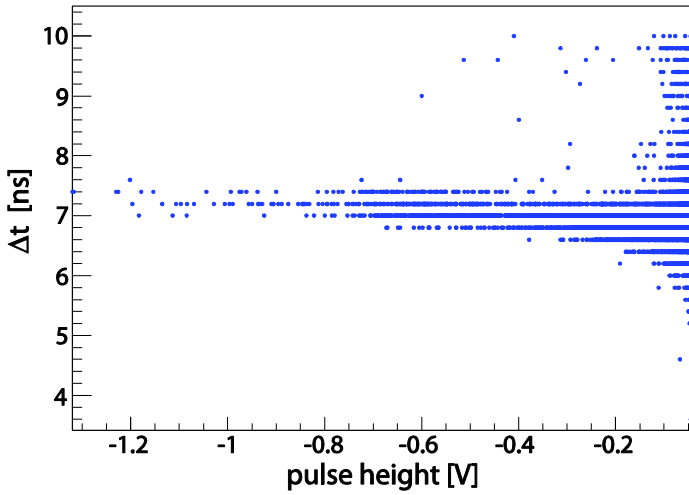


Figure 32. Time walk (Δt = software CFD time- hardware CFD time) as a function of pulse height, measured using an oscilloscope for S1-4. The discrete bands in the figure are due to a 0.2 ns bin width in the analysis. Note that the timing resolution is worse for low pulse heights (larger spread in Δt), and that a slight drift in the measured times can be observed towards larger pulse heights (increasing Δt).

A method has been developed where data from JET pulses with ohmic heating only is summed to achieve high enough statistics to determine the deviation of the S1-S2 coincidence peak times from the expected value for different detector combinations. With this method, relevant neutron pulse heights and shapes are used to determine the detector time alignment; hence, the timing issues described in this section can be avoided. Examples of results from the method are shown in Figure 33, with peak times as a function of pulse number for t_{TOF} spectra constructed for coincidences between individual S1s and all S2s, and Figure 34, with peak times for coincidence spectra between individual S2s and all S1s.

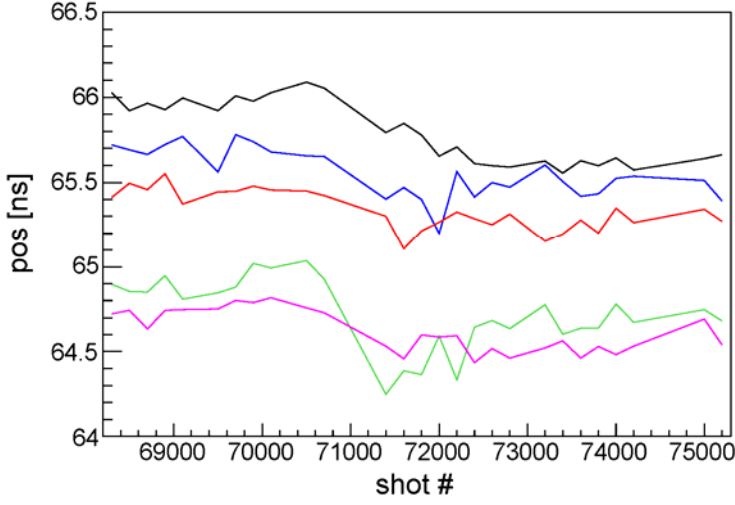


Figure 33. Time alignment for individual S1 detectors (S1-1 black, S1-2 blue, S1-3 red, S1-4 green and S1-5 magenta) based on t_{TOF} spectra constructed from coincidences between the individual S1 and all S2s.

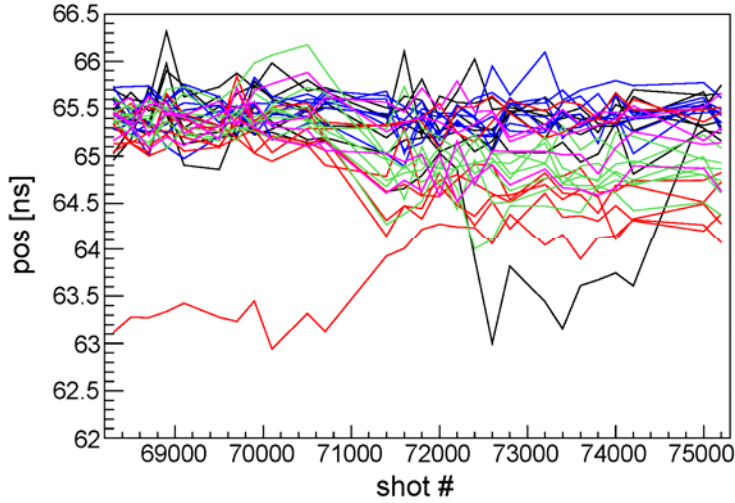


Figure 34. Time alignment of individual S2 detectors, based on t_{TOF} spectra constructed from coincidences between the individual S2 and all S1s. The colors follow the color for the S1 detector channel located on the same time board (cf Figure 33).

It can be seen that the alignment of the different S1 detectors relative to each other drifts over time, while the total spread is rather constant (Figure 33). The five S1 detectors are placed in a stack with S1-1 at the bottom and S1-5

at the top. This means that S1-1 (black curve) is expected to have the longest flight times to the S2 detectors and S1-5 (magenta) the shortest, which is indeed seen for early pulses in Figure 33.

From Figure 34, we conclude that the timing of the S2s has drifted apart since the original physical time alignment performed around pulse 68000. Two traces stand out in this figure: the red curve that starts 2 ns below the group represents detector channel S2-19, the timing of which improved around pulse 72000, and the black curve that temporarily leaves the group represents S2-1. The S2-1 deviation has a simple explanation: the electronics FIFO channel used for this detector broke and had to be replaced by a different one (from pulse 72366). This introduced a time shift. The alignment of the detector was restored by adding a 2 ns LEMO cable (from pulse 74480).

The results from the analysis of ohmic data for the S1s as illustrated in Figure 33 is used to create a correction matrix for the shot numbers in a period of stable alignment. This matrix is then applied to time align measured data from more complex JET pulses. Currently, no alignment is done to compensate for S2 timing drifts; this of course adds a time broadening to the measured t_{TOF} data.

4.2.2.3 Electronics broadening

The remaining broadening in the time-of-flight data relative to the response function with carefully determined thresholds, that is not accounted for by the time alignment, is attributed to a broadening in the electronics. Contributions to this broadening could be e.g. time jitter in the PM tubes, the pulse height-dependent timing resolution issues illustrated in Figure 32 and the time spread between the S2 detectors seen in Figure 34.

The total impact of this “electronics broadening” on the response of TOFOR is not straight-forward to quantify. Currently, a method is used where the response function is folded with a Gaussian of width Δt at full width half maximum (FWHM) to account for this effect. The size of Δt is found from fitting the response function to JET data from ohmic pulses, the width of which should follow equation (9). An example of such a fit is shown in Figure 35.

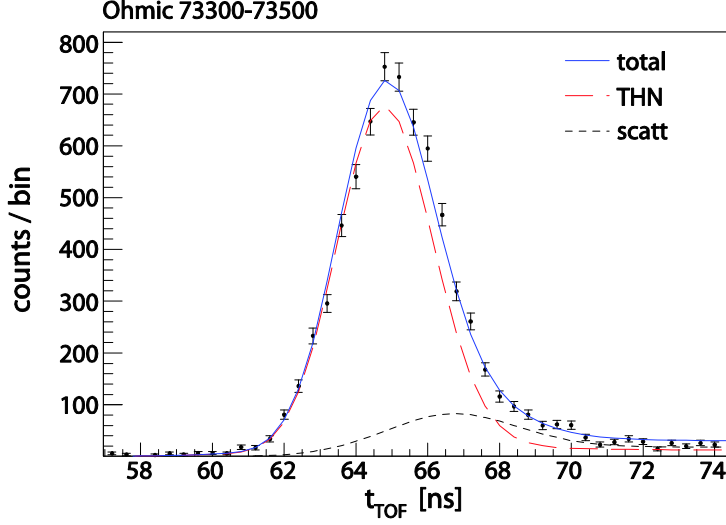


Figure 35. Fit to ohmic data from JET pulses 73300-73500, using the Cash statistics method described in section 3.4.1 above with two components: a thermal component according to equation (9) (long-dashed red) and a component to account for scattered neutrons as described in section 3.3 (short-dashed black). The total fit to the data is indicated as a solid blue curve. (Color online)

This method requires that the temperature of the observed plasmas is known. Ion temperatures T_i for ohmic pulses at JET usually fall in the range 2-3 keV. It was found that results consistent with charge exchange spectroscopy measurements were reached if the electronics broadening was determined assuming a weighted average of $T_i=2.7$ keV for the ohmic plasma temperature.

The shape of the scattered component is also of importance. The procedure has had to be step-wise revised as our understanding of the scattered neutron flux has improved.

Naturally, this is not a satisfactory method for calibrating the TOFOR T_i measurements. It would be imperative to further increase the understanding of the electronics broadening to be able to account for it in a more exact way. This could turn out to be easier if hybrid boards were introduced, eliminating the need for CFDs in the electronics chain, and with a different S1 detector setup, producing larger pulse heights and thus less sensitive to photon statistics-dependent pulse height resolution issues.

4.3 Optimization of data analysis

As has been demonstrated, the measured representation of the incident neutron spectrum is, in addition to the instrument geometry, also dependent on discriminator thresholds, detector time alignment and an additional electron-

ics broadening. In summary, these effects are taken into account in the analysis by:

- Time aligning the S1 detector channels by shifting the individual S1s to the same t_{TOF} at 2.5 MeV.
- Adding a $\Delta t=1.5$ ns empirical broadening due to electronics to get reasonable T_i for ohmic plasmas.
- Using a response function with appropriate E_p values for the thresholds.

The tool used for visualization and Neutron Emission Spectrometry (NES) analysis of TOFOR data has been adapted to automatically select the response function with the thresholds that best match the settings and time align the data using the correct alignment matrix for the pulse studied. The match between the data and the response function could be further optimized by e.g. more regular ^{22}Na threshold measurements and correction also for S2 time alignment drifts.

The energy-dependent resolution $\Delta E_n/E_n$ (FWHM) of TOFOR has been determined from fitting a Gaussian to the final broadened and aligned response function t_{TOF} spectrum for each neutron energy (Figure 36). As can be seen, the resolution is best for neutrons of about 2 MeV at 7.7%; at 14 MeV, the resolution is about 15.8%.

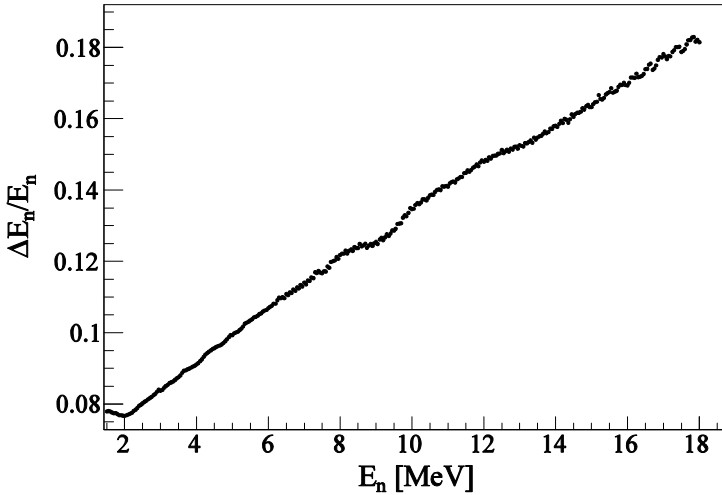


Figure 36. Resolution (FWHM) of TOFOR as a function of incident neutron energy, determined from fitting a Gaussian to the peak in the t_{TOF} spectrum of the final response function.

A resolution worse than the thermal broadening of the plasma studied does not mean that the parameters cannot be measured; however, accurate knowledge of the response function and good statistics in the measurement are required.

4.4 14 MeV TOFOR and hybrid boards

Before installation of TOFOR at JET, it was thought that the discriminator thresholds set for each TOFOR detector channel could be adjusted during campaigns to optimize the instrument for the plasma scenario under observation. This, however, turned out to be impossible in practice, given (i) that the thresholds are tweaked by physically manipulating a screw for each of the 37 detector channels and (ii) that it was not possible to connect such temporarily tweaked thresholds in mV level to their E_p equivalent for input to the response function. After the use of high thresholds to discriminate against high energy events was discontinued (see section 4.2.2.1 above), it was however decided that these high thresholds could now be used for easy changing of TOFOR settings for a different operation regime. The high thresholds were adjusted to discriminate against almost all 2.5 MeV neutrons in S1, including the ones incompatible with direct coincidences S1-S2 (compare Table 2) and to exclude the main part of the background contribution in S2. ADC spectra from operation above the low thresholds (JET pulse 76192, red curves) and the new high thresholds (JET pulse 76193, black curves) are shown in Figure 37 for S1-3 and S2-27, respectively. The plasma parameters are very similar for the two pulses; the ADC spectra have not been normalized.

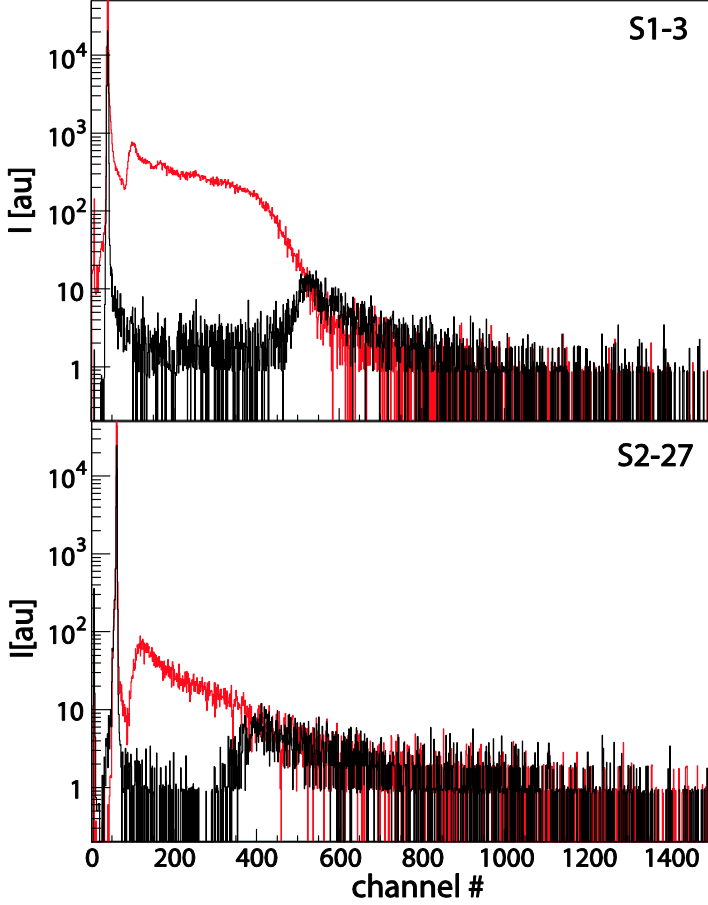


Figure 37. ADC spectra recorded for S1-3 and S2-27, respectively, for JET pulses 76192 (red, high signal in channel region 100-400) and 76193 (black) with very similar plasma parameters. The difference between the red and black curves is operation with TOFOR above the low or high thresholds. (Color online)

In the S1 case, the spectrum which for pulse 76192 included protons up to 2.5 MeV energies according to equation (9) has been cut by the high threshold to only include the very highest energy protons for pulse 76193 (top panel). The target threshold settings were $E_p=2400$ keV for S1 and $E_p=500$ keV for S2. In this way, TOFOR was optimized for detection of the weak contribution of 14 MeV neutrons from DT reactions, without interference of randoms from 2.5 MeV neutrons. An example of a t_{TOF} spectrum collected with TOFOR set to record data above the high thresholds only is given in Figure 38. Note that the 14 MeV DT peak at 27 ns is clearly visible, while the normal 2.5 MeV DD peak at 65 ns is absent.

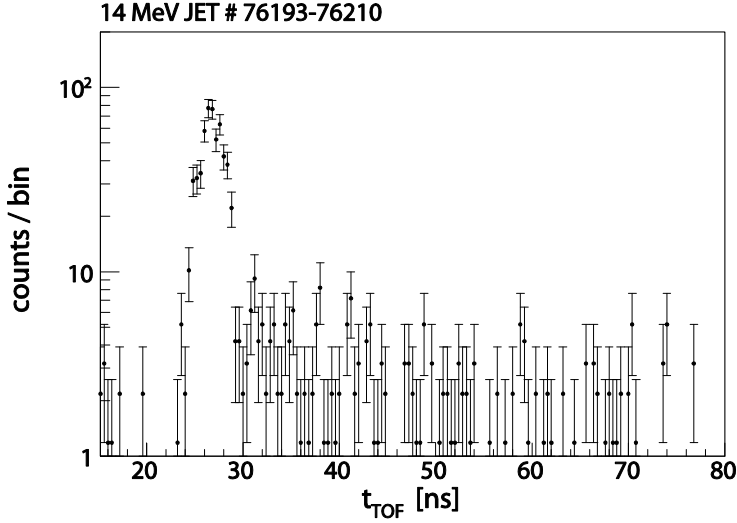


Figure 38. Summed time-of-flight spectrum from JET pulses 76193-76210, with TOFOR set to record data above the high threshold only. The DT neutron peak at 27 ns dominates the spectrum; the absence of a peak at 65 ns where DD neutrons of 2.5 MeV would fall should also be noted.

With the current electronics setup, only one time board channel is available for each detector channel and though signals above both the high and low thresholds are created for each JET pulse, only one can be recorded. This would not be the case if TOFOR was to be upgraded with hybrid boards. Pulse shapes for each event would then be recorded, and time-of-flight spectra with different threshold settings could be constructed for the same pulse. This could not only be used to separately study 2.5 MeV and 14 MeV neutrons; it could also be used to decrease the random contribution to highlight weaker features of the spectrum at energies between 2.5 and 14 MeV.

Of course, the problem of knowing the threshold levels in proton equivalent would remain also for the hybrid boards. In theory, however, if a thorough characterization of the pulse height-to-energy scale was done before the start of campaigns, the data could be corrected for PM tube gain drifts on a shot-to-shot basis using the method described in section 4.2.2.1, since the pulse height and event time information would now be correlated. As previously mentioned, the time walk problems introduced by the CFD modules in the current electronics setup might also be possible to eliminate using hybrid boards.

A main advantage expected from a hybrid board introduction is the possibility of event selection based on kinematics. Knowing deposited energies in S1 and S2, it should be possible to exclude events with flight times not compatible with neutrons on a direct track between the two detector sets. This should lead to elimination of multi-scatter and a large fraction of random

events. However, it is not straightforward to determine how this would work with a spectrum of incoming neutron energies giving different direct-track flight times and energies, and assuming that there will still be some pulse height resolution issues. A simulation project is underway to study these issues in detail.

4.5 Improving campaign preparation and monitoring

Based on the detailed characterization work described here, it is appropriate to end this chapter with some suggestions for future improvements in the campaign preparation and monitoring. It is obvious that the main stability issue with TOFOR is drifts in threshold levels accompanied by a drop in efficiency (Figure 27) due mainly to drops in PM tube gain. The threshold drift, if it is not physically corrected or taken into account in the response function, will have a detrimental impact on data analysis (Figure 26). With the current setup, it is difficult to correct the threshold levels based only on measurements of PM tube gain drifts, since these drifts cannot be correlated to deposited energies. One way to get around this problem could be weekly ^{22}Na runs throughout the campaigns. It is not easy to get access to the restricted area of the roof laboratory at JET where TOFOR is located during campaigns. However, as described in paper II, a weak ^{22}Na source is placed inside the S1 detector box. This source is too weak to be useful for S2 threshold measurements; however, the problem has been identified to affect S1 much more than S2. 48 hour ADC spectra collected over each weekend during campaigns could be used to get a new response function each week to match the data collected. This way, also smaller physical corrections could be made possible.

This monitoring should be combined with thorough threshold calibrations for all detectors before a campaign, where the thresholds for each S1 or S2 detector channel are set to the same value. It could also be good to check the PM tube high voltage settings; if the PM tube gain is high at the start, there is more room for adjusting the thresholds as the gain drops over the campaigns to keep the original efficiency. Also new ADC DNL spectra should be collected before the start of each campaign.

5 Data analysis and results

The purpose of this chapter is to demonstrate how the methods described in section 3.4 are used and what type of physics results can be obtained with TOFOR. Detailed results from analysis of TOFOR data are presented in papers III, IV, V and VI of this thesis.

In order to perform accurate analysis, a detailed understanding of the instrument response (as discussed in chapter 4) and of the contribution of scattered neutrons (paper III) to the spectrum is essential. Section 5.1 below includes comments on backscatter; the reader is referred to paper III for further details.

As mentioned in chapter 4, the response function broadening is crucial in using TOFOR to determine bulk ion temperatures. Temperature measurements, classically viewed as the specialty of neutron spectrometry diagnostics, are not the strong point of TOFOR due to the current insufficient understanding of this broadening. Also the interference in the region of the thermonuclear peak of neutrons from beam-thermal and beam-beam reactions (broadened in the region $E_n=2-3$ MeV) complicates the temperature deduction from TOFOR data from many JET discharges as will be exemplified in section 5.1. Of course, this would be different in a burning plasma reactor where the bulk of the emitted neutrons are expected to originate from thermonuclear reactions.

Another classical strong point of neutron spectrometry is the ability to determine the ratio $Q_{\text{thermal}}/Q_{\text{non-thermal}}$. This relates to the ability of the instrument to separate contributions to the neutron spectrum from reactions between different subpopulations. For TOFOR, this is done using component analysis as discussed in section 5.1.

During the recent campaigns, a strong contribution of TOFOR to the JET physics program has been in the area of fast ions, mainly from RF heating. In its simplest form, the contribution of TOFOR to an experiment can be to verify the presence of fast deuterium through study of collected t_{TOF} spectra (section 5.2). Application of the deuterium distribution unfolding method (section 3.4.2) can yield an experimental estimate of the fast deuterium distribution (section 5.3). TOFOR has also been employed to establish a contribution to the neutron spectrum from reactions between fast ions and beryllium impurity in the plasma, as described in paper VI. Another example of this type of analysis is discussed in section 5.4. Finally, section 5.5 is dedicated to discussion of 14 MeV neutron measurements with TOFOR. In con-

nection with this analysis, we also briefly discuss the possibility of using neutron spectrometry for n_t/n_d fuel ion ratio measurements.

5.1 Component analysis and scattered neutrons

The component fitting method described in section 3.4.1 was employed in the analysis described in papers II, III and VI. In Figure 39, component fitting is illustrated through applying the method to JET pulse 73311. The time interval studied is $t=9.2\text{--}10.3$ s, with constant applied NB power $P_{\text{NB}}=18$ MW and electron density $n_e \approx 2.6 \times 10^{19} \text{ m}^{-3}$. A random background of 24.53 counts per channel has been subtracted in the figures; however, this random level is used as a fixed component in the Cash minimization throughout the analysis.

Figure 39a shows the result of fitting just a thermonuclear (TH) component, modeled as described in section 3.4.1, to data in the region $50 < t_{\text{TOF}} < 85$ ns. This fit gives $C_{\text{red}}=5.03$, and is not realistic since also neutrons from beam-thermal reactions are expected due to the applied NB heating. In panel (b), the fit is instead performed with a beam-thermal (NB) component only, modeled as described in section 3.4.1 as a box in ion energy space between E_{min} and E_{max} . C_{red} from this fit is 7.46. The component follows the shape of the peak region of the spectrum rather better than the TH component, but also thermonuclear emission is expected in this case. In panel (c), both TH and NB components are used, and $C_{\text{red}}=4.16$. However, the temperature T_i estimated from the fit of the TH component is unreasonably high at 21 keV. In panel (d), T_i is fixed to the value as measured by the charge exchange diagnostic at JET, i.e., $T_i=8.8$ keV, and $C_{\text{red}}=5.03$. The fit does not follow the data on the low- t_{TOF} side of the peak in panel (d). The explanation is that because of the low density in this pulse, also reactions between particles in the beam population (beam-beam) will play a role. A fixed-shape component describing the beam-beam (BB) emission, with intensity as the free parameter, is therefore added in the analysis. The component is obtained from TRANSP [8] modeling of the pulse. The result of fitting TH (with fixed T_i), NB and BB components (with $C_{\text{red}}=4.31$) is shown in panel (e). The NB component maximum energy from the fit is $E_{\text{max}}=124$ keV, which is realistic given that the beams are injected with $E_{\text{inj}}=80\text{--}130$ keV. The fit in the peak region is now starting to look rather good, but it is clear that something is missing on the high- t_{TOF} (low- E_n) side of the peak. This is the scattered neutron contribution as discussed in section 3.3 and paper III.

The scatter component for use in the fit is generated through folding the approximate direct spectrum (Figure 39e) with a scatter matrix. The scatter matrix consists of scatter spectra such as the one illustrated in Figure 10 (with a bin width of 50 keV) for quasi-monoenergetic (± 25 keV) emitted

neutron energies in steps of 50 keV, in the interval 1-18 MeV (see paper III for details). After a first fit with the scatter component, the component can again be removed from the fit and a new scatter component generated based on the modified estimate of the direct spectrum, etc. The final component analysis fit to the data with all components included ($C_{\text{red}}=0.66$) is shown in Figure 39f. This approach can be compared with the attempt to analyze this same pulse through response function inversion in Figure 11.

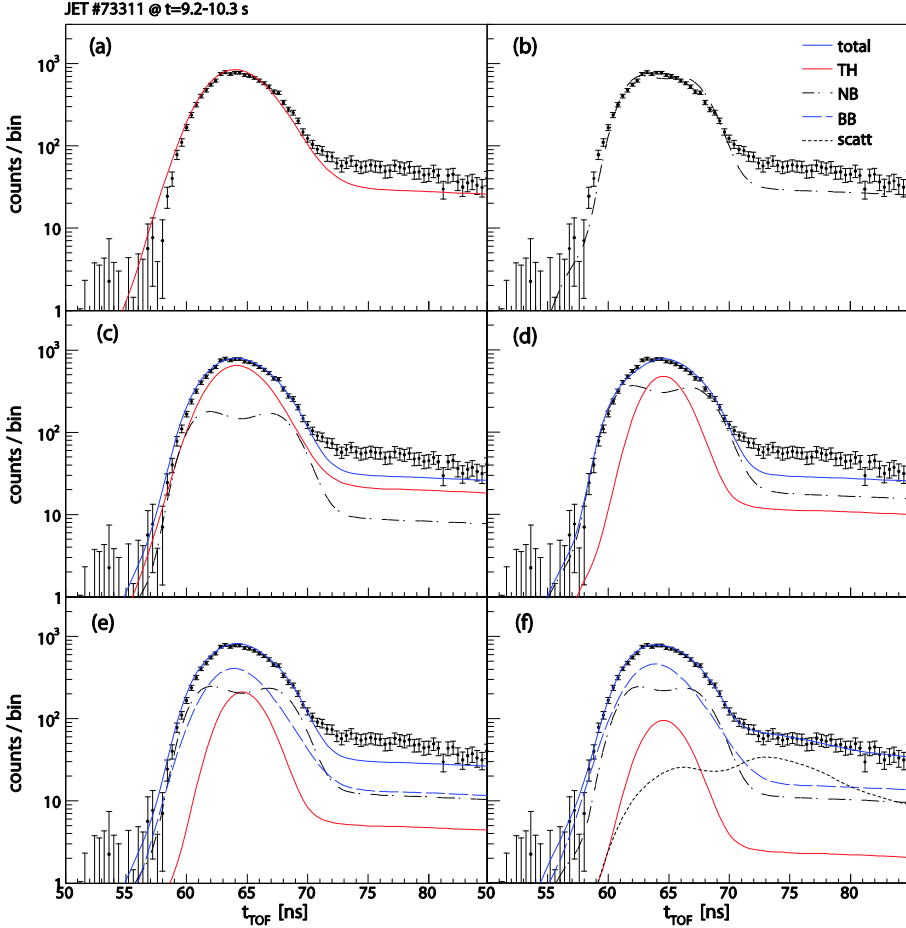


Figure 39. Step-by-step component analysis applied to TOFOR data from JET pulse 73311, during the time $t=9.2-10.3$ s with $P_{\text{NB}}=18$ MW. The panels show the result from component fitting using Cash statistics with (a) a thermonuclear (TH) component only, (b) a beam-thermal (NB) component only, (c) TH and NB components, (d) TH and NB with TH temperature locked to value from charge exchange measurements, (e) TH, NB and beam-beam (BB) components and (f) complete analysis using TH (with T_i locked), NB, BB and scatter components. (Color online)

The total number of neutron coincidences in TOFOR in the data studied in Figure 39 is about 17400. The total number of neutrons emitted during the same period is 6.7×10^{15} as determined by the JET fission chambers. The analysis yields an estimate of the number of neutrons incident on S1 (N_{S1}) from reactions between different subpopulations, taking into account the TOFOR efficiency as determined by the response function. In this case, $N_{S1}^{TH} = 1.4 \times 10^5$, $N_{S1}^{NB} = 6.6 \times 10^5$, $N_{S1}^{BB} = 8.0 \times 10^5$ and $N_{S1}^{scatter} = 2.7 \times 10^5$. This means the ratio scatter/direct (compare paper III) is 0.17.

The simplified beam-thermal box model, implemented as the default NB fit component in NES, is used here. More sophisticated analysis of the beam-thermal neutron emission is possible, but has not been the focus of this thesis. For pulses heated with single PINI NBI, the E_{max} used in the analysis can be found to closely match the beam injection energy E_{inj} [77]. A model has been constructed where a superposition of boxes representing each PINI used in the heating, with appropriate $E_{max} = E_{inj}$, is used as the NB component instead of the simple box [78]. Also, beam-thermal components from TRANSP modeling can be used in the NES analysis [77,79].

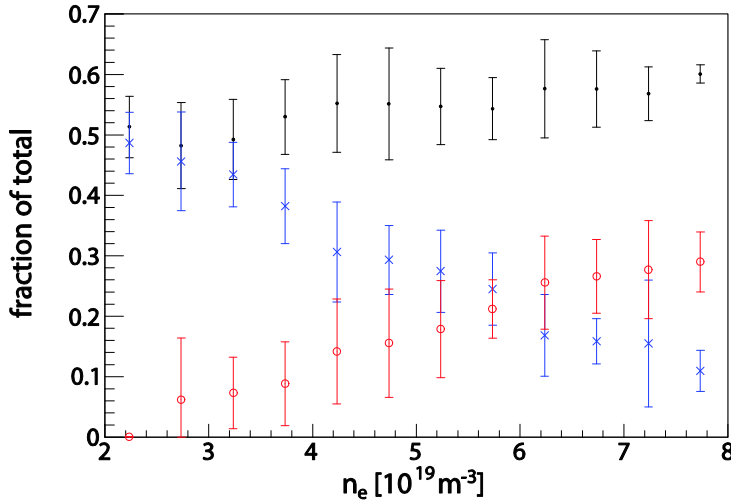


Figure 40. Fractional contribution to the total spectrum of neutrons incident on TOFOR from thermal (red hollow circles), beam-thermal (black points) and beam-beam (blue crosses) components as a function of n_e , for pulses in the interval 71000-74000 with $P_{NB} > 10$ MW and $P_{RF} = 0$. The points represent averages over the interval $n_e \pm 0.25 \times 10^{19} m^{-3}$. (Color online)

As shown in the analysis of 73311 above, the component fitting can be used to separate the contribution to the neutron emission from reactions between ions from different subpopulations. Knowing this fractional contribution, the Q value (see section 1.1) from the different contributions can be calculated

and $Q_{\text{thermal}}/Q_{\text{non-thermal}}$ determined. Figure 40 shows the fractional contribution to the total neutron spectrum incident on TOFOR from thermonuclear (TH), beam-thermal (NB) and beam-beam (BB) reactions as a function of electron density n_e , for JET pulses in the interval 71000-74000 with $P_{\text{NB}} > 10$ MW and no RF heating applied. The points in Figure 40 represent averages over $0.5 \times 10^{19} \text{ m}^{-3}$ wide bins. As can be seen, the NB contribution stays rather constant independent on bulk electron density, while the BB contribution is higher at lower density (as expected) and the TH at higher density.

5.2 Deuterium tails

Folding neutron spectra from mono-energetic deuterium distributions such as the ones in Figure 8 with the TOFOR response function, the minimum deuterium energies required to reach below set flight times can be deduced. In Figure 41, such t_{TOF} spectra obtained from folding theoretical neutron energy spectra with the response function are shown, corresponding to the thermonuclear emission from a 3 keV bulk plasma and reactions between a 3 keV bulk plasma and mono-energetic 100 keV, 300 keV, 500 keV, 1 MeV, 2 MeV and 5 MeV deuterons, respectively.

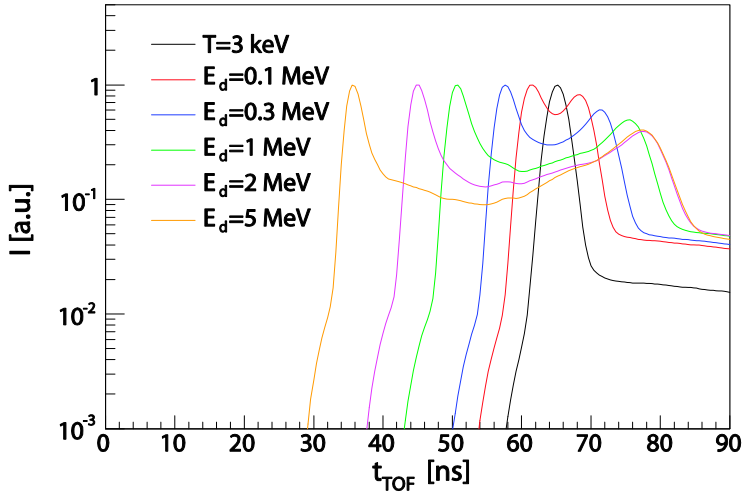


Figure 41. Modeled t_{TOF} spectra obtained from folding theoretical neutron spectra (as in Figure 8) with the TOFOR response function, for a 3 keV D bulk reacting with itself and mono-energetic deuterons of 0.1, 0.3, 1, 2 and 5 MeV energy in order of spectral broadening. (Color online)

It is clear from the figure that simple observations of the TOFOR spectra can be used to verify the presence of fast deuterium in the plasma. Events in the region $t_{\text{TOF}} < 55$ ns in the TOFOR spectra are (usually, compare section 5.4 and paper VI) a clear indication of the presence of deuterium ions of higher energy than the beam deuterium ions.

Here, we exemplify this type of TOFOR observations with analysis of data from two different sessions, on August 12th and September 29th, 2009, involving RF mode conversion. The same techniques can be applied to any plasma scenario involving RF heating on deuterium and can be very interesting for 2nd harmonic D heating (paper IV, where the results are compared with NPA data) and 3rd harmonic D heating (paper V, where the techniques are applied to study correlations with MHD activity).

In Figure 42, smoothed (adding 4 bins together, $\Delta t_{\text{TOF}} = 1.6$ ns) t_{TOF} spectra from pulses 78836, 78841 and 78842 from the August 12th session are shown, along with the spectrum from NB heated discharge 73311 for comparison.

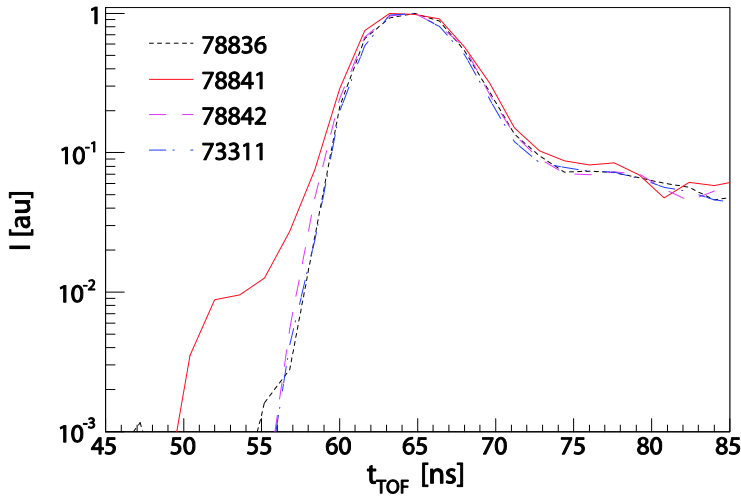


Figure 42. Smoothed t_{TOF} spectra as measured with TOFOR for JET pulses 78836 (dotted black), 78841 (solid red), 78842 (dashed magenta) and 73311 (dash-dotted blue). (Color online)

All pulses in Figure 42 are D plasmas heated with D neutral beams. The August 12th plasmas were seeded with ^3He (same amount for the three pulses studied) and the RF power tuned to the fundamental frequency of this seed population with the resonance layer located near the plasma center (Table 4). In addition to the central ^3He resonance layer, an in-board fundamental D resonance is also present (Table 4). Time traces for the NB and RF heating

power and the total neutron rate as measured by the fission chambers for pulses 78836, 78841 and 78842 are shown in Figure 43.

Table 4. RF frequency ω_{RF} , toroidal magnetic field B_{T} , plasma current I_{p} , positions of RF resonance layers for fundamental heating of D (R_{RF}^{D}) and ^3He ($R_{\text{RF}}^{^3\text{He}}$) and ^3He concentrations ($n_{^3\text{He}}$) for pulses 78836, 78841 and 78842.

	78836	78841	78842
ω_{RF} [MHz]	37	33	33
B_{T} [T]	3.42	3.4	3.4
I_{p} [MA]	1.8	1.8	1.8
R_{RF}^{D} [m]	2.11	2.35	2.35
$R_{\text{RF}}^{^3\text{He}}$ [m]	2.81	3.13	3.13
$n_{^3\text{He}}$ [n_{e}^{-1}]	0.20	0.21	0.20

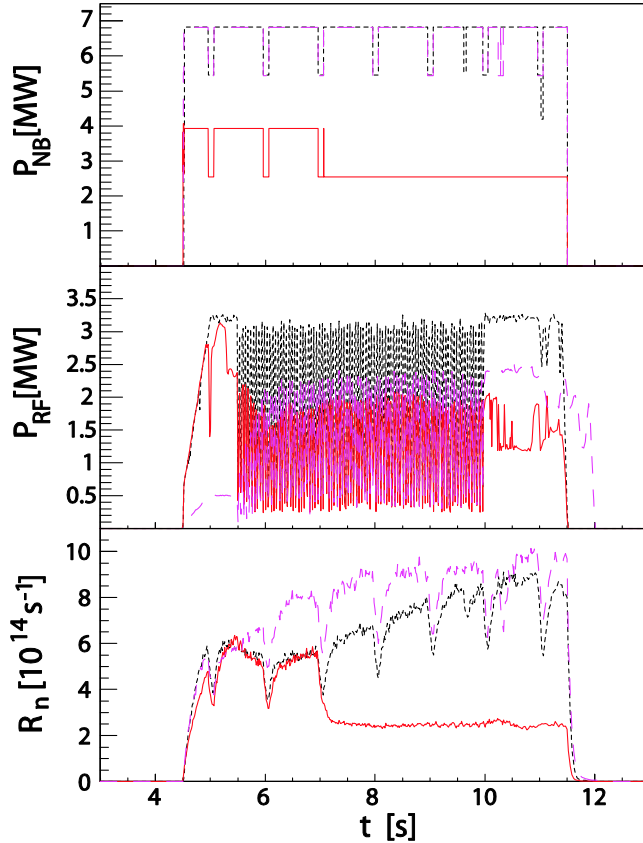


Figure 43. Time traces of plasma parameters for JET pulses 78836 (dotted black), 78841 (solid red) and 78842 (dashed magenta). The top panel shows the NB heating power, the middle the RF heating power and the bottom panel the total neutron rate as measured by the fission chambers for the three discharges.

The D resonance is not in the TOFOR line-of-sight for any of the three pulses 78836, 78841 and 78842. However, it is clear that a small tail of fast deuterium is seen for pulse 78841 (compare Figure 42 and Figure 41), though the tail is on a low level (10^{-2} of the main peak) indicating that the effect is weak in comparison with the beam-thermal reactions. The explanation for this tail could be that the resonance layer for D heating is Doppler shifted towards higher major radius R due to the energy of the beam ions. Such an effect was previously observed and discussed in [12], where the build-up of the tail was observed above a threshold ^3He concentration. With a certain amount of ^3He present in the plasma, mode conversion of the RF heating makes the D resonance layer accessible to the RF waves, that enter the plasma from the out-board side. Since the ^3He concentration is the same for the three pulses studied here, the presence or absence of a tail cannot be explained by this observed concentration threshold effect. The reason why no tail is seen for 78836 could be that the D resonance layer is located even further on the in-board side of the plasma in this case (see Table 4). For 78842, P_{RF} is substantially weaker than for 78841 (Figure 43); this could explain the fact that a tail is seen for 78841 and not for 78842. This simple discussion on cause-effect of the observed tail is in no way to be regarded as final; the observation of a tail has been reported to the coordinators of the experiment and the interpretation will be finalized in comparison with other diagnostic data collected during the session.

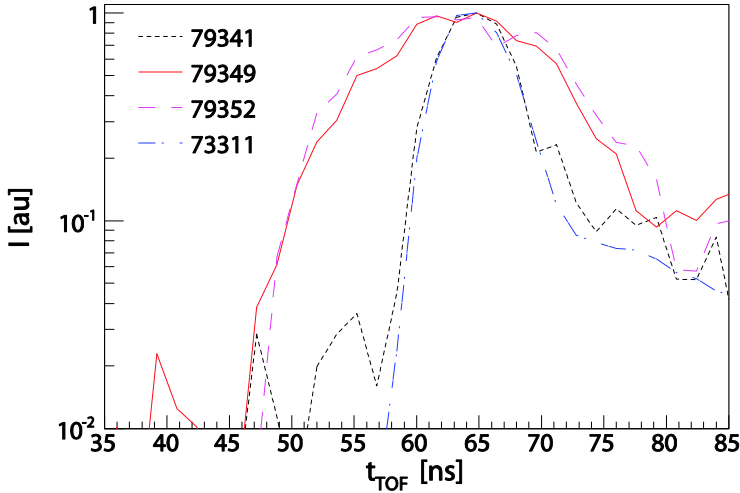


Figure 44. Smoothed t_{TOF} spectra for JET pulses 79341 (dotted black), 79349 (solid red), 79352 (dashed magenta) and 73311 (dash-dotted blue). (Color online)

The second example (Figure 44) comes from a similar session on September 29th, 2009, with the modification that the bulk plasma consists not of D but of H. D beams are however still used. Similar mode conversion as in the D(³He) case has previously been studied also for H(³He) plasmas [15]. It was observed that the threshold ³He concentration, $n_{3\text{He}}/n_e$, for mode conversion heating was lower in this case than for D(³He) plasmas, with mode conversion dominating from $n_{3\text{He}}/n_e \sim 2\%$. The t_{TOF} spectra in Figure 44 are again smoothed ($\Delta t_{\text{TOF}} = 1.6$ ns). Large tails are seen for pulses 79349 and 79352, but not for pulse 79341. The effect is strong relative to the bulk emission (same level as the main peak). This is easily explained as a consequence of the H background plasma; there is no bulk D for the beams to react with. Only beam-beam reactions will contribute to the neutron emission.

Parameters for the pulses studied are listed in Table 5, and time traces for P_{NB} , P_{RF} and the total neutron rate from the fission chambers shown in Figure 45. In this case, the RF and NB powers are similar in the three pulses; it seems like the absence of a tail for pulse 79341 could be related to the lower ³He concentration (1-4.5% compared to 10 and 2-15 for 79349 and 79352, respectively).

Table 5. RF frequency ω_{RF} , toroidal magnetic field B_T , plasma current I_P , positions of RF resonance layers for fundamental heating of D (R_{RF}^{D}) and ³He ($R_{\text{RF}}^{\text{3He}}$) and ³He/H concentrations ($n_{3\text{He}/\text{H}}$) for pulses 79341, 79349 and 79352.

	79341	79349	79352
ω_{RF} [MHz]	33	33	33
B_T [T]	3.41	3.41	3.41
I_P [MA]	1.8	1.8	1.8
R_{RF}^{D} [m]	2.35	2.35	2.35
$R_{\text{RF}}^{\text{3He}}$ [m]	3.13	3.13	3.13
$n_{3\text{He}/\text{H}}$ [$100 \times n_e^{-1}$]	1-4.5/88	10/80	2-15/88-70

An interesting observation is that the neutron rate (bottom panel in Figure 45) starts rising later for pulse 79352 (dashed magenta) than for pulse 79349 (solid red) with similar heating power. This could also be understood in terms of ³He concentrations; as can be seen in Table 5, the ³He concentration is stable at 10% for 79349, but rises from 2 to 15% for pulse 79352. It is easy to imagine that the threshold between minority and mode conversion heating for the ³He population is passed at the point when the neutron rate starts to rise.

For these pulses, the total neutron rate can be used to back up this kind of discussion because the neutron emission is dominated by reactions involving the fast D population (Figure 44). However, this is not always the case, e.g., not for the August 12th data (Figure 42).

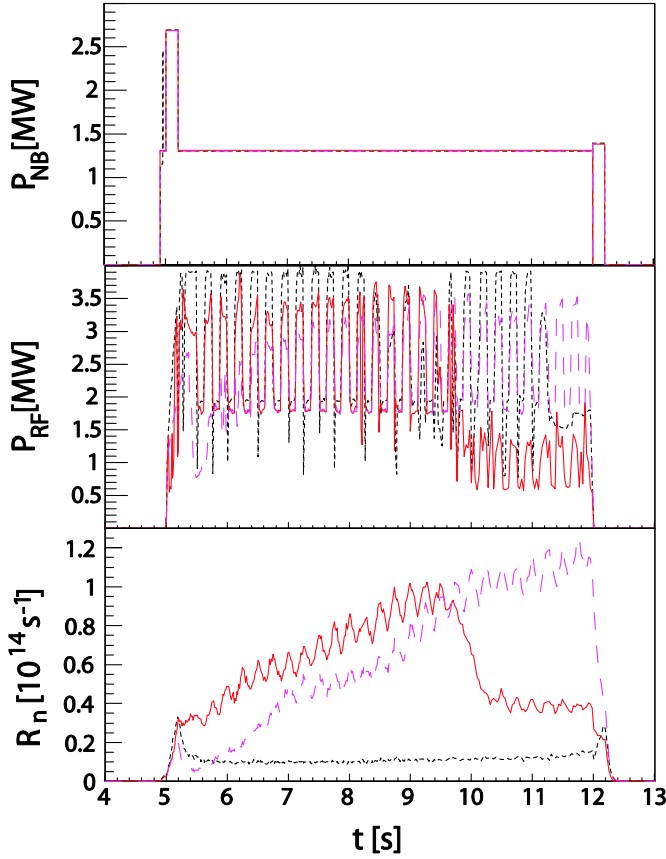


Figure 45. Time traces of plasma parameters for JET pulses 79341 (dotted black), 79349 (solid red) and 79352 (dashed magenta). The top panel shows the NB heating power, the middle the RF heating power and the bottom panel the total neutron rate as measured by the fission chambers for the three discharges.

It can be useful to construct a ‘probe’ of the time development of the fast neutrons to diagnose the evolution of the fast ion population. This can be done by integrating the counts in a set region of t_{TOF} in the TOFOR spectrum, as was done in papers IV and V. Here, we exemplify this by comparing bulk ($58 < t_{\text{TOF}} < 70$ ns) and fast ($t_{\text{TOF}} < 58$ ns) count traces for 78841 and 79352 (Figure 46 and Figure 47). Note that the counts in the region $58 < t_{\text{TOF}} < 70$ ns are not a direct probe of the bulk population; also counts from the high energy population will interfere in this region (compare Figure 41).

For 78841, the bulk neutron rate from beam-thermal reactions is a lot higher than the high energy tail neutrons (Figure 46). The bulk trace had to be divided by 20 for comparison. It can be seen (compare Figure 43) that it is only during the solid RF heating period in the beginning of the pulse ($t \leq 6.5$ s) that a fast tail is formed. Also the bulk neutron rate increases during

this period due to the higher NB power, but the bulk rate does not disappear as does the HE rate after the RF power drops.

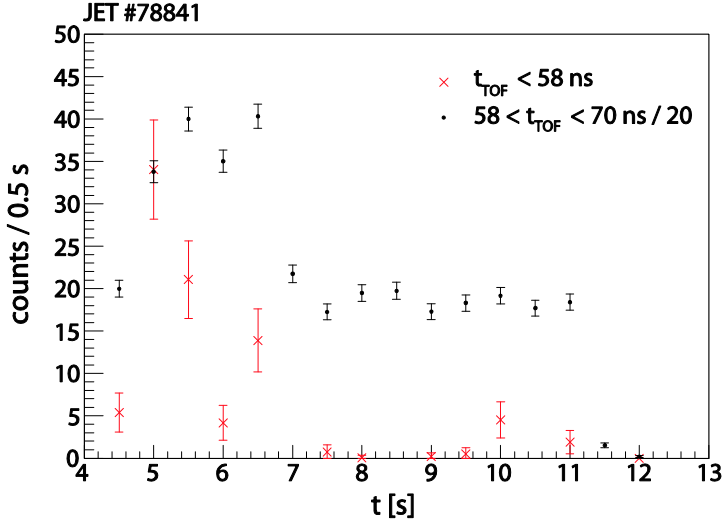


Figure 46. Time traces of summed high energy ($t_{\text{TOF}} < 58$ ns, red crosses) and bulk ($58 < t_{\text{TOF}} < 70$ ns divided by 20, black points) t_{TOF} events obtained from integrating TOFOR data in intervals of 0.5 s for pulse 78841. (Color online)

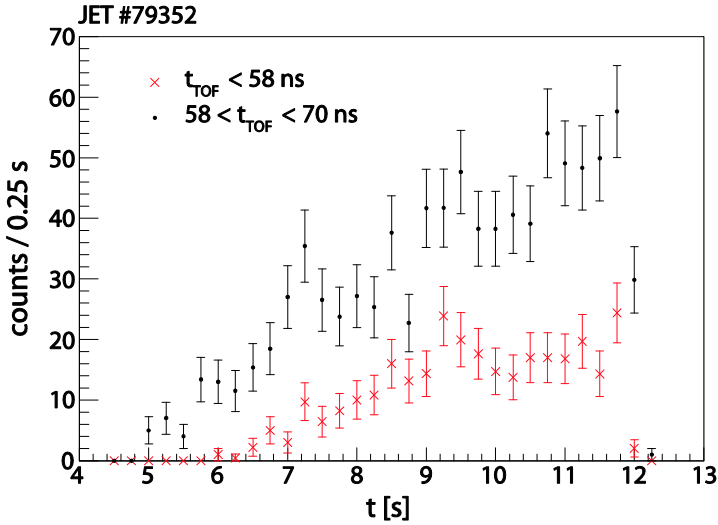


Figure 47. Time traces of summed high energy ($t_{\text{TOF}} < 58$ ns, red crosses) and bulk ($58 < t_{\text{TOF}} < 70$ ns, black points) t_{TOF} events obtained from integrating TOFOR data in intervals of 0.25 s for pulse 79352. (Color online)

For 79352 (Figure 47), the difference between the two traces is not as distinguishable, because also the region 58-70 ns is dominated by the high energy events (no bulk D for the D beam to react with). What can be seen is that the HE trace is at zero at the outset, when the ^3He concentration is low (minority heating) and increases as the ^3He concentration increases (mode conversion). This could however, as described above, be deduced also from the total neutron rate due to the special plasma circumstances.

5.3 Deuterium distribution unfolding

Section 3.4.2 describes deuterium distribution unfolding - a method to directly deduce the deuterium distribution from TOFOR data through fitting of mono-energetic deuterium (δ) spectra such as the ones in Figure 41. Here, we exemplify the use of this method through analysis of t_{TOF} spectra from JET pulse 74945, heated with 3rd harmonic RF tuned to D with a central resonance layer at $R=3$ m, in the TOFOR line of sight. This pulse is from the same session as the pulses studied in paper V, and some similar results are presented also in the paper. Time traces for P_{NB} and P_{RF} and the total neutron rate for pulse 74945 are shown in Figure 48, along with a frequency spectrogram from magnetic pickup coils showing the MHD activity in the plasma.

TOFOR spectra from four 0.5 s intervals, indicated in Figure 48 with Roman numerals, have been studied. During period I, $t=17-17.5$ s, P_{NB} and P_{RF} are constant, and MHD activity in the form of TAE and tornado modes can be observed. At about 17.5 s, a monster sawtooth crash leads to redistribution of the fast ions in the plasma. The second time interval, 18-18.5 s, is chosen to fall after the effect of the sawtooth crash has subsided, but during the period of constant P_{NB} and P_{RF} . During this period, MHD activity in the form of a neo-classical tearing mode (NTM) is observed. Time periods III and IV fall during the notch in P_{RF} with significantly lower RF power, at 18.5-19 s and 19-19.5 s, respectively.

TOFOR spectra for the four time periods are shown in Figure 49, with the fit from applying the deuterium distribution unfolding method indicated. As can be seen, the method is applied only in the region $t_{\text{TOF}} < 65$ ns. The events in the region corresponding to $E_d < E_{\text{beam}}$ are fitted using a beam component. The fits follow the data nicely for all four time periods.

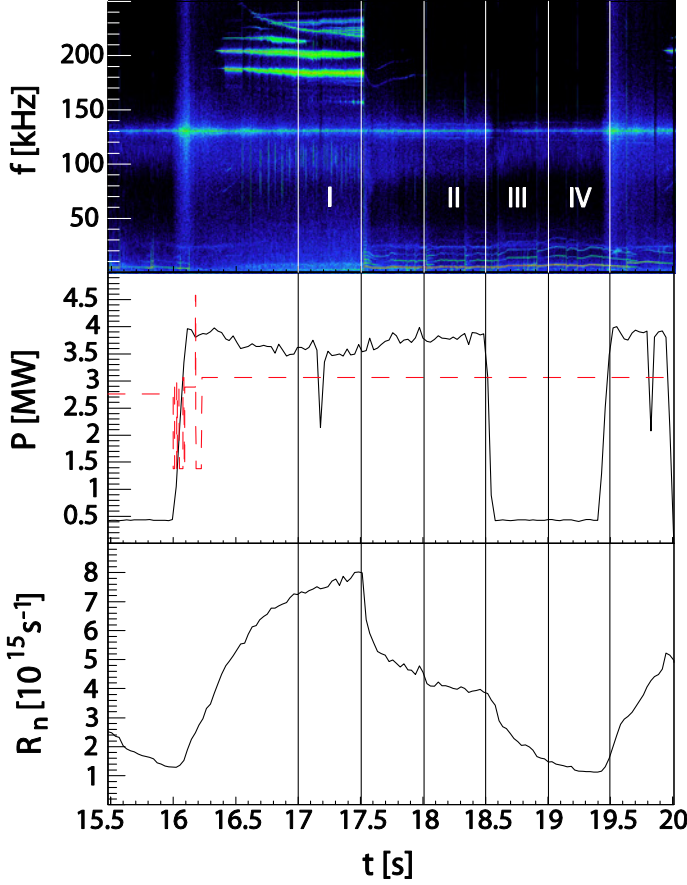


Figure 48. Time traces of plasma parameters for JET pulse 74945. The top panel shows MHD activity displayed as a frequency spectrogram from magnetic pick-up coils, the middle the NB (dashed red) and RF (solid black) heating power and the bottom the total neutron rate from the JET fission chambers.

Figure 50 shows the resulting normalized deuterium distributions (taking the viewing volume in the line-of-sight of TOFOR into account) with error bars from the fits in Figure 49. The four time periods give, in order, the distributions from top to bottom in Figure 50. We start by comparing the top two distributions, from periods with similar heating power but different MHD activity. As can be seen, the distributions are very similar in the low energy region (same P_{NB}) and die off at the same energy (same magnetic field B and electron density n_e give the same cut-off, compare section 1.3.3). However, the D distribution during the NTM (18-18.5 s) is significantly lower than the one during TAE/tornado activity in the intermediate energy region. This is due to the nature of the interaction of the NTMs and TAEs with the fast ion population; however, the detailed explanation is outside the scope of this thesis.

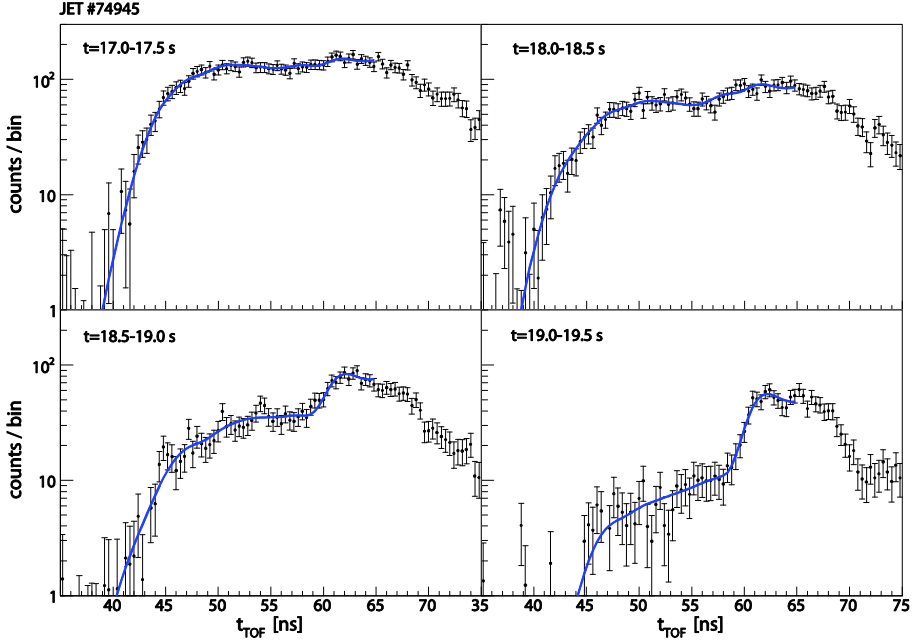


Figure 49. TOFOR data from time periods I, II, III and IV of Figure 48 with fits obtained by applying the deuterium distribution unfolding method indicated. (Color online)

Comparison with the lower two traces demonstrates the effect of the notch in P_{RF} on the D distribution. The third trace from the top represents the average distribution for the first 0.5 s after P_{RF} was reduced, the bottom trace the following 0.5 s period. It is clear that the slowing down of the fast ions in the plasma leads to a gradual drop in the fast D population when fast D is no longer generated through the applied heating.

As mentioned, paper V describes a detailed study of TOFOR observations of interactions between fast ions and MHD modes for pulses from 3rd harmonic heating. The deuterium distribution method was also used in the analysis for paper IV, where the derived distributions are compared with those obtained independently with the high-energy NPA at JET, KF1 (see section 2.2.2). In general, good agreement is seen between the distributions obtained with the two instruments. This cross-validation lends credit to the deuterium distribution method, though there are some discrepancies between the results from the two instruments that we had planned to investigate further in an experiment at JET in October 2009 that was cancelled at the last minute.

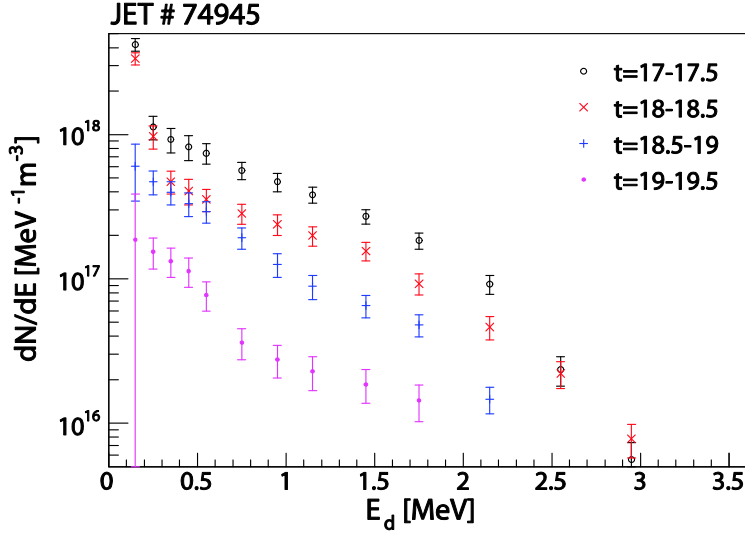


Figure 50. Deuterium distributions resulting from the fits in Figure 49, with the top trace representing the time period 17-17.5 s and the lower traces progressively later time periods. (Color online)

5.4 Beryllium neutrons

As mentioned in section 1.2, it was established in paper VI of this thesis that Be can react with fuel ions to produce neutrons on a level observable with TOFOR. The neutron emission from reactions between Be and fast H, ^3He and ^4He was studied further through simulations in paper VII. The possibility of analyzing beryllium neutrons with TOFOR is a demonstration of the versatility of the instrument. The analysis involves application of the Component fitting method (section 3.4.1) using theoretical components representing reactions between different subpopulations. These components are generated with ControlRoom (section 3.2) for reactions between ion distributions estimated from theory using Stix's formalism (section 1.3).

In this section, we study a set of data from Sept 18th, 2009, as a further example of beryllium neutron observations with TOFOR. The plasma scenario in these pulses is ^4He bulk, ^4He beams (1-2 PINIs) and RF heating tuned to the 3rd harmonic resonance of ^4He . A complicating factor is that there is residual D in the plasma from regular JET operations on a level up to 10%, and that the RF resonance layer for D coincides with that for ^4He (same Z/m ratio). The statistics in the TOFOR data from these pulses are on the low side; in Figure 51, the summed data from the whole session (pulse 79167-79175) are shown. As can be seen, the spectrum is rather flat in the region from 40-75 ns, as expected from 3rd harmonic D heating (compare the top

two panels in Figure 49). An additional structure in the data is visible in the region 30-40 ns; data in this region is consistent with neutrons from the ground state of the ${}^9\text{Be}({}^4\text{He},n){}^{12}\text{C}$ reaction as demonstrated in papers VI and VII.

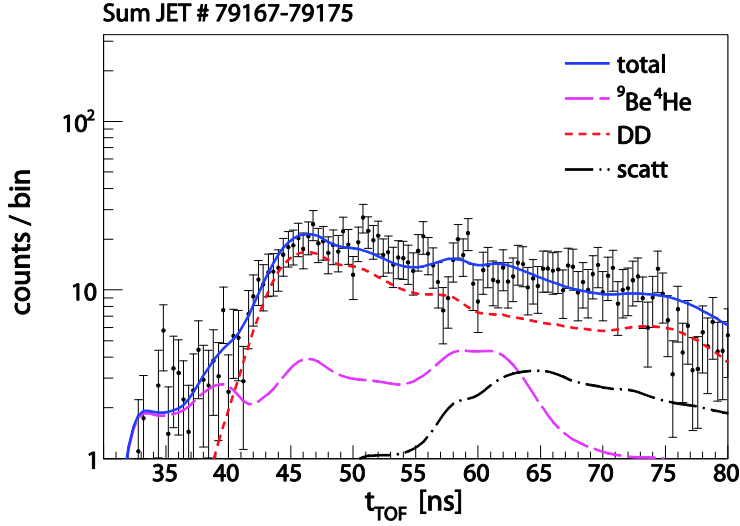


Figure 51. Summed TOFOR data from JET pulses 79167-79175, with a fit to the data (solid blue) indicated. The components of the fit represent the ground and first excited states of the ${}^9\text{Be}({}^4\text{He},n){}^{12}\text{C}$ reaction (long-dashed magenta), the fast D population reacting with itself (short-dashed red) and scatter (dash-dot black). (Color online)

A fit to the data using theoretical components is also shown in Figure 51. The component for the ground- and excited states of ${}^9\text{Be}({}^4\text{He},n){}^{12}\text{C}$ is calculated using ControlRoom with a 4 keV Maxwellian Be population and a theoretical estimate of the fast ${}^4\text{He}$ population using Stix. The electron density varies during the session from $n_e=2.5\times10^{19}\text{ m}^{-3}$ up to $4\times10^{19}\text{ m}^{-3}$. In Figure 52, the theoretical ${}^4\text{He}$ distributions using Stix assuming an applied RF power of $P_{\text{RF}}=0.43\text{ MW/m}^3$ and electron densities $n_e=2.5\times10^{19}\text{ m}^{-3}$, $2.9\times10^{19}\text{ m}^{-3}$ and $3.3\times10^{19}\text{ m}^{-3}$, respectively, are shown. The distributions are calculated for ${}^4\text{He}$ beams ($P_{\text{NB}}=1.3\text{ MW}$, $E_{\text{beam}}=96\text{ keV}$) in a ${}^4\text{He}$ bulk plasma. In the ${}^9\text{Be}({}^4\text{He},n){}^{12}\text{C}$ component used in the fit for Figure 51, $n_e=3.3\times10^{19}\text{ m}^{-3}$ is used.

In Figure 53, D distributions similar to the ones for ${}^4\text{He}$ from Figure 52 are shown. These D distributions are also calculated using Stix with $P_{\text{RF}}=0.43\text{ MW/m}^3$, but for a minority D population in a ${}^4\text{He}$ background plasma, assuming $n_d=0.1\times n_e$. The component for the DD neutrons used in the fit in Figure 51 is calculated making the distribution for $n_e=3.3\times10^{19}\text{ m}^{-3}$ from Figure 53 react with itself.

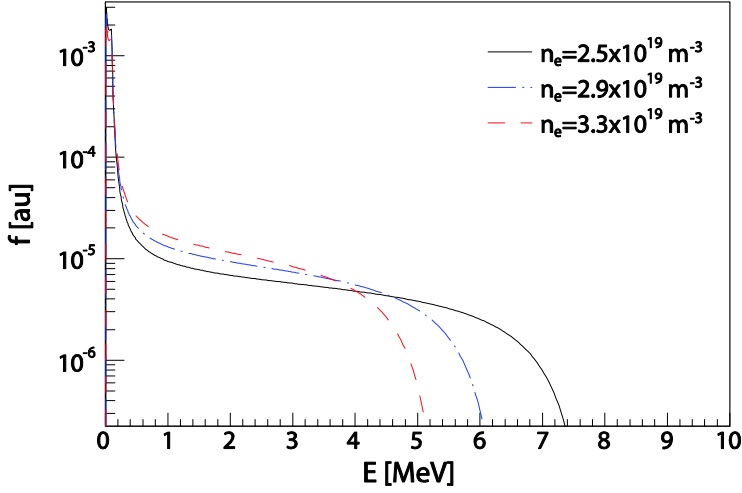


Figure 52. Theoretical distributions calculated using the Stix formalism for the ${}^4\text{He}$ population from 3^{rd} harmonic RF on ${}^4\text{He}$ beams, for electron density values $n_e = 3.3 \times 10^{19} \text{ m}^{-3}$ (dashed red), $n_e = 2.9 \times 10^{19} \text{ m}^{-3}$ (dash-dot blue) and $n_e = 2.5 \times 10^{19} \text{ m}^{-3}$ (solid black). (Color online)

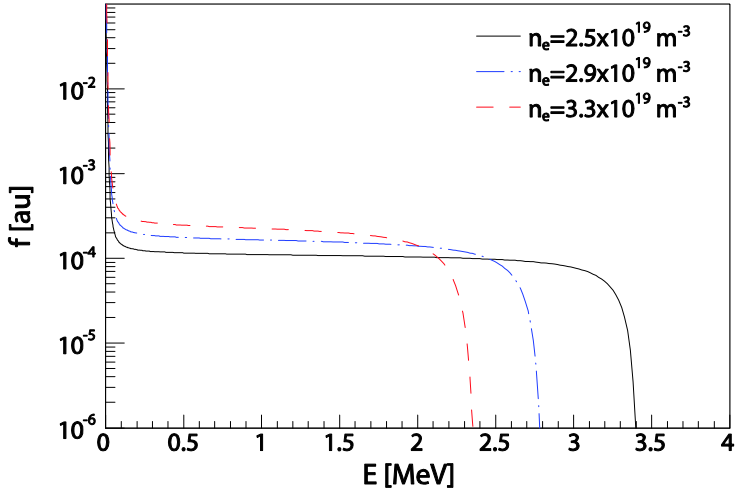


Figure 53. Theoretical distributions calculated using the Stix formalism for the D population from 3^{rd} harmonic RF on minority D , for electron density values $n_e = 3.3 \times 10^{19} \text{ m}^{-3}$ (dashed red), $n_e = 2.9 \times 10^{19} \text{ m}^{-3}$ (dash-dot blue) and $n_e = 2.5 \times 10^{19} \text{ m}^{-3}$ (solid black). (Color online)

The intensity of the scatter component used in Figure 51 is fixed to a fraction 4.6×10^{-11} of the total neutron yield as measured by the JET fission chambers.

The intensities of the ground and excited states of the ${}^9\text{Be}({}^4\text{He},n){}^{12}\text{C}$ reaction are not allowed to vary relative to each other in the fit. The ratio of neutrons from ${}^9\text{Be}({}^4\text{He},n){}^{12}\text{C}$ to neutrons from DD reactions from the analysis is 0.37; $C_{\text{red}}=0.71$.

As mentioned, the statistics of the data from this session are low. However, one simple way to split the data for more detailed analysis is to sum the intervals of single and double PINI heating individually. This has been tried, and the result is shown in Figure 54 (single PINI heating) and Figure 55 (double PINI heating). It is immediately clear from looking at these figures that the ${}^9\text{Be}({}^4\text{He},n){}^{12}\text{C}$ contribution is stronger in the single PINI case while the DD neutron emission completely dominates in the double PINI case. This can be explained by the fact that when two PINIs are used, the seed population of fast ${}^4\text{He}$ for the RF power to couple to becomes too large, leading to better coupling to the minority D ions. The observation of dominating D heating for the double PINI case is also consistent with observations from γ spectroscopy data.

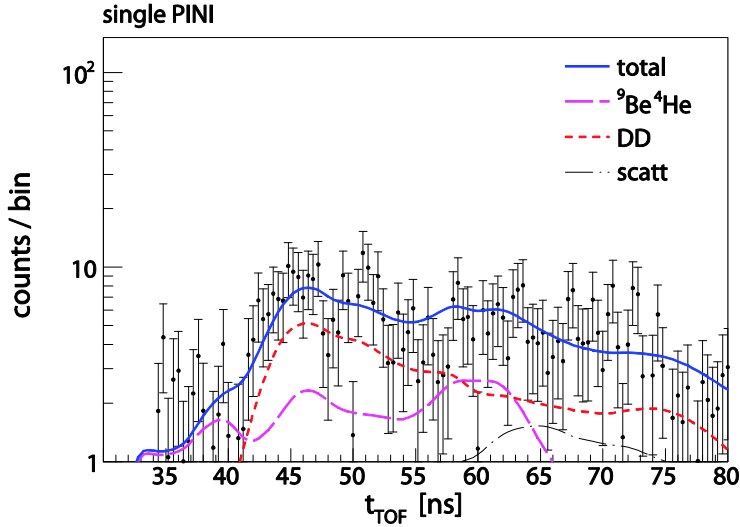


Figure 54. Data from periods with single PINI NB heating only from JET pulses 79167-79175, with a fit to the data (solid blue) indicated. The components of the fit represent the ground and first excited states (long-dashed magenta) of the ${}^9\text{Be}({}^4\text{He},n){}^{12}\text{C}$ reaction, the fast D population reacting with itself (short-dashed red) and scatter (dash-dot black). (Color online)

In both the single and double PINI cases, fits using the same components as for the summed data have been tried. The results are shown in Figure 54 and Figure 55 along with the data. In the single PINI case, the rate of ${}^9\text{Be}({}^4\text{He},n){}^{12}\text{C}$ to DD neutrons is 0.73 and $C_{\text{red}}=0.83$, in the double PINI case these numbers are 0.19 and 0.66, respectively.

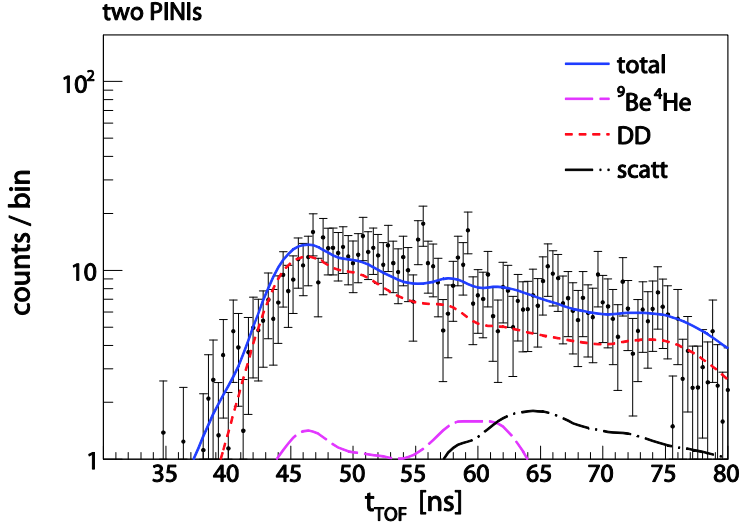


Figure 55. Data from periods with double PINI NB heating only from JET pulses 79167-79175, with a fit to the data (solid blue) indicated. The components of the fit represent the ground and first excited states of the ${}^9\text{Be}({}^4\text{He}, n){}^{12}\text{C}$ reaction (long-dashed magenta), the fast D population reacting with itself (short-dashed red) and scatter (dash-dot black). (Color online)

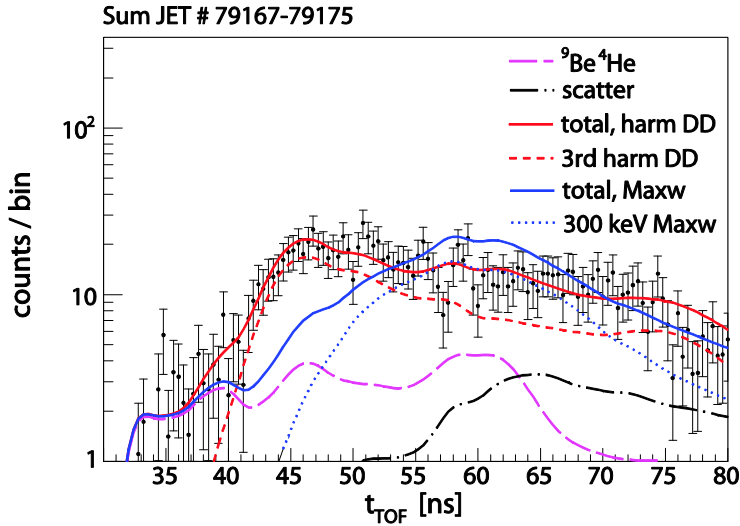


Figure 56. Comparison of fits to the summed TOFOR data from JET pulses 79167-79175 using the theoretical Stix distribution with $n_d=0.1 \times n_e$, $n_e=3.3 \times 10^{19} \text{ m}^{-3}$ (short dashed red) and a 300 keV Maxwellian (dotted blue) to describe the D population. The total fits (solid blue for the Maxwellian, solid red for the Stix distribution) include contributions from ${}^9\text{Be}({}^4\text{He}, n){}^{12}\text{C}$ (long-dashed magenta) and scatter (broken black) components; these are the same in the two cases. (Color online)

In the analysis presented here, we have fitted the data with components based on simple theoretical estimates using Stix. The fits look rather good in all cases. A commonly used assumption when analyzing fast ion data at JET is that the fast ions are Maxwellian distributed. In Figure 56, a comparison is made between fitting a 300 keV Maxwellian distribution reacting with itself (dotted blue curve, total in blue) and the Stix-based component used above (dashed red curve, total in red) to the DD part of the spectrum. It is clear that our fit based on theoretical input, though simple, gives a better description of the data. Further detailed analysis of these data is in progress.

5.5 Results from 14 MeV neutron measurements

TOFOR is optimized for study of the 2.5 MeV neutrons from DD reactions. The latest DT campaign (trace tritium, TTE) was run at JET before TOFOR was installed. However, 14 MeV TBN neutrons (see section 1.2) have been detected with TOFOR, and the same tools used to study the DD emission can be applied also in the TBN case.

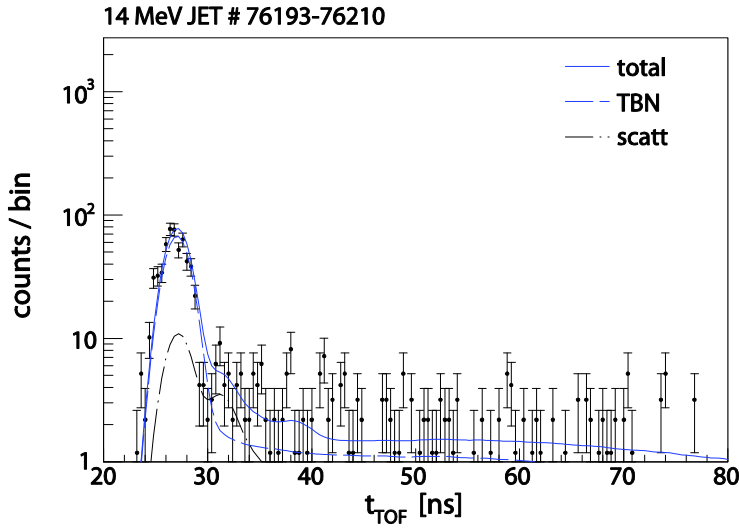


Figure 57. Summed TOFOR time-of-flight spectrum as in Figure 38, collected for pulses 76193-76210 with the instrument set to record events above a higher threshold level only. The solid blue line represents a total fit to the data of a TBN component (dashed blue) and a scatter component (dash-dot black) as described in the text. (Color online)

As discussed in section 4.4, TOFOR can currently through simple software selection be set to run in 14 MeV mode, discriminating against 2.5 MeV neutrons to highlight the weak TBN peak. A data set collected using this

setting was shown in Figure 38. In Figure 57, the same data set is shown together with a fit to the data using the component fitting method described in section 3.4.1. A response function with proton equivalent thresholds $E_p^{S1}=2400$ keV and $E_p^{S2}=500$ keV is used in the analysis. As can be seen, the data is well accounted for with a simplified TBN component and a scatter component ($C_{red}=1.2$).

The TBN component used in the analysis is simulated using ControlRoom (section 3.2) with a Maxwellian D distribution and a slowing down T distribution from $D+D \rightarrow T+H$ (compare section 1.3.2). In the simplified T slowing down simulation, only thermal $D+D$ reactions are taken into account, and the cross sections for $D+D \rightarrow {}^3\text{He}+n$ are used in place of real $D+D \rightarrow T+H$ cross sections. Average T_e , n_e and T_i values from NB heated pulses with $P_{NB}>10$ MW in the range 71729-73979 are used in the simulation.

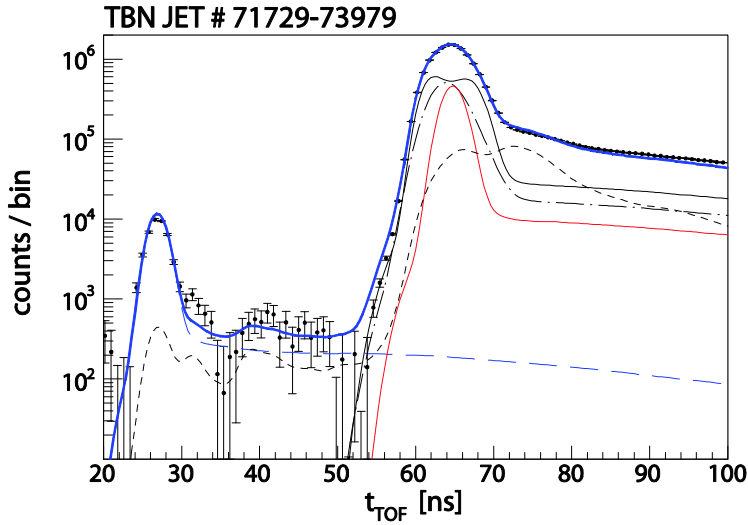


Figure 58. Summed TOFOR time-of-flight spectrum for pulses with $P_{NB}>10$ MW in the interval 71729-73979. The data is shown over a t_{TOF} scale from 20-100 ns, including the 14 MeV neutron peak at 27 ns. Also shown in the figure is the total fit to the data (solid blue line) of TBN (long dashed blue), thermal DD (solid red), beam-thermal DD (solid black), beam-beam (broken black) and scatter (short dashed black) components. (Color online)

The same TBN component is used also in the analysis of the data presented in Figure 58, i.e., the summed t_{TOF} spectrum for NB heated pulses in the range 71729-73979 with $P_{NB}>10$ MW. TOFOR is operated in regular 2.5 MeV mode and the normal response function for the JET pulse interval 71000-74000 is used. The fit to the data using the component fitting method with TBN, thermal DD, beam-thermal DD, beam-beam DD and scatter com-

ponents is shown together with the data in Figure 58. The components on a neutron energy scale are shown in Figure 59. The goodness-of-fit is poor in this case with $C_{\text{red}}=75$. However, the main C_{red} contribution is from the DD part of the spectrum in the region 85-100 ns. It should be noted that the data is summed over some 250 pulses with varying, though similar, conditions; this has implications for the ability to describe the data with the models used. It is also believed that the response function is not known to high enough accuracy to describe data with such high statistics.

It is clear from the figures that beam-thermal and beam-beam reactions are the sources of a significant fraction of the DD neutrons in this case. This means, of course, that tritium produced in beam-thermal and beam-beam DD reactions should also be taken into account in the creation of the TBN component in a detailed analysis. However, the component from this simple simulation describes the data fairly well as can be seen. Only the intensity of the 14 MeV peak is fitted, the shape of the component is fixed from the simulation.

Another observation from Figure 58 is how well the scatter component describes the data over the full range from $t_{\text{TOF}}=27$ to 100 ns. The intensity of the scatter component is completely determined by the DD scatter in the region $t_{\text{TOF}}>70$ ns. The shape is obtained from an estimate of the direct neutron energy spectrum from preliminary fits to the data as described in section 3.3 and paper III.

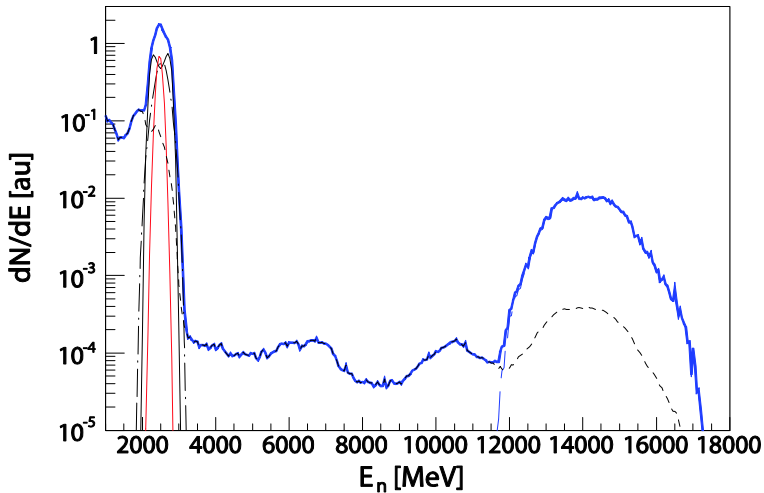


Figure 59. The components obtained from the fit to the data in Figure 58 shown on a neutron energy scale, with colors as in Figure 58. (Color online)

A very simple estimate of the fuel ion density ratio n_t/n_d can be obtained if we ignore the fact that the reactivities are different for thermonuclear, beam-thermal and beam-beam DD reactions, and assume thermal reactivities for DD and DT. For $T_i=4.9$ keV (average for the pulses studied), $\langle\sigma v\rangle_{dt}/\langle\sigma v\rangle_{dd}\approx 160$. Then

$$\frac{Y_{dt}}{Y_{dd}} = \frac{n_d n_t \langle\sigma v\rangle_{dt}}{\frac{1}{2} n_d^2 \langle\sigma v\rangle_{dd}^{thermal} + n_d n_{beam} \langle\sigma v\rangle_{dd}^{beam-thermal} + \frac{1}{2} n_{beam}^2 \langle\sigma v\rangle_{dd}^{beam-beam}} \quad (21)$$

reduces to

$$\frac{Y_{dt}}{Y_{dd}} \approx \frac{n_t}{n_d} \cdot 320. \quad (22)$$

The component analysis of TOFOR data in Figure 58 yields $Y_{dt}/Y_{dd}=0.47/(2.7+7.9+4.9)$, which gives $n_t/n_d=1\times 10^{-4}$. This is a low estimate; the beam-thermal and beam-beam DD reactivities are higher than the thermal, reducing the factor 320 in equation (22).

6 Outlook

It is rare in science that we come to an answer – rather that we come to more questions.

Barbara Badelek, 2008-12-11

This thesis concerns the development and characterization of the TOFOR neutron spectrometer at JET, as well as measurements using TOFOR in varying plasma scenarios. It has been shown that TOFOR provides a strong contribution to the fast ion physics program at JET.

The work undertaken has contributed to the understanding of and made it possible to correct for peculiarities of the instrument detectors and electronics. The discriminator thresholds in the electronics, the time alignment of the detectors relative to each other and a residual electronics broadening due to pulse height resolution and timing uncertainty issues have been seen to be of crucial importance in understanding the response of the instrument to incident neutrons. Neutrons that have scattered in the line-of-sight before reaching TOFOR contribute significantly to the recorded data and have to be taken into account in the analysis.

In this section, we discuss possible improvements of the TOFOR setup and analysis (section 6.1). Also, a number of physics issues are identified to which TOFOR is foreseen to contribute in the next few years (section 6.2).

6.1 Instrument improvements

A deeper understanding of the response of TOFOR to incident neutrons improves the data analysis, because it allows for a closer match between the response as estimated in the instrument response function and the actual response as it manifests itself in the measured data. Our estimate of the TOFOR response to incident neutrons could be further improved by

- i. correcting also for S2 time alignment,
- ii. regular and accurate threshold determination, and
- iii. more sophisticated determination of the electronics broadening.

The challenge with point (i) is the low statistics in the ohmic time board data for each individual S2 detector. However, a correction method could in principle easily be developed based on a larger number of pulses than in the S1 case.

Point (ii), i.e., the threshold determination, is a more delicate issue. As pointed out in section 4.5, weekly threshold calibrations using the ^{22}Na source in the S1 box should be introduced for the S1 detectors before the next campaign. If such regular checks are introduced, it would be of importance to also develop an automated method for threshold determination. For the S2s, applying the ^{22}Na source method during campaigns is not straightforward. TOFOR is equipped also with a laser light source, fitted with a polarizer to allow for automatic variations of the light intensity, as described in paper II. The threshold level in the ADC spectrum from a sweep over different laser intensities does not fall at the same channel number as in the ^{22}Na case, and the energy scales are also not comparable due to different pulse shapes. However, if careful threshold settings using ^{22}Na before the start of campaigns were combined with laser runs to correlate the ADC spectrum threshold levels from the two methods, laser sweeps could be used to monitor the S2 thresholds for drifts.

The current method used to determine the electronics broadening (iii), where the response function is broadened with a Gaussian of a width that gives good agreement with charge exchange measurements, is not satisfactory. This has a direct impact on the ability of TOFOR to provide an independent measurement of the bulk ion temperature. The *ad-hoc* broadening needed in the response function could possibly be reduced by introducing hybrid boards, thus eliminating the time walk introduced by the CFDs, and correcting for S2 time alignment variations. It should also be possible to determine the energy-dependent pulse height resolution of TOFOR. A method for such pulse height determination is outlined in [69], where the parameters α , β and γ in equation (17) are determined through a fit to (a minimum of three) Compton edges from different gamma sources. The method currently used for determining the thresholds could possibly also be improved in this way, by making the fits to the data easier.

In addition to the improvements already listed, another few points can be identified that would contribute to TOFOR instrumental development.

- A further investigation should be undertaken on the CFD time walk issue. This could be done by acquiring a polarizer such as the one used for the laser for use with the LED. Since the LED light is emitted simultaneously with a synch signal, an absolute timing reference would be available in this case. The results would, however, be limited by the 0.1 ns timing uncertainty due to the machining of the light fibers fed to each detector, and by the 0.4 ns bin width of time boards.
- Each S1 detector signal represents the sum of signals from three PM tubes. To further improve the instrument response,

it would be of interest to monitor the gain of individual S1 PM tubes. How this could be done is however not clear.

- Monitoring of load-dependent PM tube gain drifts would make it possible to check for threshold variations *during* high-intensity JET pulses. Also for this there is currently no method available.
- An annoying peculiarity of TOFOR is the synchronization procedure of the time boards. Synchronization is triggered by an initialization signal from the central JET computers two minutes before each pulse, and the process is random. Too frequently the time boards are not synchronized on time before the pulse starts and the data are lost. The procedure for synchronization should be improved.

A major upgrade of TOFOR is being considered where (i) the S1 detectors would be replaced with new ones with better light yield, hence larger pulse heights, improved pulse height resolution and better timing, and (ii) hybrid boards would be introduced in the electronics. As discussed in section 4.4, hybrid boards would improve the versatility of TOFOR in making it possible to focus the analysis on different energy regions of the spectrum from the same pulse. Introducing hybrid boards would also be a test to see if the randoms contribution can be reduced enough to make TOFOR useful for higher flux DD and 14 MeV neutron measurements.

6.2 Future experiments and data analysis

A new ITER-like wall (ILW) is being installed at JET during the current shutdown (2010). This project involves replacement of most of the plasma-facing C components with Be ones. Some of the divertor tiles, currently consisting almost entirely of C, will be replaced with W tiles, and some coated with a layer of W.

After the ILW installation, the Be impurity concentration in the plasma is expected to increase. In the campaigns following the shutdown, further interference in the measured TOFOR spectra from Be neutrons such as described in paper VI and section 5.4 might be expected. This could lead to further conclusions on the topic of Be neutrons at ITER (paper VII).

The new Be-rich environment should also provide ample opportunity for cross-validation of γ and TOFOR data. Cross-validation of the available fast-ion diagnostics is relevant because of the important role fast ions will play in future fusion reactors. At ITER, fast ion measurements in the region $E_n < 1$ MeV are expected to increase in importance due to the foreseen beam ion injection energy. The experiment planned and accepted to further cross-

validate TOFOR and NPA measurements in this energy region (preparatory study presented in paper IV) should be run as part of the new campaigns.

TOFOR can measure 2.5 and 14 MeV neutrons simultaneously, as demonstrated in section 5.5. This feature of the instrument should be exploited to test fuel ion ratio determination methods. This could be done in a more detailed study of DD data than that presented in section 5.5, but would be even more interesting in a future trace tritium campaign.

Scattered neutrons are of crucial importance for the fuel ion ratio determination, and these investigations should continue. The scattered neutron simulations used in the analysis of TOFOR data (paper III) also need to be rechecked after the ILW installation at JET.

6.3 Outlook to ITER

Neutron spectrometry is an ITER relevant diagnostic technique. A line-of-sight has been enabled for a neutron spectrometer in the ITER design, but there is at present no money allocated for its construction. Several of the neutron spectrometer techniques envisaged for ITER demand large apertures in the first wall in order to achieve the necessary count rates to fulfill the measurement requirements (in terms of time resolution and precision). There are concerns [24] that a large first wall aperture could lead to unacceptably high neutron fluxes relatively far from the ITER tokamak. An optimal balance between acceptable levels of neutron streaming and spectrometer performance has yet to be found.

Ref [24] lists a number of required plasma measurements for ITER. T_i and n_i/n_d , both discussed in this thesis, appear as essential in the list. Another relevant quantity is $Q_{\text{thermal}}/Q_{\text{non-thermal}}$, related to the determination of progress towards a plasma sustained with progressively higher fractions of intrinsic heating. Neutron spectrometry could, as has been shown here, be useful in determining these quantities. A further detailed simulation study of the feasibility of using neutron spectrometry for n_i/n_d measurements is underway in the group, building partly on the scattered neutron results presented in this thesis. Especially during the DD phase of operations and when trace (single percent) amounts of tritium are introduced, neutron spectrometry would be well suited for this type of measurement.

Also the determination of fuel ion energy distributions resulting from various heating schemes is highly ITER relevant, as is the possibility of contributing to the study of interactions between fast ions and MHD modes. At ITER, also beam ions would be energetic enough to resonate with Alfvén modes (depending on plasma scenario), making the type of analysis exemplified in paper V more generally applicable. Finally, a neutron spectrometer could turn out to be of interest also for the non-activated phase of ITER, for determination of the neutron emission spectrum from beryllium reactions.

7 Sammanfattning på svenska

The substance [may be] too complicated to get across, it is the image that is important.

Kenneth Wilson, Nobel Prize Winner

Den här avhandlingen handlar om TOFOR, som är en neutronspektrometer installerad på fusionsforskningsreaktorn JET utanför Oxford i England. De flesta har nog hört talas om fusion och att det ska vara en lovande metod för framtidens energiförsörjning, men vad är det egentligen? Och hur kan man ha nytta av en neutronspektrometer när man försöker lära sig hur man ska få fusion att fungera som energikälla?

Fusion innebär att två lätta joner slås ihop och bildar en tyngre. Den sammanlagda massan hos de partiklar som blir kvar efter reaktionen är lägre än massan hos de reagerande partiklarna. Massan som har försvunnit frigörs i form av energi enligt Einsteins berömda formel $E=mc^2$. Principen är densamma som för vanlig kärnkraft, fission, fast omvänt: I fission delas en tyngre kärna i två lättare med resultatet att massan efter är mindre än massan före och energi frigörs. Fusion är en attraktiv energiform eftersom mycket lite bränsle krävs för att frigöra stora mängder energi.

Fusionsreaktioner mellan tunga isotoper av väte, deuterium (D) och tritium (T), är mest lovande för framtidens energiproducerande reaktorer eftersom sannolikheten att de ska ske blir relativt hög redan vid relativt låga temperaturer (100 miljoner grader) och eftersom en stor mängd energi frigörs i varje reaktion. En komplikation är dock att T är radioaktivt med en halveringstid på 12,3 år. Detta betyder dels att extra säkerhetsåtgärder krävs för att köra en fusionsreaktor med T, och dels att T inte finns tillgängligt i naturen. I framtiden räknar man med att skapa T i reaktorerna genom reaktioner mellan litium och neutroner. I dagsläget väljer man oftast att köra forskningsreaktorer med bara deuterium, som också kan reagera med sig självt, dock med något lägre sannolikhet och mindre frigjord energi.

Fusionsbränslet (vätejonerna) måste alltså vara mycket varmt för att en tillräcklig andel av bränslet ska reagera. Vid sådana höga temperaturer är materien i plasmaform – atomerna delar upp sig i sina laddade beståndsdelar, joner och elektroner. Laddade partiklar hålls på plats i ett magnetfält och det utnyttjas i fusionsforskningen. Den hittills mest framgångsrika reaktormodellen för fusion är ett badringsformat magnetfält (tokamak) i vilket fusionsbränslet får reagera. Fusionsreaktioner sker vid sådana forskningsanläggningar över hela världen idag. JET är EU:s flaggskepp på fusionsområdet och världens just nu största tokamak. Nästa steg mot kommersiell fusion är

byggandet av en ny forskningsanläggning, ITER, som ska stå klar i södra Frankrike 2018. En stor del av den forskning som görs idag handlar om att förbättra förutsättningarna för att lyckas med ITER. Målet med ITER är att visa att mer energi går att producera än som krävs för att värma upp plasmat. Däremot räknar man inte med att producera el från ITER – det är avsikten med den nästföljande reaktorn i fusionsprogrammet, DEMO.

I både D+T- och D+D-reaktioner skapas helium och neutroner. Energin frigörs i form av rörelseenergi hos dessa partiklar, som därmed blir mycket energirika. Tanken är att heliumet, som är laddat, ska stanna i reaktorn och hålla bränslet varmt, medan neutronen, som är oladdad, ska lämna magnetfältet och använda sin energi till att värma vatten i reaktorväggen. Elektricitet ska sedan genereras i en ångcykel som på traditionella elkraftverk. I dagens forskningsreaktorer räcker värmen från det skapade heliumet inte för att hålla plasmat varmt. Yttre uppvärmning i form av neutralstråleinjektionsuppvärmning eller radiofrekvensuppvärmning tillämpas. Neutralstråleinjektionsuppvärmning innebär att bränslejoner accelereras till höga energier utanför plasmat och neutraliseras för att kunna komma in i magnetfältet. Väl inne joniseras de snabbt igen och överför sin energi till plasmat genom kollisioner med plasmapartiklarna. Radiofrekvensuppvärmning innebär att vågor skickas ut från antenner i reaktorväggen, med en frekvens som matchas till frekvensen med vilken ett partikelslag snurrar runt fältlinjerna i magnetfältet. Resonans mellan vågen och snurrfrekvensen gör att partiklarnas snurrhastighet, och därmed energi, ökar.

Samtliga former av uppvärmning, inre med snabba heliumjoner såväl som yttre med neutralstråleinjektion eller radiofrekvensvågor, innefattar överföring av värme från snabba partiklar i plasmat till övriga genom kollisioner. Även fusionsreaktionerna sker naturligtvis i kollisioner. För att de snabba jonerna ska kunna kollidera med övriga joner i plasmat så krävs att de hålls kvar i magnetfältet. Forskning på vilka mekanismer som påverkar inneslutning i eller förlust av snabba joner från magnetfältet är därför av stor vikt.

Olika så kallade diagnostiker används för att försöka förstå vad som händer inuti fusionsplasmat. Neutrondiagnostik är ett exempel. Det finns många fördelar med neutronmätningar. Neutronerna skapas i reaktioner mellan bränslejonerna och bär därmed med sig direkt information om dessa. De är neutrala, vilket betyder att de lämnar magnetfältet och blir en indikator på utsidan på vad som händer på insidan av reaktorväggen. Det betyder dels att neutrondiagnostikinstrumenten inte behöver utsättas för den enorma påfrestning som plasmamiljön utgör, med hög värme och högt partikelflöde, och dels att de kan mäta plasmaegenskaper utan att påverka plasmat. Dessa fördelar kommer att väga tungt på ITER och framförallt på DEMO, där allt högre partikelflöden och temperaturer gör reaktormiljön allt ogästvänligare. Neutrondiagnostik är en framtidsmetod.

En viktig uppgift för neutrondiagnostiken är att räkna antalet utsöndrade neutroner, dels som ett mått på hur många reaktioner som sker, och därmed

den producerade fusionseffekten, och dels av säkerhetsskäl – neutronerna aktiverar de omgärdande strukturerna och myndigheterna kräver noggrann kontroll av hur många neutroner som produceras. Neutronflödesmonitorer sköter den uppgiften.

TOFOR är som sagt ett exempel på en neutronspektrometer. Sådana har som mål att mäta energin hos de utsöndrade neutronerna. Om man känner till neutronenergispektrumet, det vill säga den relativa intensiteten av neutroner med olika energier, så kan man dra slutsatser om energifördelningen hos bränslejonerna. Denna information kan användas för att avgöra hur väl de olika uppvärmningssystemen fungerar, liksom till viss del även till ökad förståelse av inneslutnings- och förlustmekanismer. Sådan kunskap blir en bit i det pussel som måste läggas innan fusion kan komma att fungera som kommersiell elenergikälla.

Neutronspektrometri som diagnosmetod för fusionsplasman föreslogs redan 1967. Metodens framgång är beroende på hur många neutroner som går att mäta, vilket i sin tur beror på både antalet utsöndrade neutroner från plasmat och neutrontektionseffektiviteten hos instrumentet. 1967 var utsöndringshastigheten från fusionsreaktorer mycket låg. JET är en stor fusionsreaktor med god förmåga att producera neutroner. TOFOR är optimerad för att detektera så många (D+D-) neutroner som möjligt. Kombinationen av de två ger förutsättningar att ta neutronspektrometrin till nya höjder.

Arbetet med den här avhandlingen började med bygga och installation av TOFOR på JET (artikel I och II). Stor vikt har lagts vid att förbättra förståelsen av hur inkommande neutroner återspeglas i uppmätta data. TOFOR mäter flygtiden för neutroner mellan två detektorer. Eftersom flygsträckan är känd går det att räkna ut hastigheten hos neutronerna och därmed deras energi. Problemet kompliceras av att inte alla neutroner går raka vägen från den ena detektorn till den andra (multipelspridning) och av att det är ganska svårt att mäta händelser med den precision som krävs (tiondels nanosekunder). Hur det uppmätta flygtidsspektrumet relaterar till neutronenergispektrumet beskrivs av instrumentets responsfunktion, som diskuteras i detalj i själva avhandlingstexten, kapitel 4.

Förutom detaljerad förståelse för hur TOFOR reagerar på inkommande neutroner så krävs också förståelse för hur spridda neutroner påverkar uppmätta data för noggrann analys. Artikel III behandlar sådana neutroner, som alltså inte går raka vägen från plasmat till TOFOR utan sprider i reaktorgvägen eller omgivande strukturer på vägen, med förlust av energi som följd. Sådana spridda neutroner påverkar alla neutronmätningar och förståelse av dem är viktig både för korrekt räkning av antalet neutroner och detaljerad analys av energispektrumdata.

En viktig punkt i arbetet med ett nytt instrument är att kontrollera att resultaten blir rimliga. Ett sätt att göra detta är att jämföra med resultat från andra diagnostiker. På JET finns tre system som används för att studera inneslutna snabba joner: Neutronspektrometri, gammaspektroskopi och in-

strument för analys av neutrala partiklar (NPA). I artikel IV jämför vi resultat från TOFOR med resultat från NPA, som använder en helt annan metod för att studera liknande saker som TOFOR.

Allt detta bakgrundsarbete med instrumentkonstruktion, förståelse av TOFOR:s respons, simulering och mätningar av spridda neutroner och validering för att kontrollera att resultaten stämmer överens med andra diagnostiker kröns i avhandlingen med två artiklar, V och VI, med nya fysikresultat som uppnåtts med TOFOR. I artikel V beskrivs hur TOFOR har kunnat användas för att studera hur snabba joner interagerar med instabiliteter i magnetfältet med väldigt fin tidsupplösning. Detta var möjligt eftersom neutronutsöndringshastigheterna var höga i de speciella radiofrekvensuppvärmda plasman som studerades, och tack vare TOFOR:s goda effektivitet. Metoden är lovande för ITER där neutronflödena efter några år bör bli mycket höga. Artikel VI beskriver hur TOFOR använts för att mäta även neutroner från mindre vanliga fusionsreaktioner mellan beryllium och helium. Detta är intressant dels ur instrumentell synpunkt för att det visar på flexibiliteten hos TOFOR, dels inför framtiden. På JET installeras just nu en ny reaktordvägg som består av beryllium. ITER beräknas också ha en berylliumplasmavägg. Det betyder att beryllium kommer att finnas med som betydande orenhet i framtida plasman och reaktioner som de som observerats med TOFOR kommer att öka i betydelse.

Artikel VII behandlar en ren simuleringsstudie som försöker besvara hur många berylliumneutroner som kan tänkas skapas under de första åren efter att ITER har tagits i bruk, det vill säga under kampanjer då ITER ännu inte har certifierats som nukleär anläggning och inga neutroner egentligen får produceras. Slutsatsen av studien blir att betydande neutronflöden kan förväntas från berylliumreaktioner vid vissa uppvärmningsscenarier. Detta är av betydelse i planeringen av ITER-experimenten.

Acknowledgements

*Berätta vad som är bra i ert liv så får ni
kraft att hantera det som är jobbigt.*

Hans Öhman, 2009-11-26

The work with TOFOR has truly been a group effort. I started my PhD at the same time as the hardware for the instrument started arriving and the first six months, Matthias, Anders, Luca and I built the spectrometer. Those endless hours with black tape, cardboard cut to mm precision, alignment and calibration in the basement classroom-turned-lab make up some of my best memories from my time as a PhD student. Matthias, you have been my main supervisor - thank you for everything. Anders, before me there was you. Without your design work, TOFOR would not be what it is today.

Thank you, Jan, for bringing me on. Your enthusiasm and patience with my questions are highly appreciated. Thank you, Göran, for all your help, for proof reading and for guiding me forward through various projects.

Carl – we have collaborated our way to great work! I will remember our trips to England, Italy, Bulgaria and Ukraine, our endless discussions in the office – and all the secrets that Erik and I keep teasing you about. The DAQ “computer crash” is another happy memory. Sean, your MCNP expertise never fails, I would not have been able to make the roof lab computers do what I wanted without you, and all those lunches at JET were great. (Maybe you should start eating lunch in Sweden too?) Marco C, working with you on the TOFOR-NPA comparison was inspiring. Luca – thank you for always willingly me helping out with any calibration questions. I am amazed by how you still two years after you left the department can pull pulse shape files off your computer within 24 hours.

Erik, it is not your help with TOFOR (though significant) that I will always remember you for, but all the coffee and support right when it was needed the most, the discussions and all our important rules. I will never use week numbers again. Henrik, I will also try to avoid wearing my bike helmet inside. Besides, there is always HTPD! And thanks Henrik and Hans for introducing me to life at JET all those years ago. Lele, our trip to Cadarache was great.

Marco T, Giuseppe and Massimo – also your contributions are appreciated. Thank you for receiving us in Milan, for the collaborations and discussions and not least for the dinners while at JET. Sergei P, Andrea, Vasily, Liviu, Sergei S, Garry and all others who have helped at JET – thank you.

There are plenty of other people at the department who have contributed to making work fun. I will especially remember the coffee breaks with Angelica and Pernilla. All other diploma students, PhD students, seniors and administrators – you know who you are.

Mattias, du var med när jag påbörjade det här och jag önskar att jag kunde få dela även avslutningen med dig. Mamma, pappa, Markus och Annica, tack för att ni har funnits där under alla de här åren.

Darrin, more than anyone my thoughts go to you. For your love, for your endless support and encouragement, for listening and understanding and for putting up with all the physics jokes – thank you. Nova och Zoey, det är ni som gör livet roligt och spännande. Utan er skulle det här inte ha varit samma utmaning ☺

References

-
- 1 F.F. Chen, Introduction to Plasma Physics and Controlled Fusion Volume 1, 2nd Ed., Plenum Press New York and London 1984
 - 2 M. Shimada et al., *Progress in the ITER Physics Basis, Chapter 1: Overview and summary* Nucl. Fusion **47** (2007) S1-S17
 - 3 Y. Shimomura et al. *ITER overview* Nucl. Fusion **39** (1999) 1295-1308
 - 4 V. Mukhovatov et al., Review of Scientific Instruments **68** (1996) 1250-1255
 - 5 Wesson, J., Tokamaks, 3rd Ed., Oxford Science Publications, Clarendon Press, Oxford, 2004
 - 6 T.H. Stix, Nuclear Fusion **15** (1975) 737-754
 - 7 T.H. Stix, Waves in Plasmas, Springer Verlag New York Inc., 1992
 - 8 J. Ongena et al., Transactions of Fusion Science and Technology **49** (2006) 337-345
 - 9 L.-G. Eriksson, T. Hellsten and U. Willén, Nuclear Fusion **33** (1993) 1037-1048
 - 10 R. Koch, Transactions of Fusion Science and Technology **49** (2006) 187-194
 - 11 D. Van Eester et al., Plasma Physics and Controlled Fusion **51** (2009) 044007 (31pp)
 - 12 L. Giacomelli et al., Review of Scientific Instruments **79** (2008) 10E514
 - 13 D. Van Eester, F. Louche and R. Koch, Nucl. Fusion **42** (2002) 310-328
 - 14 A. Salmi et al., PPCF **48** (2006) 717-726
 - 15 M.-L. Mayoral et al., Nucl. Fusion **46** (2006) S550-S563
 - 16 J. Hedin et al., Nuclear Fusion **42** (2002) 527-540
 - 17 L.-G. Ericsson et al., Nuclear Fusion **38** (1998) 265-278
 - 18 R. Koch et al., Plasma Physics and Controlled Fusion **37** (1995) A291-A302
 - 19 M.J. Mantsinen et al., Physical Review Letters **88** (2002) 105002-1
 - 20 V.G. Kiptily et al., Nuclear Fusion **45** (2005) L21-L25
 - 21 S. Sharapov et al., Nuclear Fusion **45** (2005) 1168-1177
 - 22 S. Pinches et al., Nuclear Fusion **46** (2006) S904-S910
 - 23 I.H. Hutchinson, Principles of Plasma Diagnostics, Cambridge University Press 1987
 - 24 A.J.H. Donné et al., *Progress in the ITER Physics Basis, Chapter 7: Diagnostics* Nucl. Fusion **47** (2007) S337-S384
 - 25 W. Morris, *Physics and diagnostics of DEMO-class devices*, Int workshop on burning plasma diagnostics, Varenna, Italy, Sept 2007
 - 26 O.N. Jarvis, PPCF **36** (1994) 209-244
 - 27 M.T. Swinhoe and O.N. Jarvis, Nucl. Instrum. Meth. **221** (1984) 460
 - 28 S. Popovichev, L. Bertalot, M. Adams, A. Alekseyev, M. Angelone, C.D. Chailis, S. Conroy, N. Hawkes, J. Hobirk, V. Kiptily, A. Kaschuck, A. Krasilnikov, P.U. Lamalle, A. Murari, M. Pillon, K. Stammers, D. Stork and JET-EFDA contributors, *Performance of Neutron Measurements during Trace Tritium Experiments on JET*,

-
- 31st EPS Conference on Plasma Phys. London, 28 June - 2 July 2004 ECA Vol.28G, P-5.173 (2004)
- 29 O.N.Jarvis, E.Clipsham, M.Hone, B.Laundy, M.Pillon, M.Rapisarda, G.Sadler, P. van Belle and K.A.Verschuur, *Use of activation techniques for the measurement of neutron yields from deuterium plasmas at the Joint European Torus*, Fusion Technology **20** (1991) 265
- 30 B. Esposito, L. Bertalot, M. Loughlin and A.L. Roquemore, Rev. Sci. Inst. **70** (1999) 1130-1133
- 31 S. Conroy, O. N. Jarvis, G. Sadler and G. B. Huxtable, *Time resolved measurements of triton burnup in JET plasmas*, Nuclear Fusion **28** (1988) 2127-2134
- 32 M. Adams et al., Nuclear Instruments and Methods A **329** (1993) 277-290
- 33 O.N. Jarvis, Nuclear Instruments and Methods A **476** (2002) 474-484
- 34 F.D. Brooks and H. Klein, Nuclear Instruments and Methods A **476** (2002) 1-11
- 35 A.V. Krasilnikov, V.N. Amosov, P. van Belle, O.N. Jarvis and G. Sadler, Nuclear Instruments and Methods A **476** (2002) 500-505
- 36 W.A. Fisher et al., Physical Review A **28** (1983) 3121-3123
- 37 Yu.A. Kaschuck et al., *Neutron Measurements during Trace Tritium Experiments at JET Using a Stilbene Detector*, 31st EPS Conference on Plasma Phys. London, 28 June - 2 July 2004 ECA Vol.28G, P-5.174 (2004)
- 38 A. Zimbal et al., Review of Scientific Instruments **75** (2004) 3553
- 39 N.P Hawkes et al., Review of Scientific Instruments **70** 1134
- 40 S. Conroy et al., Review of Scientific Instruments **79** (2008) 10E508
- 41 E.Andersson Sundén et al., Nucl. Instr. and Meth. A **610** (2009) 682-699
- 42 J. Frenje et al., Review of Scientific Instruments **79** (2008) 10E502
- 43 T. Elevant, Nuclear Instruments and Methods in Physics Research A **476** (2002) 485-489
- 44 H. Bindslev et al., Physical Review Letters **83** (1999) 3206-3209
- 45 W.W. Heidbrink et al., Plasma Physics and Controlled Fusion **46** (2004) 1855-1875
- 46 W.W. Heidbrink et al., Plasma Physics and Controlled Fusion **49** (2007) 1457-1475
- 47 S. Baeumel et al., Fus Eng Des **74** (2005) 853-857
- 48 V.G. Kiptily et al., Nuclear Fusion **42** (2002) 999-1007
- 49 V. I. Afanasyev et al., Rev Sci Inst **74** (2003) 2338-2352
- 50 A.B. Izvozchikov, et al., *Charge-Exchange Diagnostic for Fusion Alpha Particles and ICRF Driven Minority Ions in MeV Energy Range in JET*, Plasma Rep. JET-R(1991)12, JET Joint Undertaking, Abingdon (1991).
- 51 A.A. Korotkov, A. Gondhalekar and A.J. Stuart, Nuclear Fusion **37** No. 1 (1997) 35-51
- 52 G. Lehner and F. Pohl, Zeitschrift für Physik **207** (1967) 83-104
- 53 H. Brysk, Plasma Physics **15** (1973) 611-617
- 54 W. Cash, The Astrophysical Journal **228** (1979) 939
- 55 M. Olsson et al., Plasma Physics and Controlled Fusion **35** (1993) 179-191
- 56 G. Gorini and J. Källne, Review of Scientific Instruments **63** (1992) 4548-4550
- 57 F. Ognissanto et al., Review of Scientific Instruments **79** (2008) 10E511
- 58 H. Henriksson et al., Review of Scientific Instruments **72** (2001) 832-835
- 59 M. Tardocchi et al., Review of Scientific Instruments **70** (1999) 1171-1175
- 60 H. Henriksson et al., Nuclear Fusion **46** (2006) 244-253

-
- 61 J. Källne et al., *Physical Review Letters* **85** (2000) 1246-1249
- 62 L. Ballabio et al., *Nuclear Fusion* **38** (1998) 1723
- 63 L. Ballabio et al., *Physical Review E* **55** (1997) 3358-3368
- 64 G.F. Knoll, *Radiation Detection and Measurement*, 3rd Ed., John Wiley & Sons, Inc., 2000
- 65 MCNPX User's Manual, Version 2.5.0, LA-CP-05-0369, edited by D.B. Pelowitz (2005)
- 66 E. Andersson Sundén et al., Evaluation of spectral unfolding techniques for neutron spectroscopy, 2008 *Burning Plasma Diagnostics An International Conf. Varenna Italy 24-28 September 2007* Orsitto F P, Gorini G, Sindoni E and Tardocchi M Melville New York AIP Conf. Proc 988 315-318
- 67 A. Hjalmarsson, *Development and Construction of a 2.5-MeV Neutron Time-of-Flight Spectrometer Optimized for Rate (TOFOR)*, PhD thesis Acta Universitatis Upsaliensis, Uppsala 2006, <http://urn.kb.se/resolve?urn=urn:nbn:se:uu:diva-7198>
- 68 M. Gherendi et al., *Journal of Optoelectronics and Advanced Materials* **10** (2008) 2092-2094
- 69 G. Dietze and H. Klein, *Gamma-calibration of NE213 scintillation counters*, NIM 193 (1982) 549-556
- 70 H.H. Knox and T.G. Miller, *A technique for determining bias settings for organic scintillators*, NIM 101 (1972) 519-525
- 71 R. Madey et al., *The response of NE-228A, NE-228, NE-224, and NE-102 scintillators to protons from 2.4 to 19.55 MeV*, NIM 151 (1978) 445-450
- 72 N.P. Hawkes et al., *Measurements of the proton light output function of the organic liquid scintillator NE213 in several detectors*, NIM A **476** (2002) 190-194
- 73 S. Conroy, private communication, November 2007
- 74 J. Frenje, *Instrumentation for Fusion Neutron Measurements and Experimentation at JET*, PhD thesis Acta Universitatis Upsaliensis, Uppsala 1998, ISBN 91-554-4125-4
- 75 http://gwdac.phys.gwu.edu/analysis/nn_analysis.html
- 76 H. Sjöstrand et al., *Rev. Sci. Instrum.* **80** (2009) 063505
- 77 C. Hellesen et al., *Neutron spectroscopy measurements and modeling of neutral beam heating fast ion dynamics*, submitted to *Plasma Physics and Controlled Fusion*
- 78 P. Kårén, *Ion distribution box models for the NBI heating system at JET using neutron emission spectroscopy*, Master's thesis, Uppsala University Department of Physics and Astronomy 2009-02-11
- 79 C. Hellesen et al., *Review of Scientific Instruments* **79** (2008) 10E510

Acta Universitatis Upsaliensis

*Digital Comprehensive Summaries of Uppsala Dissertations
from the Faculty of Science and Technology 715*

Editor: The Dean of the Faculty of Science and Technology

A doctoral dissertation from the Faculty of Science and Technology, Uppsala University, is usually a summary of a number of papers. A few copies of the complete dissertation are kept at major Swedish research libraries, while the summary alone is distributed internationally through the series Digital Comprehensive Summaries of Uppsala Dissertations from the Faculty of Science and Technology. (Prior to January, 2005, the series was published under the title "Comprehensive Summaries of Uppsala Dissertations from the Faculty of Science and Technology".)



ACTA
UNIVERSITATIS
UPSALIENSIS
UPPSALA
2010

Distribution: publications.uu.se
urn:nbn:se:uu:diva-114077